



**Università degli Studi di Genova**

**Facoltà di Scienze Matematiche, Fisiche e Naturali**

**Ph.D. Thesis in Physics**

**XVIII ciclo**

May, 2006

**Development of the Timing Counter for the MEG  
experiment**

**Dr. Riccardo Valle**

*Supervisor:*

Prof. Flavio Gatti

*External supervisor:*

Dott. Dino Zanello



*A mio padre...*



*“Si d'accordo ma poi.....tutto il resto è noia”*

Franco Califano

# ***Index***

<b><i>Introduction</i></b>	I
<b><i>Chapter 1 Theoretical introduction</i></b>	1
<b><i>Chapter 2 <math>\mu \rightarrow e \gamma</math> experiment: MEG</i></b>	5
2.1. Beam and target at PSI	7
2.2. Photon detector	10
2.3. Positron detector	13
2.3.1. COBRA magnet	13
2.3.2. Drift chambers	17
2.3.3. Timing counter: conceptual design	19
2.4. Trigger and data acquisition system	21
2.5. Background and sensitivity	23
2.5.1. Physics background	26
2.5.2. Accidental background	27
2.5.3. Sensitivity	30
<b><i>Chapter 3 Timing-counter sub-detector</i></b>	33
3.1. PMTs characterization in magnetic field	35
3.2. Test of the tilted PMT solution in the COBRA magnet	41
3.3. Time resolution measurements at the beam	45
3.3.1. Early test	49
3.3.2. Choice of scintillator and PMT	51
3.3.3. Results and Interpretation	55
3.3.4. Validation test in magnetic field	58
3.4. Front-end electronics	59
3.4.1. Considerations on PMT time resolution	62
3.5. Final measurements	65
3.5.1. Preparation of the bars	66
3.5.2. Preparation of the PMTs	69
3.5.3. Conclusions	70
<b><i>Chapter 4 Triggering sub-detector</i></b>	73
4.1. Detector concept	74
4.1.1. Scintillator fibers	74
4.1.2. Avalanche Photodiodes	76
4.2. APD characterization	78
4.2.1. Thermal dependence	79
4.2.2. APD evaluation	82
4.2.3. Dark current and gain measurements	85

<b>4.3. Fibers characterization</b>	<b>87</b>
4.3.1. Light propagation measurements	89
4.3.2. Emission spectrum measurements	94
4.3.3. Remarks on cladding properties	96
4.3.4. Summary of the scintillating fiber measurements	98
<b><i>Chapter 5 Preparation of <math>\alpha</math>-source on wire and target for <math>(p,\gamma)</math> energy calibration of LXe detector</i></b>	<b>101</b>
5.1. Radioactive wire-sources	102
5.2. Targets for the Cockcroft-Walton accelerator	105
5.2.1. Preparation of copper plates	106
5.2.2. Preparation of LiF targets	108
5.2.3. Preparation of B targets	109
5.2.4. Experimental setup	109
5.2.5. Results	110
<b><i>Appendix A Plastic scintillators</i></b>	<b>115</b>
<b><i>Acknowledgements</i></b>	<b>117</b>

## ***Introduction***

The aim of MEG experiment is to observe the  $\mu^+ \rightarrow e^+ \gamma$  decay with a Branching Ratio (BR) sensitivity of about  $5 \times 10^{-14}$ , improving of about two orders of magnitude the actual limit (BR =  $1.2 \times 10^{-11}$ ) obtained by MEGA experiment in 1999.

The flavour violating decay of the muon with a branching ratio between  $10^{-12}$  and  $10^{-14}$  is foreseen by the several super-symmetric extension of the Standard Model (SM) of the elementary particle. In SM, the absence of mixing angles caused by the assumption of massless neutrino leads to a strong conservation law of the lepton flavour (LFC) which inhibits processes as  $\mu^+ \rightarrow e^+ \gamma$  decay. If the neutrino mass is introduced in the standard theory instead, a reaction with Lepton Flavour Violation should have an extremely low BR ( $< 10^{-40}$ ); only super-symmetric theories predict a BR in the range of the MEG experiment. Therefore, MEG has a chance to discriminate between SM and super-symmetric models.

Anyway, also the non observation of the  $\mu^+ \rightarrow e^+ \gamma$  decay at the desired sensitivity would be important, leading to strong constraints on these theories and, in general, on the nature of this new physics.

To observe the  $\mu^+ \rightarrow e^+ \gamma$  decay, it is extremely important to optimize the detection of the back-to-back positron-photon pairs: the positron momentum is measured by a set of drift chambers placed in inhomogeneous magnetic field and its timing is given by a timing counter, whereas the photon energy and timing are measured by a liquid Xe calorimeter.

This thesis is devoted to the study of the timing counter detectors for the positron produced in the muon decay. The conceptual design, the related problems and the strategies that have been adopted in order to achieve the required performances will be discussed.

The main goal of the timing counter is to obtain a timing resolution of the positron impact time of 100 ps FWHM. This performance must be achieved inside a magnet with a field intensity of about 1 Tesla. The timing counter must provide also a first level trigger for selecting a subset of events with the proper angular correlation with the gamma. Therefore it is composed by two sub-detectors that are specialized in time and position measurement separately. The timing counter has a double layer structure of cylindrical shape with a radius slightly smaller than the magnet bore.

My contribution to this research has been mainly devoted to the study of the general design and of the instrumental solution for the realization of high timing resolution scintillating elements capable to operate in high magnetic field environment, which include scintillator, photomultipliers, readout-techniques. This sub-detector successfully achieved a timing resolution better than 100 ps, namely 90 ps in average.

I have also contributed to the study of the sensitive part of the position sub-detector in which an innovative solution that makes use of scintillating fibers and Avalanche Photodiode (APD) was proposed. The APDs have been used instead of Photomultipliers, allowing a single particle identification with a spatial resolution of 5 mm over 800 mm of detector length. Further, I have contributed to the construction and test of calibration source for the Liquid Xe detectors constituted by small source of alpha particle on thin wire to be placed inside the calorimeter and of the targets for  $\gamma$ -line generation by means of proton capture in Lithium and Boron.

The plan of this work is the following.

- In Chapter 1 a short overview of the theoretical background is presented.
- Chapter 2 describes the whole MEG detector and in particular the role of the timing counter; the calculation on sensitivity and background are also shown.
- In Chapter 3 the structure of the timing sub-detector, composed by parallel scintillator bars is presented. The magnetic field behavior of different types of photomultipliers and the optimized solution for the coupling of PMT- scintillator bar are studied. The optimization of scintillator bars geometry and size is

reported. Moreover, the acquisition technique to obtain the best resolution is described.

- Chapter 4 is devoted to the characterization of APDs used to read the light produced in scintillating fibers hit by positrons. To select the best APDs, different batches are tested. Furthermore, the physics of scintillating fibers is studied.
- In Chapter 5 my contribution to calibration of the LXe calorimeter is described.



# *Chapter 1*

In this chapter, a short overview<sup>1</sup> of the theoretical motivation in muon decay physics will be presented. Obviously, its aim is to evidence the main scientific motivations for the MEG experiment and not to give a detailed theoretical description, which is out of the purposes of this Ph.D. thesis. A more detailed description is reported in Dussoni's Ph.D. thesis<sup>2</sup>.

The muon was discovered in cosmic rays by Neddermeyer and Anderson in 1937<sup>[3]</sup>. They found experimentally that, the mass of the muon was about 200 times the mass of the electron. The discovery was made just after Yukawa (1935)<sup>4</sup> postulated the existence of the  $\pi$ -meson, a force carrier of the strong interaction. In 1947, Conversi, Pancini and Piccioni<sup>5</sup> demonstrated, however, that the muon did not interact through strong forces, and thus it could not be the Yukawa  $\pi$ -meson. It was believed that the muon decayed into an electron and a neutral particle. It was thought that if the muon was a heavy electron, it would also decay into an electron and a  $\gamma$ -ray. The first search for  $\mu^+ \rightarrow e^+ \gamma$  was made in 1947 by Hincks and Pontecorvo<sup>6</sup> using cosmic ray muons. This was the beginning of the search for the lepton flavor violation and the negative results set an upper limit on the branching ratio of less than 10%.

## **Theoretical introduction**

After the discovery of parity violation (Lee and Yong 1956), it was suggested that the weak interaction took place through the exchange of charged intermediate

vector bosons<sup>7</sup>. In 1958, Feinberg pointed out that the intermediate vector boson, if it exists, would lead to  $\mu^+ \rightarrow e^+ \gamma$  at a branching ratio of  $10^{-4}$  [8]. The absence of any experimental observation of the  $\mu^+ \rightarrow e^+ \gamma$  process with  $B(\mu^+ \rightarrow e^+ \gamma) > 2 \times 10^{-5}$  led directly to the two-neutrino hypothesis<sup>9</sup> in which the neutrino coupled to the muon differs from that coupled to the electron, and the  $\mu^+ \rightarrow e^+ \gamma$  process is forbidden. The two-neutrino hypothesis was verified experimentally at Brookhaven National Laboratory (BNL) by observing muon production but not electron production from the scattering of neutrinos produced from pion decays<sup>10</sup>. This introduced the concept of a separate conservation law for individual lepton flavours, electron number ( $L_e$ ) and muon number ( $L_\mu$ ).

Our understanding of modern elementary particle physics is based on the standard model (SM), which is a gauge theory of the strong and electroweak interactions. The formulation of the SM is based on many theoretical developments of gauge theory in the 1960s and 1970s. Since then, the SM has held out numerous experimental tests, being entirely consistent with all precision measurements to date. In the minimal version of the SM, where only one Higgs doublet is included and mass-less neutrinos are assumed; lepton flavour conservation is an automatic consequence of gauge invariance and the renormalizability of the SM Lagrangian. It is the basis of a natural explanation for the smallness of lepton flavour violation (LFV) in charged lepton processes. However, in extensions of the minimal SM, LFV could occur from various sources. In fact, in many new physics scenarios one would expect LFV at some level. Important LFV processes involving muons are  $\mu^+ \rightarrow e^+ \gamma$ ,  $\mu^- - e^-$  conversion in a muonic atom ( $\mu^- N \rightarrow e^- N$ ) and  $\mu^+ \rightarrow e^+ e^+ e^-$ . The current LFV searches with muons are now sensitive to branching ratios of the order of  $10^{-12} - 10^{-13}$ . In general, searches for rare processes could probe new interactions mediated by very heavy particles. For example, in the four-fermion interaction, the LFV branching ratios could be scaled by  $(m_W/m_X)^4$ , where  $m_X$  is the mass of an exotic heavy particle responsible for the LFV interaction and  $m_W$  is the mass of the  $W$  gauge boson ( $\sim 80$  GeV). In such a scenario, the present sensitivities for LFV searches in muon decays could probe  $m_X$  up to several hundred TeV, which is not directly accessible at present or planned accelerators.

Recently, considerable interest in LFV processes has arisen based on super-symmetric (SUSY) extensions to the SM, in particular super-symmetric grand unified

theories (SUSY GUT). Since the three gauge-coupling constants of the strong, weak, and electromagnetic interactions, which were measured at LEP and SLC, have been shown to be consistent with the assumption that they unify to a single  $SU(5)$  gauge-coupling constant at a scale of the order of  $10^{16}$  GeV in SUSY SM, SUSY GUT models have become very attractive candidates for physics beyond the SM. In SUSY models, in general there is a new source of flavour mixing in the mass matrices of SUSY partners for leptons and quarks. This would induce LFV processes for charged leptons whose branching ratios depend on the flavour mixing in the mass matrix of the sleptons, which are the super-symmetric partners of leptons. In the SUSY GUT scenario, the flavour mixing in the slepton sector is naturally induced at the GUT scale because leptons and quarks are in the same GUT multiplet<sup>11</sup>. It has been shown<sup>[12,13]</sup> that the large top-quark mass has an impact on the calculations of the branching ratios of  $\mu^+ \rightarrow e^+ \gamma$  and  $\mu^- \rightarrow e^-$  conversion in SUSY GUT's. The predictions are just one or two orders of magnitude lower than the present experimental limits.

There is considerable evidence for the existence of neutrino masses and mixing based on the experimental results of the solar neutrino deficit<sup>[14,15,16,17,18]</sup> and the atmospheric neutrino anomaly<sup>19</sup>. Since neutrino oscillations indicate that lepton flavour is not conserved, LFV processes in muon decays are also expected to occur. In non-SUSY models, however, the neutrino mixing introduces only small contributions to  $\mu^+ \rightarrow e^+ \gamma$ . For example, the branching ratio of  $\mu^+ \rightarrow e^+ \gamma$  is of the order of  $10^{-50}$  for a neutrino mass-squared difference of  $\Delta m_\nu^2 \sim 10^{-3}$  eV<sup>2</sup>, due to a suppression factor of  $(\Delta m_\nu^2 / m_W^2)^2$ <sup>[20,21]</sup>. The situation changes drastically in SUSY models. In SUSY models with a neutrino-mass generation mechanism of the see-saw type, the Yukawa coupling constants among the Higgs doublet, lepton doublets, and right-handed neutrinos could induce large flavour-mixing effects in the slepton sector<sup>[22,23,24]</sup>. The resulting LFV rates can be as large as (or even exceed) the present experimental upper bounds, depending on the various parameters in question, especially the Majorana mass of the right-handed neutrino. In such a case, the Yukawa coupling constants associated with the right-handed neutrino are responsible for both the neutrino oscillation and the LFV processes of charged leptons. Thus there are many theoretical scenarios in which the predicted branching ratios for the muon LFV processes can be close to their present experimental upper bounds, and therefore could be accessible to and tested with future

experiments. There has been much progress on the experimental front. First of all, several new results have been obtained using the high-intensity muon beams now available, and ongoing and proposed experiments are aiming for further improvements. Furthermore, in the long term, new attempts to create high-intensity muon sources have been initiated, based on the ideas arising from the  $\mu^+ \mu^-$  collider project. The desired muon beam intensity at such a muon source would be about  $10^{12} - 10^{13} \mu^\pm/s$ , which is several orders of magnitude higher than that presently available. With this increased muon flux, significant improvements in experimental searches can be anticipated.

## Bibliography Chapter 1

---

- <sup>1</sup> Y. Kuno and Y. Okada, Rev. Mod. Phys. 73 (2001).
- <sup>2</sup> S. Dussoni, MEG collaboration, Ph.D. Thesis, “Search for Lepton Flavour Violation: The MEG experiment”, May 2006.
- <sup>3</sup> S. H. Neddermeyer and C. D. Anderson, Phys. Rev. 51 (1937) 884.
- <sup>4</sup> H. Yukawa, Proc. Phys. Math. Soc. Jap. 17 (1935) 48.
- <sup>5</sup> M. Conversi et al., Phys. Rev. 71 (1947) 209.
- <sup>6</sup> E. P. Hincks and B. Pontecorvo, Can. J. Res. 28 A (1950) 29.
- <sup>7</sup> R.P.Feynman and M. Gell-Mann, Phys. Rev. 109, (1958) 193.
- <sup>8</sup> G.Feimberg, Phys. Rev. 116, (1958) 1482.
- <sup>9</sup> K.Nishijima, Phys. Rev. 108, (1957) 907.
- <sup>10</sup> G.Danby, J.M. Gaillard, K. Goulian, L.M. Lederman, N. Mistry, M. Schwartz, and J. Steinberger, Phys. Rev. Lett. 9, (1962)36.
- <sup>11</sup> L.J Hall, V.A. Kostelecky, and S. Raby, Nucl. Phys. B 267, (1986) 415.
- <sup>12</sup> R. Barbieri and L.J. Hall, Phys. Lett. B 338, (1994)212.
- <sup>13</sup> R. Barbieri, L.J. Hall, and A. Strumia, Nucl. Phys. B 445, (1995) 219.
- <sup>14</sup> J.N. Abdurashitov *et al.* (SAGE Collaboration), Phys.Rev. Lett. **77**, (1996) 4708.
- <sup>15</sup> Y. Fukuda *et al.* (Kamiokande Collaboration), Phys. Rev. Lett. **77**, (1996) 1683
- <sup>16</sup> B.T. Cleveland *et al.*, Astrophys. J. 496, (1998).505
- <sup>17</sup> Y. Fukuda *et al.* (Super-Kamiokande Collaboration), Phys. Rev. Lett. 81, (1998)1158 and 4279(E).
- <sup>18</sup> W. Hampel *et al.* (Gallex Collaboration), Phys. Lett. B 447, (1999) 127.
- <sup>19</sup> Y. Fukuda *et al.* (Super-Kamiokande Collaboration), Phys. Rev. Lett. 81, (1998) 1562.
- <sup>20</sup> S.M. Bilenky, S.T. Petcov, and B. Pontecorvo, Phys. Lett. B 67, (1977) 309.
- <sup>21</sup> S.T. Petcov, Yad. Fiz. 25, 641 [Sov. J. Nucl. Phys. 25, (1977) 340].
- <sup>22</sup> F. Borzumati and A. Masiero, Phys. Rev. Lett. 57, (1986) 961.
- <sup>23</sup> J. Hisano, D. Nomura, and T. Yanagida, , Phys. Lett. B 437, (1998) 351.
- <sup>24</sup> J. Hisano and D. Nomura, Phys. Rev. D 59, (1999) 116005.

## *Chapter 2*

In this chapter, the MEG experiment<sup>1</sup> will be described. This experiment has the aim to reach a Branching Ratio (BR) sensitivity on the  $\mu^+ \rightarrow e^+ \gamma$  decay of  $5 \times 10^{-14}$ , with an improvement of two orders of magnitude with respect to the actual limit, obtained by MEGA experiment in 1999<sup>[2]</sup>. The detector will be mounted at Paul Scherrer Institute (PSI) in Villigen, using the  $\pi E5$  beam, one of the most intense Direct Current (DC) muon beam presently available. In the following subchapters, a detailed description of all sub-detectors will be given. In particular, the beam and the target configuration, to produce low energy muon beam that satisfies the experimental requirements and the photon and positron detector will be presented.

### **$\mu \rightarrow e \gamma$ experiment: MEG**

The major background in  $\mu^+ \rightarrow e^+ \gamma$  searches, is the accidental coincidence of two muon decays in the target: a positron, coming from standard Michel decay ( $\mu^+ \rightarrow e^+ + \nu_e + \bar{\nu}_\mu$ ), and  $\gamma$ -ray, coming from radiative muon decays ( $\mu^+ \rightarrow e^+ + \nu_e + \bar{\nu}_\mu + \gamma$ ). Annihilation of positrons in flight or external bremsstrahlung also contributes to photon backgrounds. Since the accidental background increases quadratically with the muon rate, each daughter particle comes from a different muon, a continuous DC muon beam showing a lowest instantaneous rate, is the best choice for a  $\mu \rightarrow e \gamma$  search, rather than a pulsed beam. In this way, to achieve a BR sensitivity of  $10^{-14}$  with a detection

efficiency  $\varepsilon = 10\%$  in a typical observation period of one year ( $t = 10^7$  s), a muon rate of  $R_\mu \cong \frac{10^{14}}{\varepsilon \cdot t} \cong 10^8 \mu^+/\text{s}$  is necessary.

The reduction of background is achieved by precise measurements of the available experimental parameters. Experimental efforts have been devoted to the improvement of detection resolutions of four variables: the energy of the  $\gamma$ -ray,  $E_\gamma$ , and the positron momentum,  $p_e$ , (that should be equal to  $m_\mu/2$ ); the angle between positron and photon,  $\theta_{\gamma e}$ , which should be  $180^\circ$ ; and the time difference between photon and positron at the origin in the target,  $\Delta t_{\gamma e}$ , that should be equal to zero, within a resolution of 150 ps FWHM.

Assuming  $\mu^+ \rightarrow e^+ \gamma$  as a single two body decay at rest, as sketched in Figure 2.1, the process identification seems easier than the usual muon Michel decay one. It consists of simultaneous back-to-back emission of a high energy positron and a  $\gamma$ -ray, from the muon stopping target. Indeed, to utilize this simple kinematic in the search, muons are stopped in a material, namely a thin polyethylene target. Positive muons are used to avoid capture by the target nuclei.

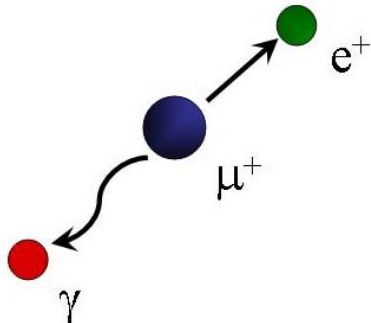


**Figure 2.1:**  $\mu^+ \rightarrow e^+ \gamma$  at rest in a stopping target.

The experimental setup is schematically shown in Figure 2.2. DC surface muon beam of  $10^7$ - $10^8$  /s is focused and stopped in a thin plastic target.  $\gamma$ -rays from  $\mu^+ \rightarrow e^+ \gamma$  decays are measured by a liquid Xenon (LXe) scintillation detector, located just outside a very thin solenoidal magnet defined COnstant Bending RAdius (COBRA). Positrons are tracked by drift chambers inside COBRA, which provides specially graded magnetic field. The timing is measured by plastic scintillation counters in the second turn of the helicoidal trajectories inside the COBRA.

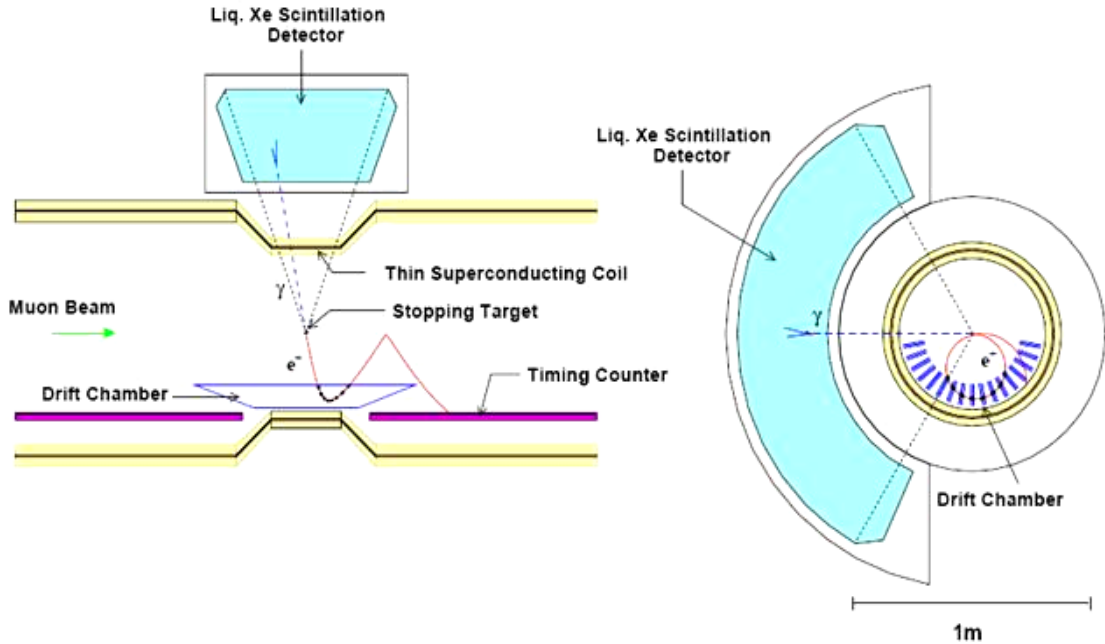


**Figure 2.2:** Schematic view of the MEG detector<sup>1</sup>.

To minimize the accidental coincidence and also to achieve this new sensitivity limit, the experiment should be designed to achieve the following items:

- continuous muon beam, rather than pulsed beam, to minimize the instantaneous muon rate, available at PSI;
- high resolution  $\gamma$ -ray detector that sustains high rate;
- special positron spectrometer with graded magnetic field;
- high resolution positron counter.

## 2.1. Beam and target at PSI

The PSI cyclotron accelerator produces protons with energy of 590 MeV. These protons have a high current,  $\geq 1.8$  mA, and are transported to two meson production graphite targets: a thinner one called M-target (7 mm thick) and a thicker one called E-target (40-60 mm thick). The  $\pi$ E5 beam line extracts low energy pions and muons from the E-target at an angle of  $175^\circ$ , with respect to the primary proton beam. The main characteristics of the beam are listed in Table 2.1.

**Table 2.1:** Main properties of the  $\pi$ E5 beam line.

Solid angle acceptance	150 msr
Momentum range	20-120 MeV/c
Length	10.4 m
Momentum band (FWHM)	10%
Momentum resolution (FWHM)	2%
Horizontal emittance	15.3 cm·rad
Vertical emittance	3.6 cm·rad
Spot size	4×4 cm <sup>2</sup>

For many experiments with muons it is necessary to stop a high intensity muon beam in a very thin target. A muon beam with very low momentum is advantageous since its range is short and straggling is small. In fact the range R is approximately<sup>[3]</sup> proportional to  $p^{3.5}$  where p is the muon momentum, hence the range spread  $\Delta R$  associated with momentum spread  $\Delta p$  of the muon beam rapidly decreases with momentum, as shown by:  $(\Delta R)_{tot} = [(0.1)^2 + (3.5\Delta p / p)^2]^{0.5} p^{3.5}$ . Usually a good approximation of the range straggling is to consider it 10% of the range. It is interesting to note that, in the experiment at SIN<sup>19</sup>, the energy loss in the target alone introduced uncertainty of 4 MeV/c in the positron momentum.

For the MEG experiment, the beam channel will be tuned to collect surface muons<sup>4</sup>. Positive pions produced in the hadronic interactions may stop inside the target and decay to muons which may escape from the target with peak kinetic energy of 4 MeV (29 MeV momentum)\*. These muons have a well determined momentum and polarization. However, the main drawback is the positron contamination which is high:  $e^+/\mu^+ \sim 10$ . These positrons arise from the decay of muons trapped in the E-target and from the conversion of photons from neutral pion decays. For this reason, the positrons must be reduced to avoid showing up in the positron spectrometer and, in other cases, to minimize the background of annihilation photons, if stopped in the experimental hall.

Therefore, there are two features that must be taken into account: the first one acts on the reduction of positrons to a small fraction of muons flux; the second one is the reduction of the muon momentum in order to stop them in a thin target (150  $\mu$ m). Consequently, the beam must be manipulated as described below. The final setup of the

---

\* This method can not be applied to produce  $\mu^-$  beam, since  $\mu^-$  mesons stopped in a target are captured by nuclei at a rate that is large compared to the  $\pi^- \rightarrow \mu^-$  decay rate.

$\pi$ E5 beam line is shown in Figure 2.3. There are two sets of quadrupole magnets and a solenoid magnet (inside this, there is a momentum degrader, that allows to reduce the  $\mu^+$  momentum) to couple the last quadrupole and the MEG magnet. An electrostatic separator is used as a velocity selector, to reject unwanted positrons in the beam. Indeed, the beam distribution intensity, after the separator, is split in two beams with Gaussian distribution of the intensity. The final separation between muons and positrons is  $\sim 7.2 \sigma^{[5]}$ . Therefore, considering that the target size covers  $\pm 2\sigma$  of the  $\mu^+$  distribution, the residual ratio  $e^+/\mu^+$  is given by the tail of the  $e^+$  distribution in the  $\mu^+$  beam. Being the  $\pi$ E5  $e^+/\mu^+$  ratio  $\sim 10$  with  $N_e \sim 9.8 \times 10^8 e^+/s$  before the separator, the  $e^+$  suppression factor introduced by the separator is  $5.7 \times 10^{-7}$  [6]. In addition, the degrader inside the solenoid reduces the positron contamination of the muon beam by a factor 9<sup>[1]</sup>. Then we expect  $\sim 60 e^+/s$  on the target with a residual ratio  $e^+/\mu^+$  of  $\sim 6 \times 10^{-7}$ .

In this way, the beam can be focused in ellipsoidal spot with horizontal and vertical profiles of  $\sigma_x = 5.5$  mm and  $\sigma_y = 6.5$  mm. In presence of helium gas, the profiles increase to a  $\sigma_x = 10.0$  mm,  $\sigma_y = 10.0$  mm.

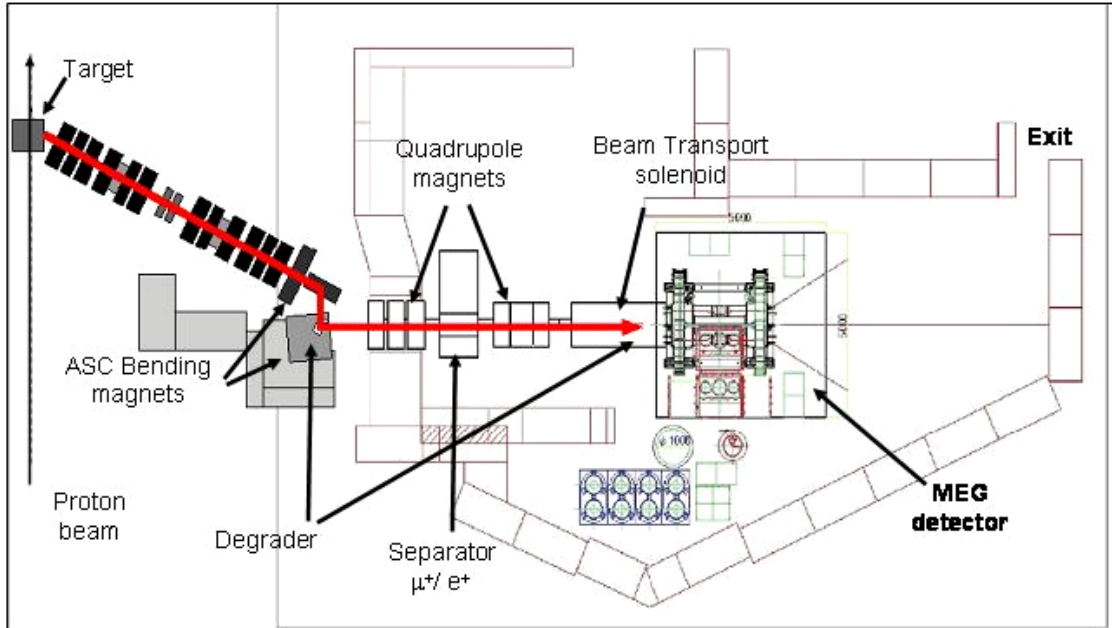


**Figure 2.3:** The  $\pi$ E5 beam line for the MEG experiment.

The introduction of surface muon beams allows to stop the muons in thinner targets. The target will be placed at a slant angle of  $22^\circ$ , which corresponds to a slant

ratio of 1/2.5 in a He-gas atmosphere. Three target/degrader materials were considered: Polyethylene ( $\text{CH}_2$ ), Mylar ( $\text{C}_5\text{H}_4\text{O}_2$ ) and Kapton ( $\text{C}_{22}\text{H}_{10}\text{N}_2\text{O}_5$ ). After tests and simulations, it seems that Polyethylene is the best material, both for background suppression and a beam quality.

Since the range of muons (29 MeV/c) in Polyethylene is about 1.1 mm, a  $\text{CH}_2$  target of 150  $\mu\text{m}$  thick requires a  $\sim 700 \mu\text{m}$  thick polyethylene degrader to be placed along the beam line, in the beam transport solenoid. Since the target is slanted, the average muon path, in 150  $\mu\text{m}$ , is of the order of 400  $\mu\text{m}$ . The energy loss for positrons in a 150  $\mu\text{m}$  Polyethylene target is about 30 keV<sup>\*</sup>.

## 2.2. Photon detector

An innovative LXe scintillation detector, placed outside the magnet, detects the penetrating  $\gamma$ -rays. The detector holds an active volume of 0.8 m<sup>3</sup> LXe. Only the scintillation light from LXe is used, without attempting to collect the ionization. Scintillation light emitted inside LXe is viewed from all sides ( $4\pi$ ) by approximately 850 photomultiplier tubes (PMTs) which are immersed in LXe in order to maximize direct light collection.

As shown in Figure 2.4 , the MEG calorimeter cryostat is placed just outside the COBRA magnet. It has a “C” shape to minimize its volume with respect to the acceptance angle. This shape allows to have the photon impinging as perpendicular as possible on its front face. The surface of LXe is at 65 cm from the target center and its depth is 47 cm. The fiducial volume of the detector covers a solid angle of  $\Delta\Omega / 4\pi \sim 12\%$  ( $|\cos\theta| < 0.35$  and  $120^\circ$  in  $\phi$ ).

The photon parameters to be measured are energy, direction and timing. The energy is provided by the scintillation light collected by all PMTs. The photon is supposed to come from the same vertex of the “family” positron on the target. To determine the gamma incident position, it is important to define the size of an event, so that the reconstruction is minimally affected by shower fluctuations. In this way, the

---

\* Problems as the depolarization characteristics of these materials are being checked by PSI collaboration, taking into account the experience obtained by the previous experiments, MEGA and Crystal Box.

gamma incident position is reconstructed in two steps: first, find a peak position of light distribution by using the PMT's signal of the entrance face; second, determine more precisely the incident position using an iterative process. The light arrival time on all PMTs is used to extract the photon timing.

The high light yield of LXe, comparable to that of NaI(Tl), and its uniformity are necessary ingredients for a good energy resolution. The scintillation pulse from Xe is very fast and has a short tail<sup>7</sup>. This allows to minimize the pileup problem of high rate of  $\gamma$ -rays. In Table 2.2, the main characteristics of three liquid rare gases are listed. The high atomic number and low radiation length  $X_0$  of Xe, together with its high boiling temperature and the absence of radioactive isotopes make Xe the best choice for our scintillation detector.

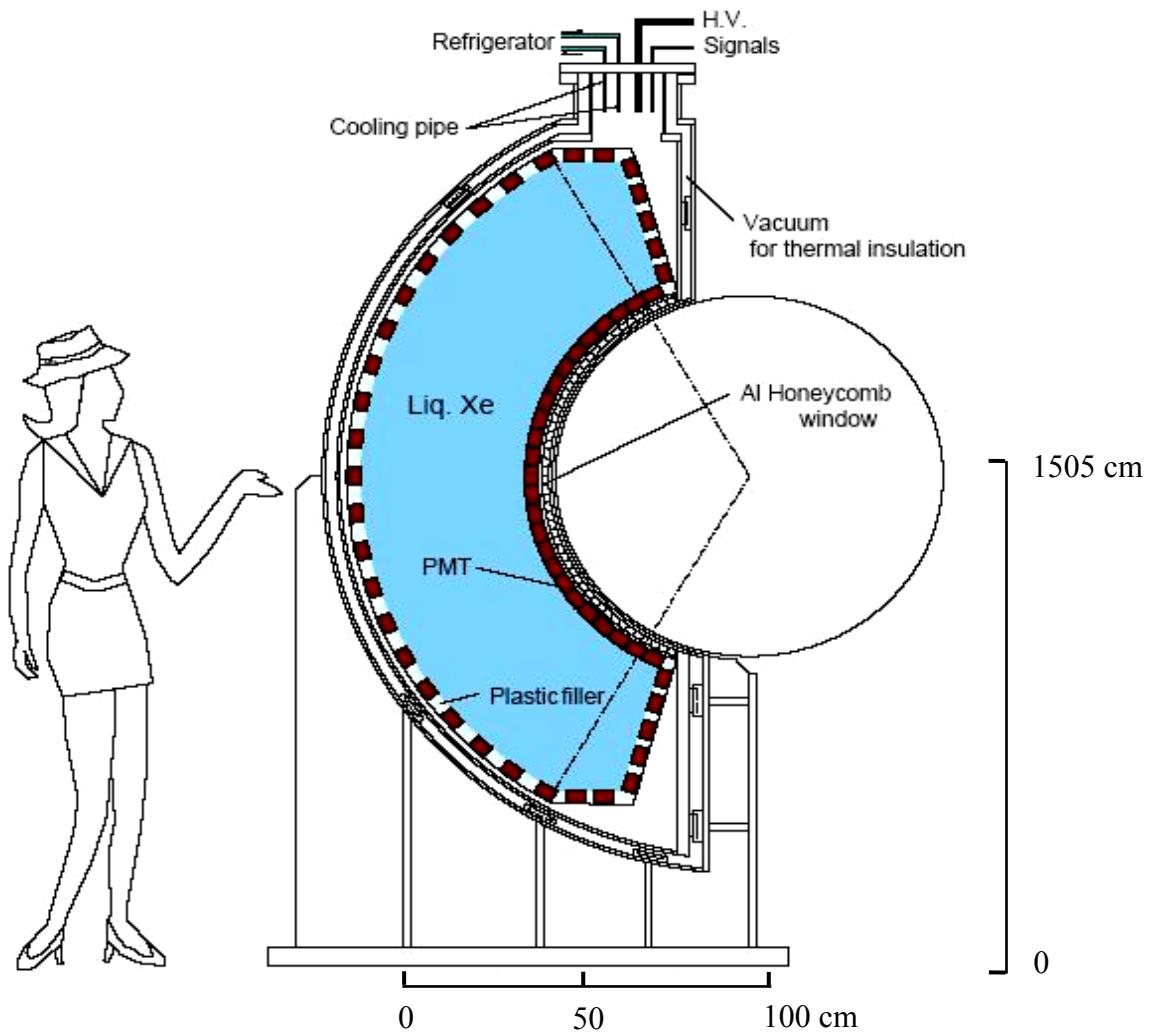


**Figure 2.4:** A cross-section view of LXe detector. The cryostat consists of a Xe vessel and a vacuum vessel for thermal insulation. Its front face is an aluminum honeycomb structure.

**Table 2.2:** Main characteristics of Ar, Kr and Xe<sup>8</sup>.

Liquid gases	Ar	Kr	Xe
density (g/cm <sup>3</sup> )	1.39	2.45	2.98
Z	18	36	54
Boiling point T(K)	87.3	119.9	167.1
dE/dx (m.i.p.) (MeV/cm)	2.11	3.45	3.89
X <sub>0</sub> (cm)	14.30	4.76	2.77
Wavelength (nm)	128	147	178

The major constraint of this innovative detector is the absorption of the scintillation light inside Xe. Impurities in Xe, such as water and oxygen, reduce the light absorption length  $\lambda_{\text{Abs}}$  and degrade the detector performance. To study and to improve the energy and time resolution of this detector, a small prototype of 0.1 m<sup>3</sup>, surrounded by more than 200 PMTs and called Large Prototype (LP), has been build and tested. PMTs, developed in cooperation with Hamamatsu Photonics, are sensitive to the UV scintillation light ( $\lambda = 178$  nm) and can operate at the LXe temperature ( $T \sim -100^\circ\text{C}$ ).

The first absorption length measurements in the Large Prototype indicated a length shorter than 10 cm. To remove the water contamination, an additional gas system was installed to circulate and purify Xe, with a gas getter purifier. The purification takes so long time because of large release of contaminants by the cable materials, PMTs and ancillaries. Light absorption was monitored by blue LEDs, cosmic-rays and alpha sources. After one month of circulation, light absorption length improved from 7 to more than 100 cm\*. Assuming a 100 cm absorption length, a Monte Carlo simulation predicts an average energy resolution of 5% for  $\gamma$ -rays uniformly entering the detector with energy of 52.8 MeV. This value can be improved to 4% by exploiting the knowledge of the photon conversion point.<sup>9</sup>

---

\* The impurity density can be expressed as a function of time:  $C(t) = C_0 \exp(-\frac{t}{\tau})$ , where  $C_0$  is the initial value of the impurity density in the vessel and  $\tau$  is the time constant of the purification cycle. Consequently, the absorption length caused by this impurity has the same time constant, and can be written as:  $\lambda(t) = \lambda_0 \exp(-\frac{t}{\tau})$  where  $\lambda_0$  is the initial value of the absorption length.

During the MEG experiment run, several methods (described in Chapter 5) will be used to calibrate and monitor the stability of calorimeter, for example to study the time dependent attenuation length for the scintillation light or to monitor the quantum efficiencies of all PMTs; all these items are necessary to control the energy and time resolution. A detailed description of the whole detector calibration techniques is reported in Dussoni's Ph.D. thesis<sup>10</sup>.

## 2.3. Positron detector

The positron detector consists of three parts: a magnet specially designed to provide a gradient field, a drift chamber to measure the positron momentum and two scintillation counters to measure the positron timing.

### 2.3.1. COBRA magnet

In general, the aim of a solenoidal magnetic field is to confine low momentum tracks within a certain radius. In this way, in muon decay a large fraction of Michel positrons do not reach the track detectors located at large radii. However, as shown in Figure 2.5, in a conventional solenoid, positrons with high transverse momentum ( $p_t$ ), emitted close to  $90^\circ$  with respect to the solenoid axis, make many turns in the drift chambers and degrade the detector performance. Furthermore, the bending radius of positrons with a given absolute momentum is determined by its  $p_t$ , which makes difficult to select the positron by momentum reconstruction. This was the choice on the MEGA experiment, who suffered of the trapping of positrons emitted at large angles.

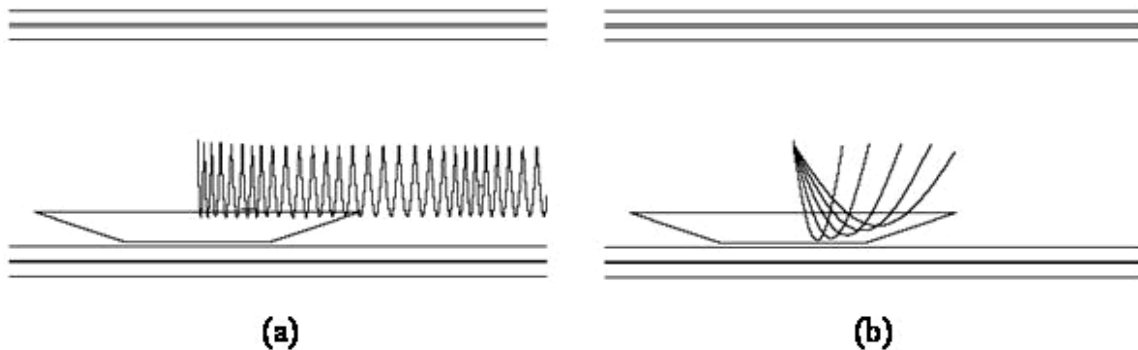


**Figure 2.5:** Particle trajectory in a uniform solenoidal magnetic field: (a) r-z view of the solenoid shown with the trajectory of a particle emitted at  $88^\circ$  making several turns inside the detector; (b) Trajectories of monochromatic particles emitted at various angles. The bending radius depends on the emission angle.

To avoid these problems, the COBRA positron spectrometer was designed to provide a graded magnetic field whose flux lines have a large divergence also in the center (1.27 T at the center and 0.49 T at both ends). As shown schematically in Figure 2.6, positrons with the same absolute momentum follow trajectories with a constant projected bending radius, independent on the emission angles over a wide angular range. This allows to sharply discriminate high momentum signal positrons emitted from the target ( $p = \frac{m_\mu}{2} = 52.8 MeV/c$ ). Only high momentum positrons enter the drift chamber volumes. The graded field also helps to sweep away positrons with high  $p_t$  from the detector center, after one or two turns in the drift chamber zone, thereby reducing accidental pile up of the Michel positrons.

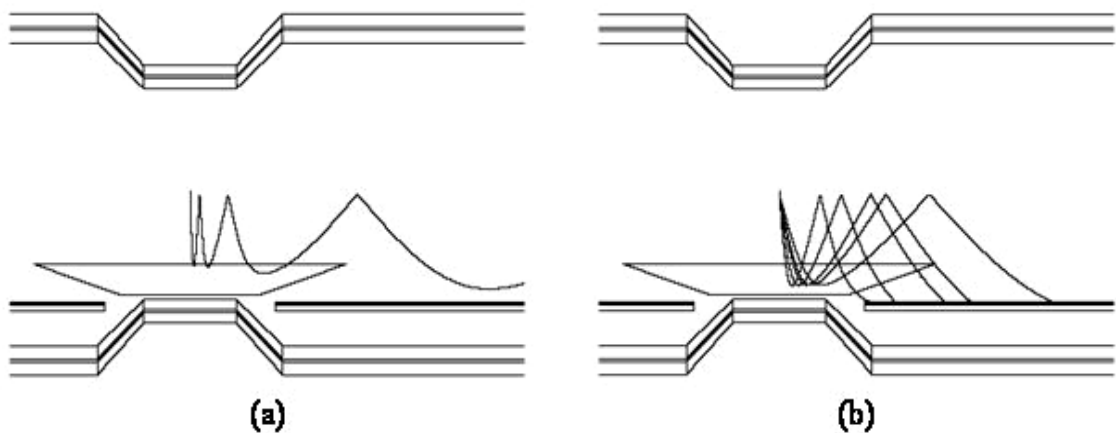


**Figure 2.6:** Advantages of a gradient magnetic field: (a) r-z view of the COBRA spectrometer shown with the trajectory of a particle emitted at  $88^\circ$ . The particle is swept away much more quickly than in Figure 2.5(a); (b) Trajectories of monochromatic particles emitted at various angles. The bending radius is independent on the emission angle<sup>1</sup>.

In Figure 2.7 is shown the rate of Michel positrons as a function of radius (for a muon decay rate of  $1 \times 10^8$ ) indicating that by placing the drift chambers at a radius larger than 20 cm, the counting rate can be contained to a level below the limit of stable chamber operation.

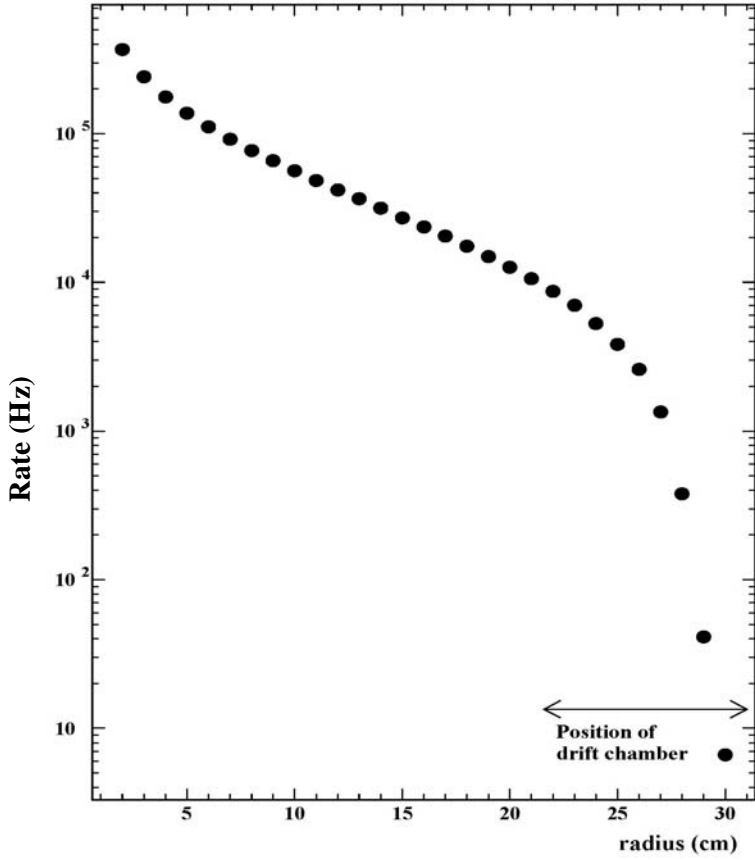


**Figure 2.7:** Rate of Michel positrons per square centimeter per second as a function of radius of the magnet.

The COBRA magnet was designed in order to be as transparent as possible to 52.8 MeV  $\gamma$ -rays, directed towards the photon calorimeter. It is composed by five coils of three different radii: a central coil, two gradient coils and two end coils. A high strength 1.2 mm aluminum stabilized superconducting cable was developed for the COBRA magnet, consisting of a NbTi multi-filament embedded in a copper matrix and an aluminum stabilizer. The current density variation in the coils is obtained by varying the winding pitch, the number of winding layers and the orientation of the superconducting wire<sup>11</sup>. The superconductivity windings are cooled by means of mechanical cryocoolers.

To reduce the stray-field in the calorimeter zone, which could degrade the performance of photomultipliers, a pair of compensation coils will be used. The suppression of the stray magnetic field occurs below 50 Gauss in the proximity of the  $\gamma$ -ray detector (see Figure 2.8).

The total equivalent thickness of the central part of the magnet is  $3.83 \text{ g/cm}^2$  which corresponds to 0.197 radiation length. Therefore, the conversion probability of the magnet for a 52.8 MeV photon is 15%, i.e. 85% of  $\gamma$ -rays pass through the magnet without any interaction before entering the  $\gamma$ -ray detector. The COBRA magnet was built by Toshiba-Japan and placed in the  $\pi$ E5 area during 2004. Various tests, including full excitation and quenching were already carried out with successful results. Also a precise mapping of the magnetic field showed a well-defined graded magnetic field as designed and successful field suppression at the  $\gamma$ -ray detector position.

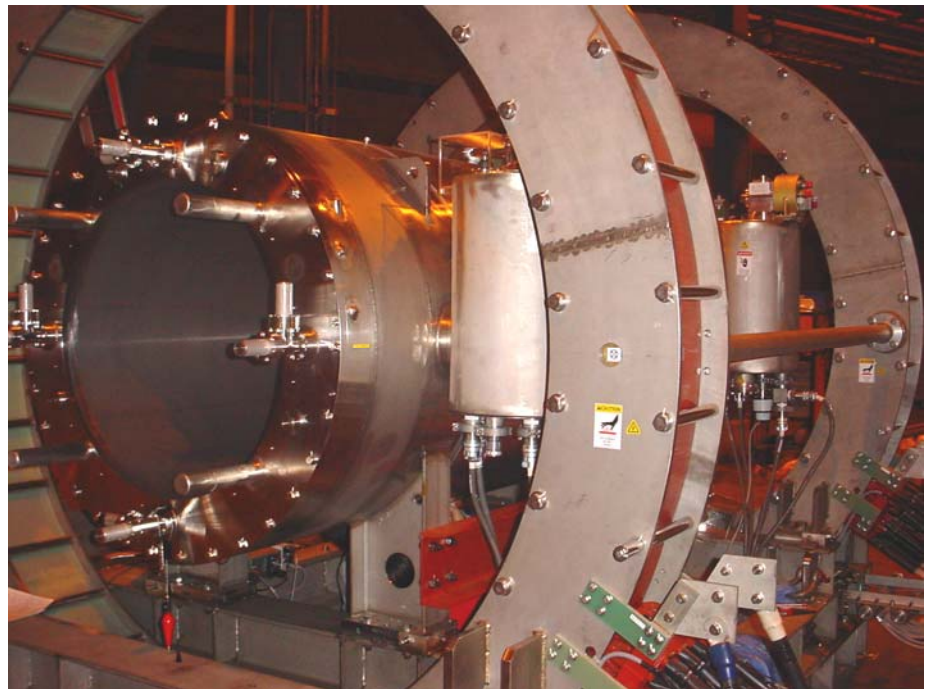


**Figure 2.8:** The COBRA magnet. Two large coils around the main magnet are to compensate and suppress the magnetic field at the LXe detector.

### 2.3.2. Drift chambers

Positrons tracks are measured with sixteen trapezoidal drift chambers shaped as sectors and aligned radially with  $10^\circ$  intervals in azimuthal angle. Each sector consists of two staggered arrays of drift cells, as show in Figure 2.9. The sensitive area of the chamber covers a radius from 19.3 to 27.0 cm. In the z-direction, the active area extends up to  $z = \pm 50$  cm at the innermost radius and  $z = \pm 21.9$  cm at the outermost one.

Consequently, positrons of 52.8 MeV emitted from the target with  $|\cos\theta| < 0.35$  and  $-60^\circ < \phi < 60^\circ$  are covered by this geometry, as mentioned in 2.2. The chamber walls are made of thin plastic foils. A thin layer of aluminum deposit on the four cathode foils is shaped to make a so called Vernier pad.

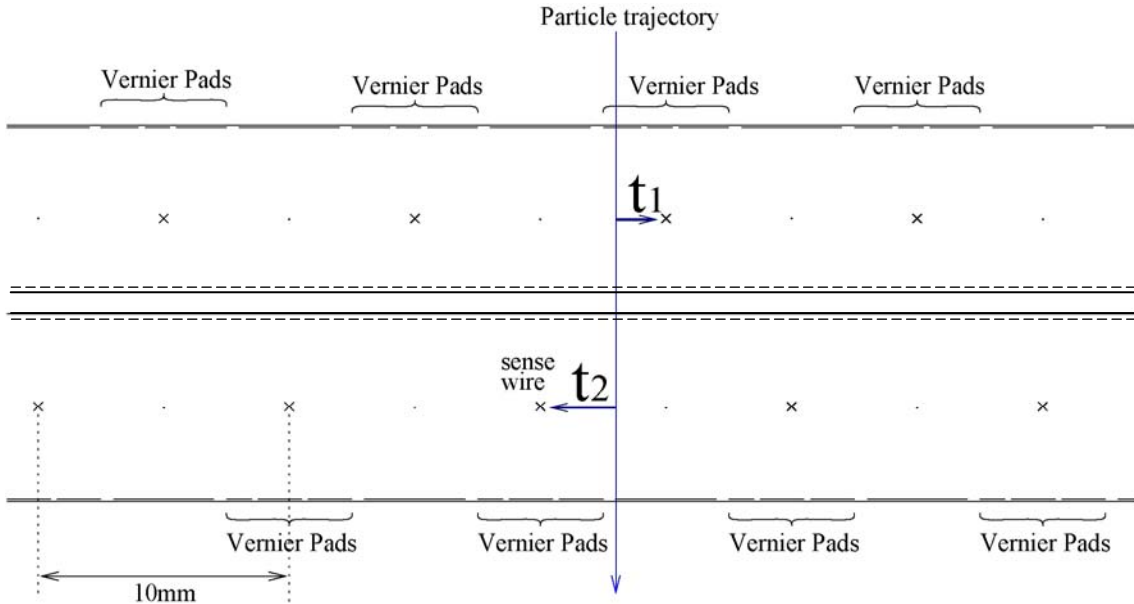


**Figure 2.9:** Cross-section view of a part of a chamber sector. It consists of two layers of drift cells staggered by a half cell<sup>1</sup>.

The configuration of the cells allows to measure simultaneously the radial coordinate ( $r$  coordinate) and the absolute time of the track. The difference between the drift time ( $t_1 - t_2$ ) in two adjacent cells gives the  $r$ -coordinate of the track, with an accuracy of  $\sim 150 \mu\text{m}$ , while the average  $(t_1 + t_2)/2$  gives the absolute time of the track with  $\sim 5 \text{ ns}$  accuracy. This high timing resolution is important for the pattern recognition. The ratio of charges observed at both ends of a sense wire allows to define, in the first step, the  $z$  coordinate along the wire with an accuracy of  $\sim 1 \text{ cm}$ . Comparing the charges induced on the Vernier pads of each cell, it is possible to refine the  $z$  coordinate determination with an accuracy of about  $300 \mu\text{m}$ <sup>[12]</sup>.

The chambers are filled with a gas mixture of Helium (50%) and Ethane (50%). This mixture was chosen to have sufficient ionization loss in the gas and to minimize the multiple Coulomb scattering of tracks. In fact, the momentum and angular

resolutions of the spectrometer are primarily limited by multiple scattering in the gas and also by the chamber material.

The expected resolutions of the drift chamber have been studied with GEANT simulations by incorporating detailed material distribution. Positrons of 52.8 MeV were generated and their trajectories reconstructed using several methods. The fractional momentum resolution and the FWHM angular resolution turns out to be  $\frac{\Delta E_e}{E_e} = 0.9\%FWHM$  and 12 mrad, respectively. The positron origin on the target can be

reconstructed with a 2.5 mm resolution. To obtain information on the performance of the proposed chambers, several prototypes are being built and tested at PSI. The final spectrometer will be placed inside the COBRA and tested in June 2006.

### 2.3.3. Timing counter: conceptual design

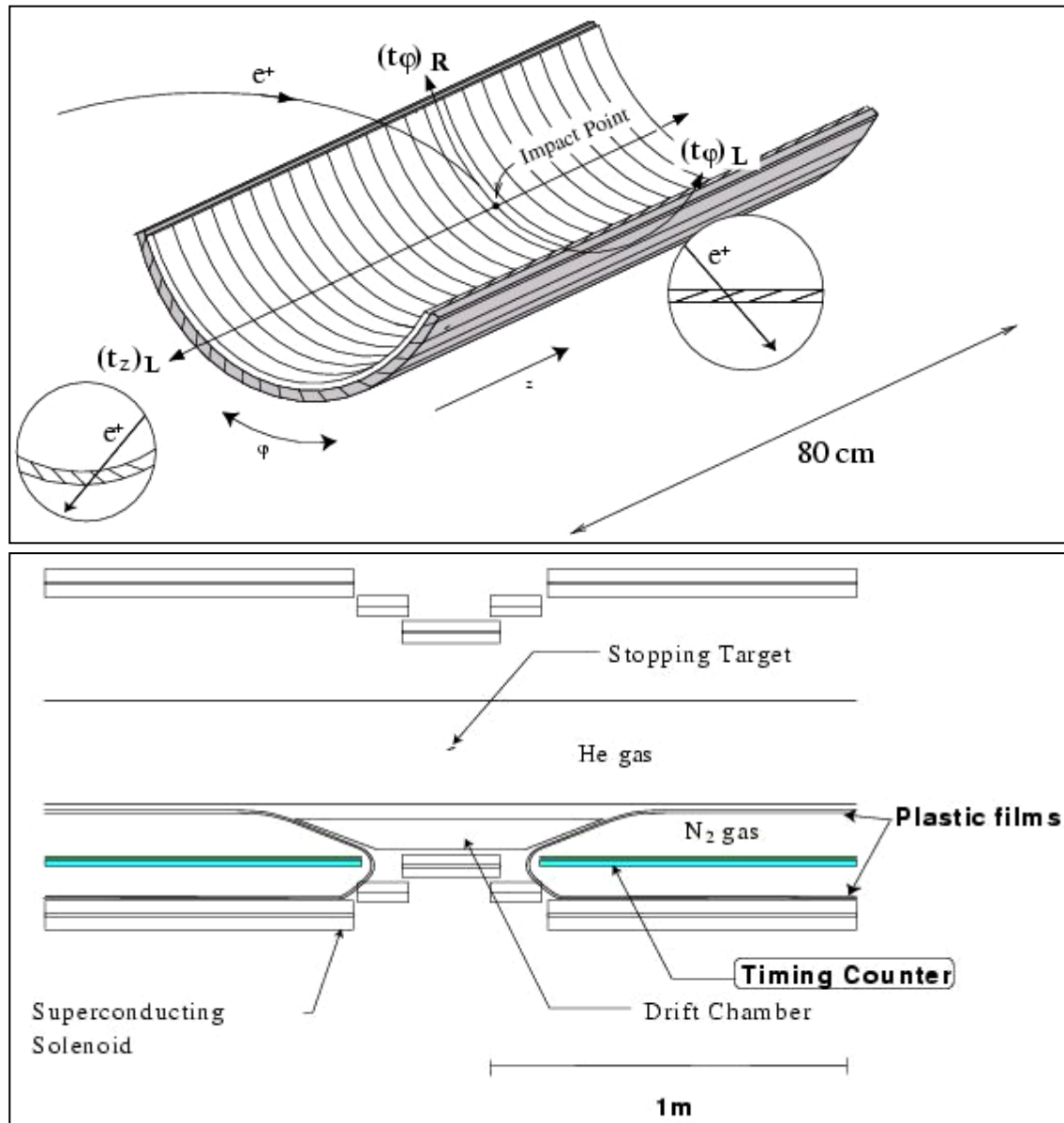
This detector is designed to measure the positron timing with a FWHM resolution of 100 ps and to be used in the trigger, for selecting events containing a positron coincident in time and collinear in direction with a photon, identified in the electromagnetic calorimeter. It also provides a fast determination of the positron direction. Hodoscope arrays are placed on both sides of the drift chambers at a radius of 31.9 cm, covering  $157.5^\circ$  in  $\phi$  and their position along the beam is  $27.6 \text{ cm} < |z| < 108.0 \text{ cm}$ . The  $\mu \rightarrow e \gamma$  positrons emitted in the angular range  $0.08 < |\cos \theta| < 0.35$  hit the timing counter after completing about 1.5 turns in the  $r\phi$  plane\*.

Figure 2.10 shows the conceptual design of the timing counters. These are two cylindrical shaped detectors symmetrically placed with respect to the  $z = 0$  plane, up-stream  $z < 0$  and down-stream  $z > 0$ , in the COBRA bore. The first conceptual design was based on two layers of plastic scintillator bars orthogonally placed along the  $z$  and  $\phi$  directions. The bars of the outer layer (longitudinal) are approximately 80 cm long. Each scintillator bar is viewed at both sides by photomultiplier tubes which measure the pulse heights and the arrival time of the scintillation light ( $t_L$  and  $t_R$ ) at both ends. The

---

\* The  $z$ -axis represents the beam direction. The plane perpendicular to this direction is called the  $r\phi$  plane.

time difference  $t_L - t_R$  provides a measurement of the impact point along the scintillator, while the mean time  $(t_L + t_R)/2$  gives the absolute impact time. The inner (curved) layer is mainly used for trigger purposes, while the outer layer provides the positron timing.



**Figure 2.10:** (top) The timing counter configuration, (bottom) the layout of positrons timing counter in the MEG detector.

In order to avoid the PMTs working in the helium atmosphere inside COBRA, the area surrounding the timing counters will be separated with a plastic bag, as shown in Figure 2.10 (bottom). This Nitrogen-bag will assure a longer PMTs life time.

Before our contribution, a couple of prototypes have been tested at KEK (Japan) in 1999<sup>[13]</sup> and repeated in Pisa in 2001<sup>[14]</sup>, using cosmic-ray muons, to investigate the possibility of achieving the required timing resolution of 100 ps. A 1 m long scintillator bar was used, with cross section  $5 \times 1 \text{ cm}^2$ , wrapped with 50  $\mu\text{m}$  of aluminized Mylar and coupled to PMTs through light guides, at the two opposite ends. Philips XP2020UR photomultiplier tubes, with a transit time spread of 350 ps FWHM<sup>[15]</sup>, were used. In these conditions, the obtained results were a factor 1.5–2 higher than 100 ps FWHM.

This thesis work concerns the design study, prototyping and realization of the timing counter detector, performed at PSI and in Frascati. The results will be presented in the following chapters.

## 2.4. Trigger and data acquisition system

Detailed simulation studies have been performed in order to obtain an estimate of the final acquisition rate expected in the experiment. Background from the accidental coincidence of photons (from the muon radiative decay or positron annihilation in flight) and Michel positrons have been considered. A complete GEANT simulation of the proposed experimental set-up was used. The selections based on the photon and positron kinematic variables, which could be used in the trigger at various levels, were studied.

The information available at the trigger level comes from the LXe detector and from the timing counter\*. The signal from the drift chambers is available with some delay  $\sim 100$  ns, due to the electron drift time in the cells, therefore the drift chambers cannot be used for a fast first level trigger.

The photon energy is determined by the sum of the light collected by all PMTs, while its direction is determined by the position of PMT with the largest signal, which is

---

\* Note that the  $\mu \rightarrow e \gamma$  decay is a back-to-back photon-positron pair coincident in time. Therefore the experiment trigger requires the presence of two high energy particles with opposite momenta.

sufficient for trigger purposes. By setting a threshold level of at least a 45 MeV equivalent energy release in the LXe calorimeter, the estimated trigger rate is given by:

$$R_\gamma = R_\mu f_\gamma \frac{\Omega}{4\pi} = 2.4 \text{ kHz},$$

where  $R_\mu = 10^8 \mu^+/\text{s}$  is the muon stopping rate, the solid angle fraction ( $\Omega/4\pi$ ) is 12% and  $f_\gamma \sim 2 \cdot 10^{-4}$  is the fraction of background photons per stopped muon that satisfies this selection criterion.

The positron time coincidence is provided by the timing counters. The radial position excludes most of low momentum positrons, as showed in Figure 2.7. The overall rate due to Michel positrons, in the single timing counter, is estimated to be  $R_{TC} = 2 \times 10^6 \text{ Hz}$ . For the accidental background, the corresponding rejection factor is  $f_\phi \sim 5$ , due to the correlation between positron direction and photon.

Therefore, the presence of a hit in the timing counter, within a time coincidence window of  $\Delta T = 10 \text{ ns}$  and spatially aligned with the measured photon direction, reduces the uncorrelated background event rate to:

$$R_{trig} = 2\Delta T R_\gamma \frac{R_{TC}}{f_\phi} \left( \frac{R_\mu}{10^8} \right)^2 = 20 \left( \frac{R_\mu}{10^8} \right)^2.$$

The estimated trigger rate provides some margin in the case of other possible contributions to the background which are not presently taken into account, e.g. photons coming from the experiment shielding.

The trigger system is based on a fast logic processor built with Field Programmable Gate Arrays (FPGAs) on Virtual Machine Environment (VME) boards. The trigger inputs are the digitized signals of the LXe and timing counter PMTs. This allows complex trigger solutions and improvements during the execution of the experiment. For instance, it allows the corrections to each PMT signal: the different PMTs gains can be taken into account and the baseline of each signal can be subtracted. This is essential to estimate the energy deposited in the Xe calorimeter by using the sum of the light seen by all the PMTs. The clock frequency of the trigger system is 100 MHz.

Being MEG a high rate experiment, the pile-up discrimination efficiency is a crucial parameter\*. In order to maximize it, it was proposed to digitize each signal for a carefully off-line analysis. Consequently, the signals from all PMTs and from the drift chambers will be individually digitized by a custom chip, called Domino Ring Sampler (DRS). The DRS consists of a bank of 1024 analogical sample and holder (SH) which strobe signal is generated by a so called domino wave signal, which runs continuously in a circuital loop. When a trigger occurs, the domino-wave is stopped and the charges collected on all capacitors are sequentially readout and digitized. This digitization method constitutes a sort of analog pipeline. The signals will be digitized at 2 GHz (500 ps sampling period) in order to be able to obtain a timing resolution of 50 ps via bin interpolation, necessary for the positron timing counter and for the LXe calorimeter.

Waveform digitizing on all channels gives an excellent handle on event pile-up and noise suppression, although the amount of data per event is large:  $\sim 1.6$  MB, using a stopping muon rate  $R_\mu = 3 \cdot 10^7 \mu^+/\text{s}$ . Studies are under way to reduce or compress the data.

For the  $\mu^+ \rightarrow e^+ \gamma$  experiment, the Data Acquisition (DAQ) is based onto the software framework, called MIDAS DAQ system<sup>16</sup>, which has been successfully used in other experiments<sup>17</sup> and has now become the standard system at PSI. Besides all the necessary means of data readout, transport and storage, MIDAS contains a full slow control system, an integrated data analysis functionality and a Web interface for remote control. The slow control system includes the measurement and control of environment variables such as temperature, pressure and humidity, as well as the control of high voltage channels (more than 900) for PMTs, wire chambers, superconducting solenoid and LXe calorimeter.

## 2.5. Background and sensitivity

Looking at the past history of the experimental research (see Table 2.3) on  $\mu^+ \rightarrow e^+ \gamma$  decay made at the muon beams, it is clear that the limit on the Branching Ratio essentially improves as the number of observed muons, as reported in Figure 2.11. The

---

\* Since the liquid Xe calorimeter has a homogeneous volume, it is possible that two or more low energy photons entering the detector are reconstructed as a single high energy photon.

best the detector is able to discriminate a signal-event from the background, composed by particles that simulate the  $\mu^+ \rightarrow e^+ \gamma$  decay, the best is the sensitivity. Increasing the muon rate, the number of background events increase drastically. Experimental efforts have been devoted to the improvement of detection resolutions of four variables, namely the positron energy  $E_e$ , the photon energy  $E_\gamma$ , the timing between the positron and photon  $\Delta t_{e\gamma}$  and the angle between the positron and photon direction  $\Delta\theta_{e\gamma}$ .

In Table 2.3 is summarized the historical progress of the  $\mu^+ \rightarrow e^+ \gamma$  search and in Figure 2.11 a graphical view of the branching ratio (BR) limit as a function of the year is shown.

**Table 2.3:** Chronology of  $\mu^+ \rightarrow e^+ \gamma$  searches since the era of meson factories with 90% C.L. (Confidence Level) upper limits. The resolutions quoted are given as a full width at half maximum (FWHM).

Accelerator	Year	$\Delta E_e/E_e$	$\Delta E_\gamma/E_\gamma$	$\Delta t_{e\gamma}$	$\Delta\theta_{e\gamma}$	Limit
TRIUMF <sup>18</sup>	1977	10%	8.7%	6.7 ns	-	$<3.6 \times 10^{-9}$
SIN <sup>19</sup>	1980	8.7%	9.3%	1.4 ns	-	$<1.0 \times 10^{-9}$
LANL <sup>20</sup>	1982	8.8%	8%	1.9 ns	37 mrad	$<1.7 \times 10^{-10}$
LANL <sup>21</sup>	1988	8%	8%	1.8 ns	87 mrad	$<4.9 \times 10^{-11}$
LANL	1999	1.2%	4.5%	1.6 ns	15 mrad	$<1.2 \times 10^{-11}$

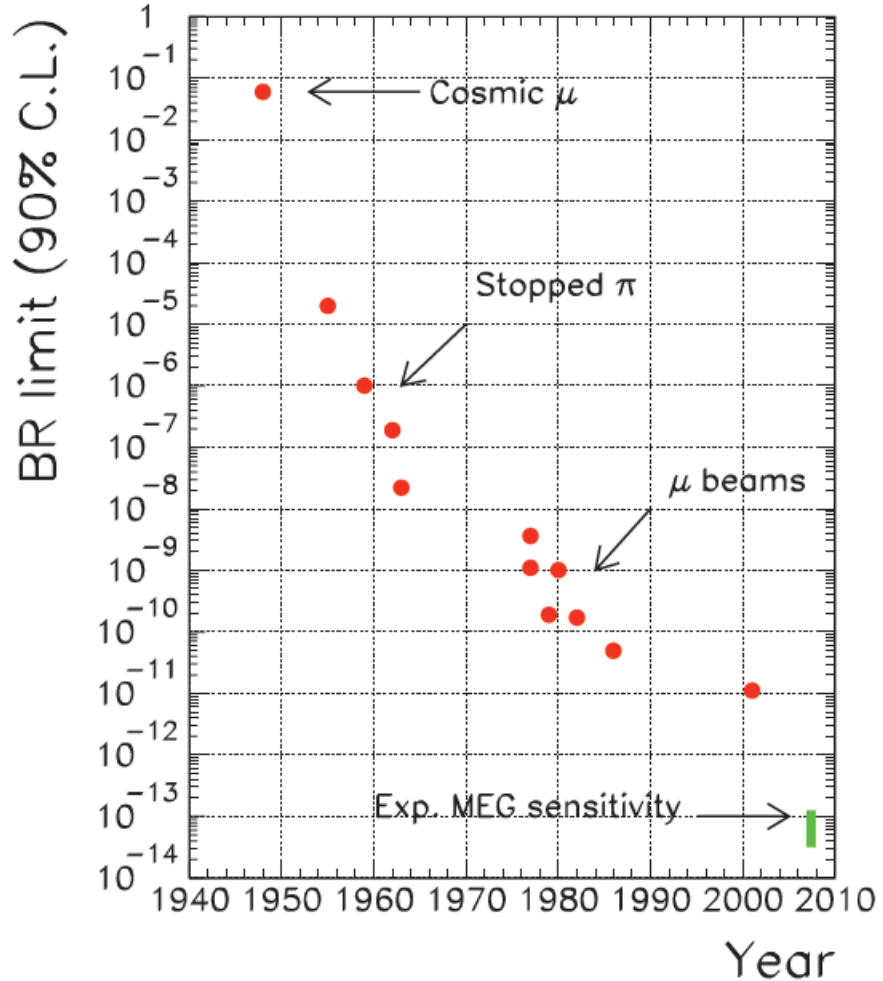


**Figure 2.11:** Improvement of the branching ratio along the years and the innovations in muon source and technological instrumentation.

Consequently, the efficiency of new experimental apparatus depends directly on the background rejection capabilities. For this reason, a brief description of the main background sources in the  $\mu^+ \rightarrow e^+ \gamma$  decay is done. There are two major backgrounds in the  $\mu^+ \rightarrow e^+ \gamma$  experiment:

- prompt or physics background; coming from radioactive muon decay ( $\mu^+ \rightarrow e^+ + \nu_e + \bar{\nu}_\mu + \gamma$ ) when the positron and the photon are emitted back-to-back with a small energy of the two neutrinos;
- accidental background; arising from the accidental coincidence of a positron in a normal muon decay ( $\mu^+ \rightarrow e^+ + \nu_e + \bar{\nu}_\mu$ ), accompanied by a high energy

photon. The sources might be either radiative decay, annihilation in flight or external bremsstrahlung of positrons from normal muon decay.

The background rejection strictly depends on detector performance. With the expected performances of MEG detector, summarized in Table 2.4, the accidental background prevails over the prompt one, as will be showed in the following chapters.

**Table 2.4:** Resolution of the various kinematical quantities for the MEG experiment.

	Resolution	Value
Photon energy	$\Delta E_\gamma/E_\gamma$	5%
Positron energy	$\Delta E_e/E_e$	0.9%
Relative timing	$\delta t_{e\gamma}$	105 ps
Relative angle	$\delta \theta_{e\gamma}$	23 mrad

### 2.5.1. Physics background

One of the major physics background is the radiative muon decay, ( $\mu^+ \rightarrow e^+ + \nu_e + \bar{\nu}_\mu + \gamma$ ; with branching ratio = 1.4 % for  $E_\gamma > 10$  MeV). The differential decay width of this radiative decay has been calculated as a function of the positron ( $E_e$ ) and photon energy ( $E_\gamma$ ) normalized to their maximum energies:  $x = \frac{2E_e}{m_\mu}$  and  $y = \frac{2E_\gamma}{m_\mu}$ ; therefore the kinematical ranges are  $0 \leq x, y \leq 1$ <sup>[22,23]</sup>. As a background to  $\mu^+ \rightarrow e^+ \gamma$ , the kinematic case of  $x \sim 1$  and  $y \sim 1$  is important. In this approximation and with an angle between positron and photon ( $\theta_{e\gamma}$ ) of almost 180° the differential decay width of  $\mu^+ \rightarrow e^+ + \nu_e + \bar{\nu}_\mu + \gamma$  is given by<sup>24</sup>:

$$d\Gamma(\mu^+ \rightarrow e^+ \nu \bar{\nu} \gamma) \approx \frac{G_F^2 m_\mu^5 \alpha}{3 \cdot 2^8 \pi^4} \left[ (1-x)^2 (1 - P_\mu \cos \theta_e) + (4(1-x)(1-y) - 0.5z^2) \cdot (1 + P_\mu \cos \theta_e) \right] \cdot dx dy dz d(\cos \theta_e)$$

where  $\theta_e$  is the angle between the muon spin and the positron momentum direction,  $G_F$  is the Fermi coupling constant,  $\alpha$  is the fine structure constant,  $z = \pi - \theta_{e\gamma}$  and  $P_\mu$  is the muon polarization.

When  $x = 1$  and  $y = 1$  exactly, this differential decay width vanishes. However, experimentally, finite detector resolutions introduce background events which would ultimately limit the sensitivity of a search for  $\mu^+ \rightarrow e^+ \gamma$ . The physics background was calculated using the expression:<sup>25</sup>

$$dB(\mu^+ \rightarrow e^+ \nu \bar{\nu} \gamma) = \frac{1}{\Gamma(\mu^+ \rightarrow e^+ \nu \bar{\nu})} \int_{1-\delta x}^1 dx \int_{1-\delta y}^1 dy \int_0^{\min[\delta z, 2\sqrt{(1-x)(1-y)}]} dz \frac{d\Gamma(\mu^+ \rightarrow e^+ \nu \bar{\nu} \gamma)}{dxdydz}.$$

By numerical integration over the selection cuts, 90% efficient cuts were applied on the four quantities, which correspond to 1.4 FWHM for Gaussian distribution of the variables. A background of  $\sim 3 \times 10^{-15}$  events per muon decay can be obtained, for the resolution values from Table 2.4.

### 2.5.2. Accidental background

For a very high rate of incident muons, the accidental background becomes more important with respect to the physics background. This is the case for the present experiments. The event rate of the accidental background ( $B_{acc}$ ), normalized to the total decay rate can be obtained by:

$$B_{acc} = R_\mu \cdot f_e^0 \cdot f_\gamma^0 (\Delta t_{e\gamma}) \cdot \left( \frac{\Delta \omega_{e\gamma}}{4\pi} \right), \quad (2.1)$$

where  $R_\mu$  is the instantaneous muon intensity,  $f_e^0$  and  $f_\gamma^0$  are an integrated fraction of the spectrum of positrons in the normal muon decay, and of photon in the radiative muon decay, within the signal region, respectively. They include their corresponding branching ratios. The terms  $\Delta t_{e\gamma}$  and  $\Delta \omega_{e\gamma}$  are the full widths of the signal regions for the timing coincidence and angular constraint of the back-to-back kinematics, respectively.

Given the sizes of the signal region,  $B_{acc}$  can be estimated; by taking  $\delta x$ ,  $\delta y$ ,  $\delta \theta_{e\gamma}$ , and  $\delta t_{e\gamma}$  to be the half width of the signal region for positron and photon energies,

of the angle  $\delta\theta_{e\gamma}$  and of the relative timing between positron and photon, respectively. Then  $f_e^0$  can be estimated by integrating the Michel spectrum of the normal muon decay in the interval  $(1 - \delta x) \leq x \leq 1$ , yielding  $f_e^0 \sim 2(\delta x)$ , since the Michel spectrum is constant at  $x \sim 1$ . Given the angular resolution,  $\delta\theta_{e\gamma}$ , the back-to-back resolution is given by  $\left(\frac{\Delta\Omega_{e\gamma}}{4\pi}\right) = \frac{(\delta\theta_{e\gamma})^2}{4}$ . As for  $f_\gamma^0$ , if the radiative muon decay is considered as a source of the 52.8 MeV photon, it can be given by integrating the photon energy spectrum within the width of the signal region  $(1 - \delta y) \leq y \leq 1$ . The expression is given by<sup>25</sup>

$$f_\gamma^0 \approx \left(\frac{\alpha}{2\pi}\right)(\delta y)^2 [\ln(\delta y) + 7.33].$$

The equation shows that  $f_\gamma^0$  is roughly proportional to  $(\delta y)^2$ .

The other sources of high-energy photons are annihilation in flight of positrons in normal muon decay and external bremsstrahlung. The contribution from annihilation of positrons in flight depends on the materials along the positron's track path. Figure 2.12 shows, for instance, the contribution of annihilation in flight for the case of positrons which passing through a muon-stopping target of Mylar, thick 150  $\mu\text{m}$ . It indicates that the contribution from the target is smaller than the radiative muon decay, and it becomes important only if the photon energy resolution becomes extremely high.

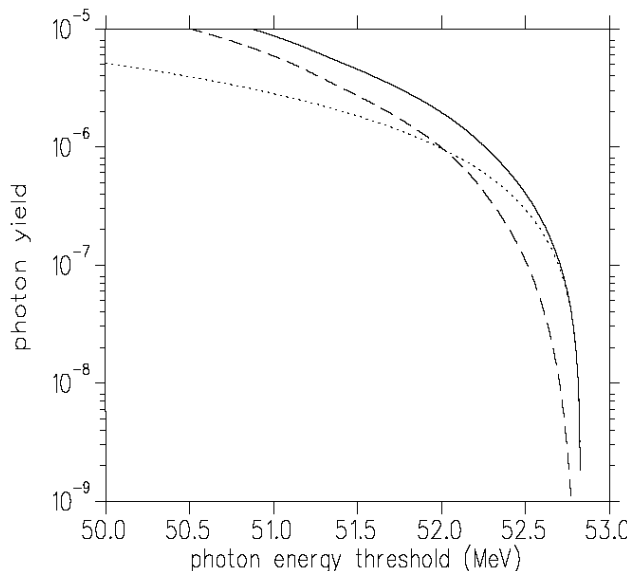


**Figure 2.12:** Integrated rates of backgrounds: (dotted line) from annihilation in flight; (dashed line) from radiative muon decay, as a function of the photon energy. The solid line shows the sum of the two.

However, it is dependent on the total amount of material in the experimental setup. Therefore, the effective branching ratio of accidental background is given by:

$$B_{acc} = R_\mu \cdot (2\delta x) \cdot \left[ \frac{\alpha}{2\pi} (\delta y)^2 (\ln(\delta y) + 7.33) \right] \times \left( \frac{\delta \theta^2}{4} \right) \cdot (2\delta t). \quad (2.2)$$

Figure 2.13 shows  $B_{acc}$  as a function of the positron and photon energy resolution ( $\delta x$ ,  $\delta y$  respectively) for a muon rate of  $2.2 \times 10^7 \mu/\text{s}$ . Based on Table 2.4, the contribution of the accidental background to the branching ratio is in the region of  $10^{-14}$ . In Figure 2.14 is shown the expected number of background events as a function of the muon rate  $R_\mu$  and of the measuring time,  $t$ , for the resolution assumed. The choice of  $R_\mu$  and  $t$  is dictated by a compromise between the need to perform the experiment in a reasonable time and that of having good single event sensitivity. If a number of 0.5 accidental background events are wanted, one must move along the corresponding dotted line shown in Figure 2.14.

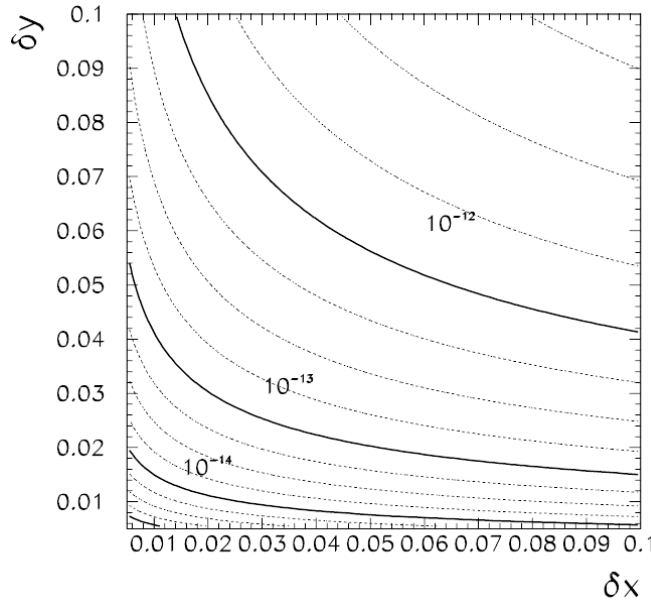


**Figure 2.13:** Accidental background curves for different values of the photon and positron energy resolution at  $R_\mu = 2.2 \times 10^7 / \text{s}$ <sup>[9]</sup>.

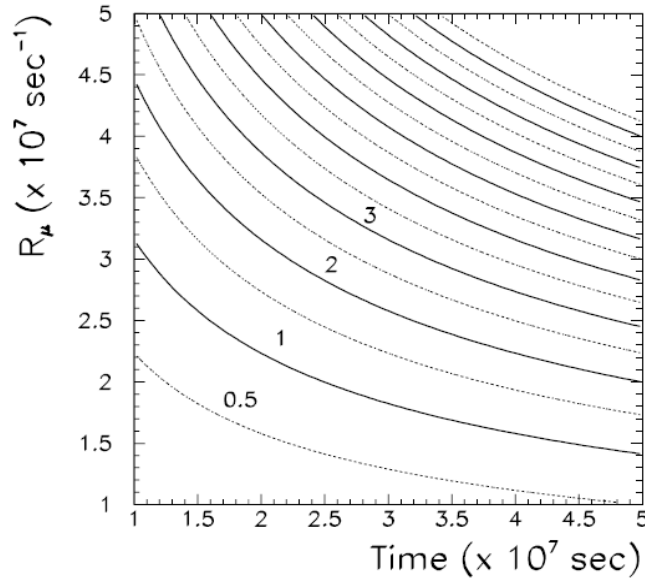


**Figure 2.14:** Number of expected background events as a function of the muon stopping rate  $R_\mu$  and measuring time  $t$ , for the resolution quoted.

### 2.5.3. Sensitivity

The detector acceptance defined by the positron spectrometer and the LXe calorimeter is  $0.08 < |\cos \theta| < 0.35$  and  $-60^\circ < \phi < 60^\circ$ , amounting to  $\Delta\Omega / 4\pi \sim 12\%$ , assuming identical values for photon and positron detector. The single event sensitivity (SES) of the MEG experiment is defined as the  $\mu^+ \rightarrow e^+ \gamma$  branching ratio for which the number of expected decays is equal to one. For a given branching ratio  $B_{\mu^+ \rightarrow e^+ \gamma}$  the number of observed events can be written as:

$$N_e = R_\mu T \frac{\Delta\Omega}{4\pi} \varepsilon_e \varepsilon_\gamma \varepsilon_{sel} B_{\mu^+ \rightarrow e^+ \gamma}, \quad (2.3)$$

where  $\varepsilon_e$  and  $\varepsilon_\gamma$  are the positron and photon detection efficiencies, 90% and 65% respectively, and  $\varepsilon_{sel}$  is the efficiency of the selection cuts. In MEG experiment, selection events covering 90% of the signal, corresponding to 1.4 FWHM for Gaussian distribution, are considered to be applied on the reconstructed positron energy, photon energy, opening angle and relative timing. Therefore, the selection cuts are dependent on the detector resolution.

The single event sensitivity is shown in Figure 2.15 as a function of the muon rate and running time. Comparing this plot with that of Figure 2.14, the optimum choice of  $R_\mu = 1.2 \times 10^7 \mu/\text{s}$  and  $T = 3.5 \times 10^7 \text{ s}$ , yielding a SES of  $6 \times 10^{-14}$ .

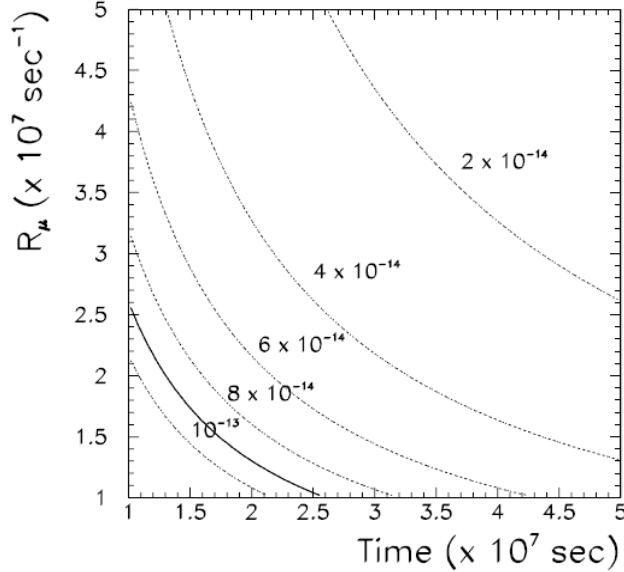


**Figure 2.15:** Single event sensitivity as a function of the muon rate and running time.

For a given number of background events, it is more convenient to run for a long time at low beam intensity, since the single event sensitivity increases, as shown previously with the  $R_\mu^2$  dependence of the accidental background. On the basis of the studies performed, the proposed detector will allow to reach this sensitivity and consequently, using the Feldman-Cousins<sup>26</sup> statistical analysis of small signals, a branching ratio of  $\sim 1.2 \times 10^{-13}$  90% C.L. upper limit in case of no-signal observed. However, further improvement is possible and only the operation of the experimental apparatus will enable to understand what the final sensitivity will be.

## Bibliography Chapter 2

- 
- <sup>1</sup> A. Baldini, R&D proposal to INFN, “The MEG experiment: search for the  $\mu^+ \rightarrow e^+ + \gamma$  decay at PSI”, September 2002.
- <sup>2</sup> M. L. Brooks et al., Phys. Rev. Lett. 83 (1999) 1521.
- <sup>3</sup> W. P. Trower, LBL Report No. UCRL-2426, vol.4 (July 1, 1966) unpublished.
- <sup>4</sup> A. E. Pifer et al., NIM 135 (1976) 39.  
H. W. Reist et al., NIM 153 (1978) 61.
- <sup>5</sup> S. Ritt, Talks from Review Meetings, July 2004, <http://meg.web.psi.ch/docs/>.
- <sup>6</sup> <http://www.sciencedirect.com>.
- <sup>7</sup> A. Hitachi et al., Phys. Rev. B 27 (1983) 5279.
- <sup>8</sup> Handbook of Chemistry and Physics, David R. Lide, Editor-in-Chief, 73rd Edition 1992-1993.
- <sup>9</sup> G. Signorelli, MEG Collaboration, Ph.D. Thesis, “A sensitive search for lepton flavour violation: the MEG experiment and the new LXe calorimetry”.
- <sup>10</sup> S. Dussoni, MEG collaboration, Ph.D. Thesis, “Search for Lepton Flavour Violation: The MEG experiment”, May 2006.
- <sup>11</sup> A. Yamamoto et al., Nucl. Phys. B 78 (1999) 565.
- <sup>12</sup> MEG Collaboration, “Test measurements for the MEG drift chambers” in PSI Annual Report (2003).
- <sup>13</sup> K. Abe et al., MEG-TN012 (2000).
- <sup>14</sup> MEG Collaboration, in PSI Annual Report (2001).
- <sup>15</sup> <http://www.photonis.com/briv/spec/PDF/XP2020UR.PDF>.
- <sup>16</sup> MIDAS home page, <http://midas.psi.ch>.
- <sup>17</sup> PIBETA experiment at PSI, <http://pibeta.psi.ch>.
- <sup>18</sup> P. Dopommier et al., Phys. Rev. Lett. 39 (1977) 1113.
- <sup>19</sup> A. van der Schaaf et al., Nucl. Phys. A 340 (1980) 249.
- <sup>20</sup> W. W. Kinnison et al., Phys. Rev. D 25 (1982) 2846.
- <sup>21</sup> R. D. Bolton et al., Phys. Rev. D 38 (1988) 2077.
- <sup>22</sup> C. Fronsdal and H. Überall, Phys. Rev. 118 (1959) 654.
- <sup>23</sup> S. G. Eckstein and R. H. Pratt, Ann. of Phys. 8 (1959) 297.
- <sup>24</sup> Y. Kuno and Y. Okada, Phys. Rev. Lett. 77 (1996) 434.
- <sup>25</sup> Y. Kuno and Y. Okada, Rev. Mod. Phys. 73 (2001) 151.
- <sup>26</sup> G. J. Feldman and R. D. Cousins, Phys. Rev. D 57 (1998) 3873.

## ***Chapter 3***

In this chapter, the experimental results on the timing counter performance for the MEG experiment<sup>1</sup> will be presented. In particular, the tests performed on a single timing counter bar indicating that the required resolution can be reached, the physical motivation to obtain the best matching between photomultiplier (PMT) and scintillator bar, the geometrical solutions to reduce the magnetic field effects and the best resolution that has been obtained will be described.

### **Timing-counter sub-detector**

The MEG timing-counter (TC) detector consists in two layers of plastic scintillator hodoscopes placed orthogonally: the timing and the triggering sub-detectors, which are designed to measure the positron arrival time and to perform a hardware first level trigger. Figure 3.1 shows the schematic layout of the timing-counter in the COBRA magnet, where both photomultipliers (PMTs) close to the target (inner position) and those far from it (outer position) can be seen. The final design of the scintillators composing each layer will be discussed later. First of all, the parameters affecting the performance of the timing counter will be studied.

When a scintillator is viewed on both ends (a, b) by a PMT, measuring both the pulse-height and the arrival time of the scintillation light to each end ( $T_a$ ,  $T_b$ ), the time difference ( $T_a - T_b = \frac{L - 2z}{v_{eff}}$ ) provides a measurement of the impact point  $z$ , along the scintillator and the mean time ( $\frac{T_a + T_b}{2} = \frac{L}{2v_{eff}} + T_0$ ) gives the absolute impact time  $T_0$ ,

<sup>1</sup> The MEG experiment is a search for a magnetic monopole using the COBRA magnet at the CERN NA62 experiment. The detector consists of two layers of plastic scintillator hodoscopes placed orthogonally: the timing and the triggering sub-detectors, which are designed to measure the positron arrival time and to perform a hardware first level trigger. The final design of the scintillators composing each layer will be discussed later. First of all, the parameters affecting the performance of the timing counter will be studied.

where  $L$  and  $v_{eff}$  are the length and the effective propagation velocity of light in the scintillator bar respectively.

The timing sub-detector should provide the impact time of the positron with a resolution of 100 ps FWHM. This detector should have a cylinder shaped structure in order to be placed inside the COBRA magnet bore. Further it should be made of identical plastic scintillator slabs aligned with the direction of the COBRA axis, covering  $157.5^\circ$  in  $\phi$  and  $27.6 \text{ cm} < |z| < 108.0 \text{ cm}$ . The main parameters that have been evaluated and optimized in the design and test of prototypes are:

1. scintillation rise and decay time, attenuation length;
2. PMT's transit time spread (TTS), quantum efficiency (QE), gain;
3. particle trajectory length and its spread;
4. signal slew rate, bandwidth and noise.

The parameters that have the highest impact on the design of the timing counter are 1, 2 and 3. It should be noted that the intrinsic TTS, the QE and the gain are strongly constrained by the characteristics of the few available PMTs that can operate in a high magnetic field ( $B$ ) environment.

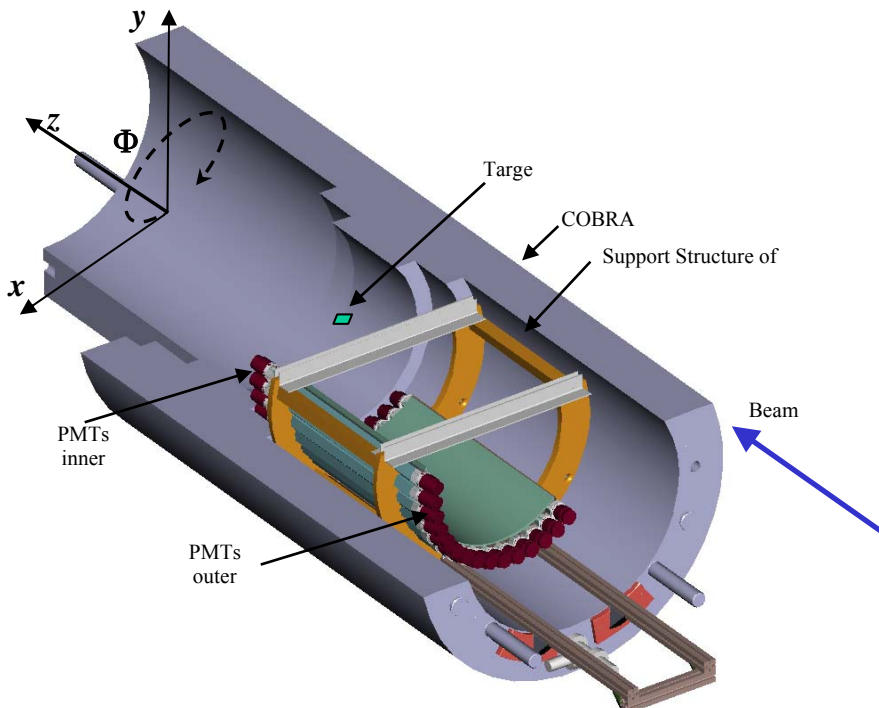


**Figure 3.1:** Schematic view of one of the two timing counters (up-stream), inside the COBRA magnet.

### 3.1. PMTs characterization in magnetic field

The PMTs parameters in magnetic field have been measured, for the first time, at the INFN-LASA/Milano facilities. Fine-mesh PMTs, produced by Hamamatsu, can operate at high gain and reasonable low sensitivity to the magnetic field, thanks to the principle of electron multiplication based on flat fine-mesh grids acting as dynodes. A sketch of a fine-mesh PMT with its working principle is shown in Figure 3.2. This tube is constructed with an input window, a photocathode, fine-mesh dynodes and an anode.

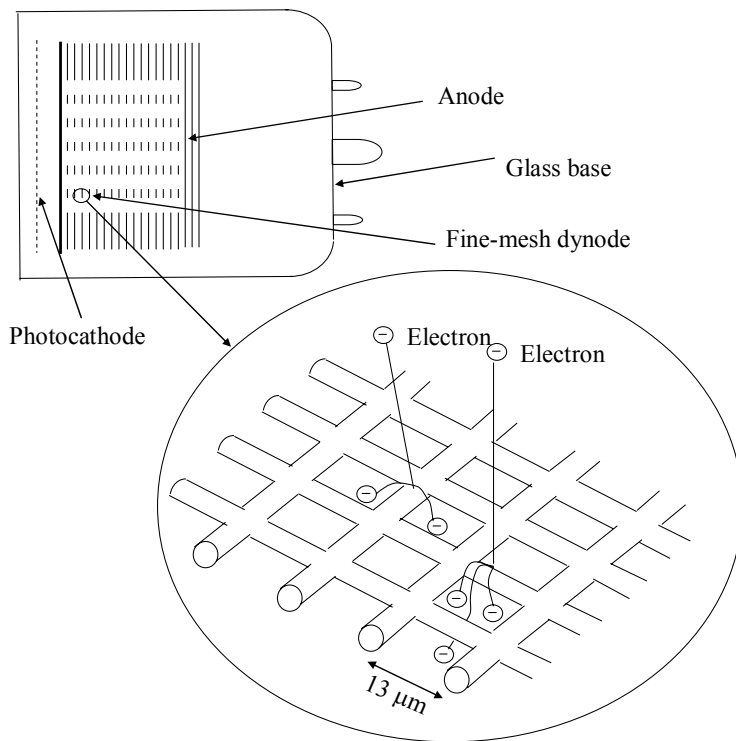


**Figure 3.2:** Sketch of a fine-mesh PMT by Hamamatsu.

When an electron impinges on the upper part of the mesh, multiple secondary electrons are emitted from the secondary emissive surface deposited on the mesh. This process is repeated through the last dynode stage and finally electrons are multiplied up to a million times. Although the output decreases with increasing magnetic flux, this tube can be used up to near 1.5 Tesla. This performance is due to the fine-mesh structure with its very minute diameter and also to the close-proximity spacing between dynodes, so that the electron trajectories of the secondary electrons emitted from the fine-mesh dynodes are resistant to external magnetic fields.

While these devices can drive very high single pulse current without loosing peak voltage linearity, up to 35 V on a  $50\ \Omega$  load with a linearity reduction of 5% for 2" diameter PMTs (see Table 3.1), a limit on the integrated anodic current must not be exceeded, to avoid dynode damage and pulse amplitude reduction (loss of linearity). This parameter can be simply investigated by observing the anode output amplitude pulse as a function of the pulse rate. Hence, the rate at which the amplitude starts to decrease, multiplied by the pulse duration and by the pulse current (voltage amplitude divided by  $50\ \Omega$ ) gives the average limit current before losing linearity. This limit is typically  $100\ \mu\text{A}$  for 2" diameter PMTs. Moreover there is an other parameter that represents the total charge which can be accumulated by a PMT, i.e.  $100\mu\text{A} \times 100\text{h} = 36\text{C}$  for 2" diameter PMT. Systematic studies have been done for 1" diameter (R5505), 1.5" diameter (R7761) and 2" diameter (R5924) Hamamatsu fine-mesh PMTs, as resumed in Table 3.1, using a refurbished resistive dipole magnet at LASA facilities, with magnetic fields up to 1.2 T and an open gap of 12 cm.

**Table 3.1:** Main properties of Hamamatsu fine-mesh PMTs.

Properties	R 5505	R 7761	R 5924
Tube diameter	1"	1.5"	2"
No. stages	15	19	19
Q.E. at peak (390 nm)	23%	23%	22%
Gain (B=0T)	$5 \times 10^5$	$1.0 \times 10^7$	$1.0 \times 10^7$
Gain (B=1T)	$1.8 \times 10^4$	$1.5 \times 10^5$	$2.5 \times 10^5$
Rise time (ns)	1.5	2.1	2.5
TTS (ns)	0.35	0.35	0.44
Average anode current $I_a$ (mA)	0.010	0.010	0.100
Max pulse amplitude to get a 2% linearity (mA)	180	350	500
Max pulse amplitude to get a 5% linearity (mA)	250	500	700

The PMTs were inserted in the central region of the test magnet, where the field had a uniformity of  $\sim 1\%$ , using plexiglass supports providing up to  $60^\circ$  inclination with respect to the magnetic field lines. Measurements were performed to evaluate the gain reduction, timing resolution and rate capability as a function of magnetic field and relative orientation angles ( $\theta$ ). Due to the effect of magnetic field on the accelerated electrons inside the PMTs, a reduction of gain as the  $B$  increases was expected and also a marked dependence of the relative gain on the  $\theta^{[2]}$ . Fine-mesh PMTs show a good behaviour up to a critical orientation,  $\theta_c$ , depending on the photocathode size: typically  $\theta_c \sim 30^\circ$ . In Figure 3.3 the behaviour of a 2" PMT gain, with a standard HV value of +2000 V, as function of magnetic field, for different orientation angles with respect to the B is shown.

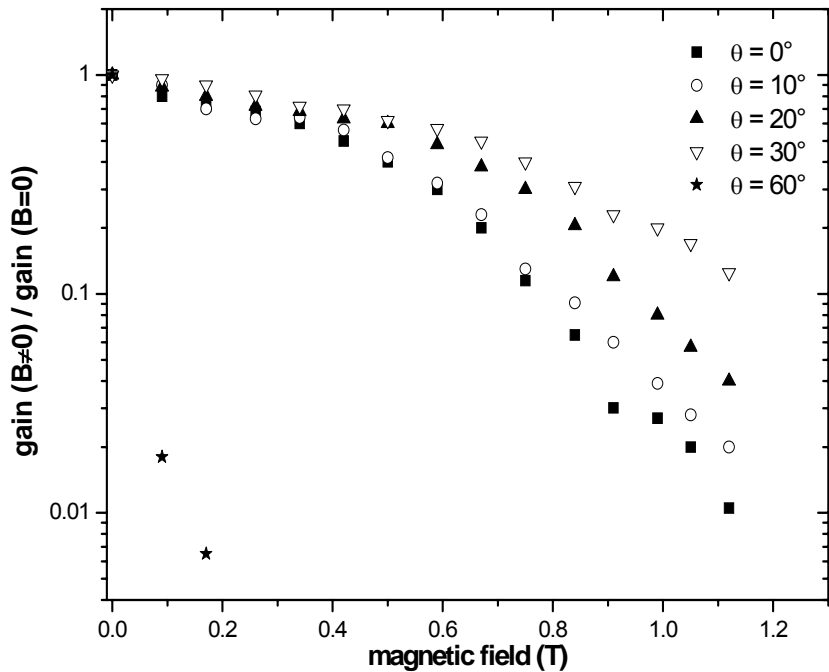


**Figure 3.3:** Behaviour of PMT gain in magnetic field for a typical 2" Hamamatsu R5924 fine-mesh PMT, at various inclinations angles. In ordinate the gain ratio for B and B=0 T is plotted.

The results are in agreement with the producer data sheet<sup>2</sup>, for a uniform magnetic field. Figure 3.3 shows that, when the magnetic field is on, the gain is always lower than 1; for an angle of  $60^\circ$ , the gain dramatically decreases with a reduction factor  $\geq 100$  for a field of 0.17 T.

The timing characteristics of fine-mesh PMTs show a weak dependence on field strength and direction, as shown in Figure 3.4, in spite of the large reduction in gain

(about a factor 100). Only at high fields,  $\geq 1\text{T}$ , the timing resolution in the standard position ( $\theta = 0^\circ$ ) is affected of an evident decrease, as shown in Figure 3.5 for a typical 2" fine-mesh PMT.

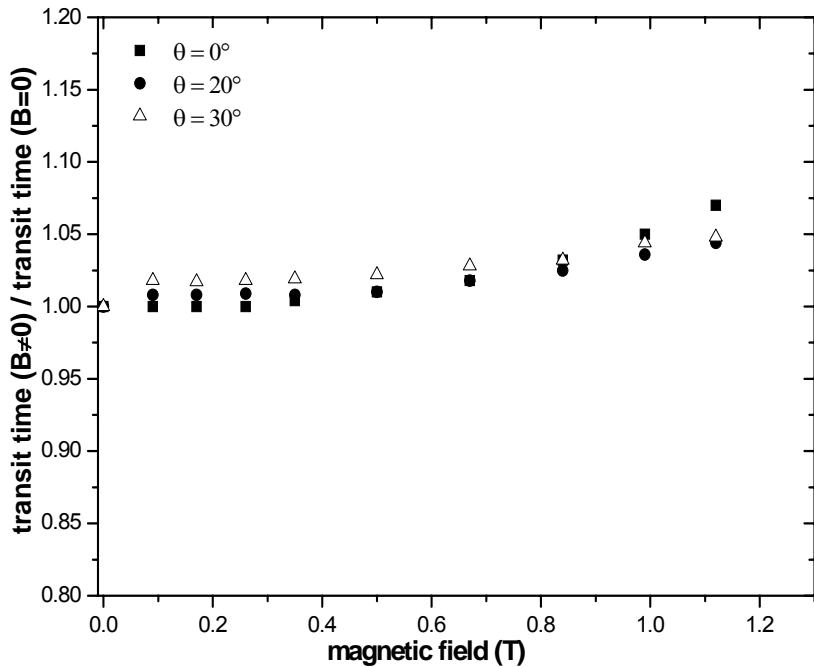


**Figure 3.4:** Transit time ratio, for magnetic field  $B$  and  $B=0\text{ T}$ , as a function of magnetic field for a typical 2" Hamamatsu R5924 fine-mesh PMT.

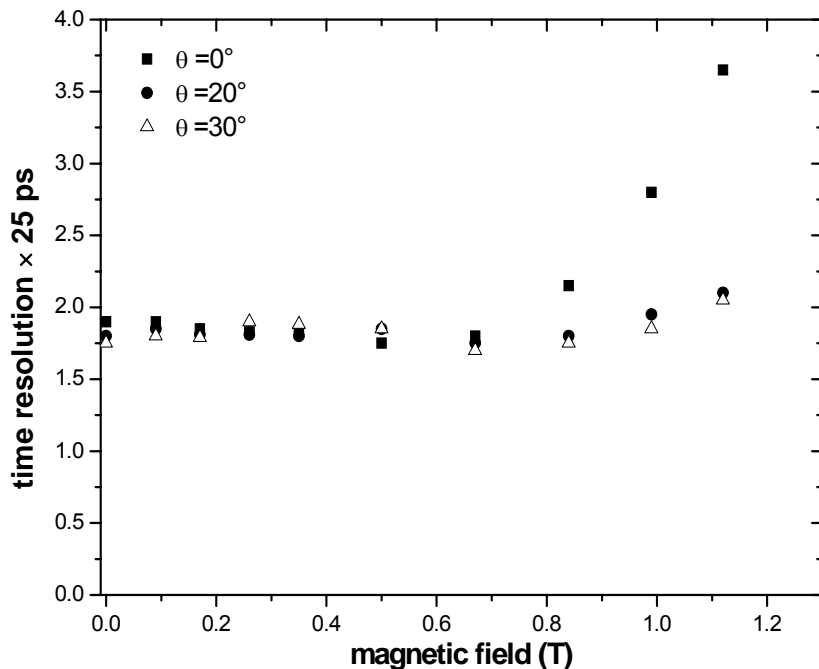


**Figure 3.5:** Timing resolution in 25 ps units as a function of the magnetic field for a typical 2" Hamamatsu R5924 fine-mesh PMT.

The rate capability, i.e. the frequency dependence of the gain, of fine-mesh PMTs is limited by the maximum allowable average anode current  $I_a$ , as per Table 3.1. During the test at LASA, the peak amplitude  $V_{out}$  (proportional to the gain) was measured as a function of the laser pulse repetition rate, for typical 1", 1.5" and 2" diameter fine-mesh PMTs, in different magnetic field conditions with a standard HV value of +2000 V. The best performances have been obtained with 2" photomultiplier as can be concluded from data in Figure 3.6.

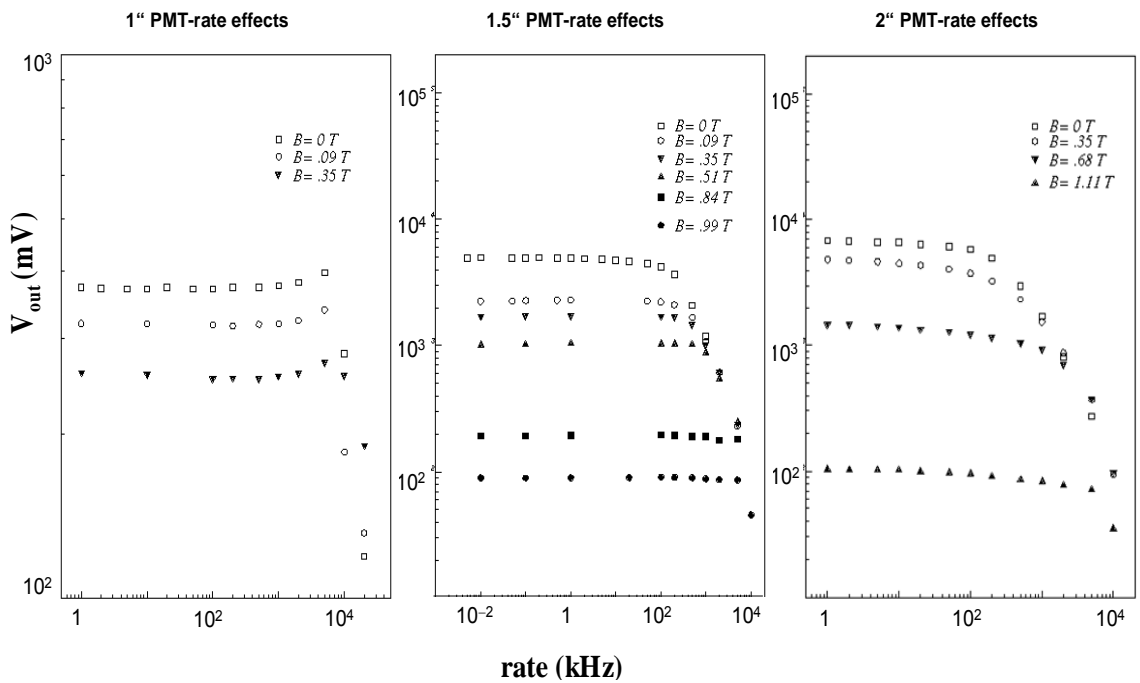


**Figure 3.6:** Rate capability of typical 1", 1.5" and 2", at  $\theta = 0^\circ$ , fine-mesh PMTs, as a function of magnetic field<sup>3</sup>.

Figure 3.6 shows that, at zero field,  $V_{out}$  of 1" PMT never exceeds 0.4 V, while 1.5 and 2" PMTs reach, in the same conditions, voltage values of the order of 5 and 7 V respectively. In the presence of a magnetic field, this effect is even more evident: at 0.35 T,  $V_{out}$  of 1" phototube is less than 0.26 V, while 1.5" and 2" PMTs show maximum  $V_{out}$  of 1.9 and 4.9 V with reduction factors of about 35, 62 and 30% respectively.

These preliminary tests showed that a maximum of the gain, in a magnetic field, is obtained tilting the PMTs in order to reach an angle  $\sim 30^\circ$  with respect to the field direction, as concluded from Figure 3.3. Consequently, a tilting angle respect to the field lines has been inserted in the timing counter design, in order to maximize the gain.

The final design of the tilted PMT is schematically shown in Figure 3.7. Unfortunately the tilting angle cannot reach  $30^\circ$ , because of geometrical constrains on maximum allowable radius inside COBRA, minimum radius settled by positron acceptance function and interaction with the Drift Chamber detectors. The total angle is given by the sum of the geometric angle and the angle that the magnetic field lines form with the COBRA z axis, which is  $\sim 10^\circ$  at 25 cm from the vertex (inner position) and  $\sim 8.5^\circ$  at 105 cm (outer position)<sup>4</sup>.

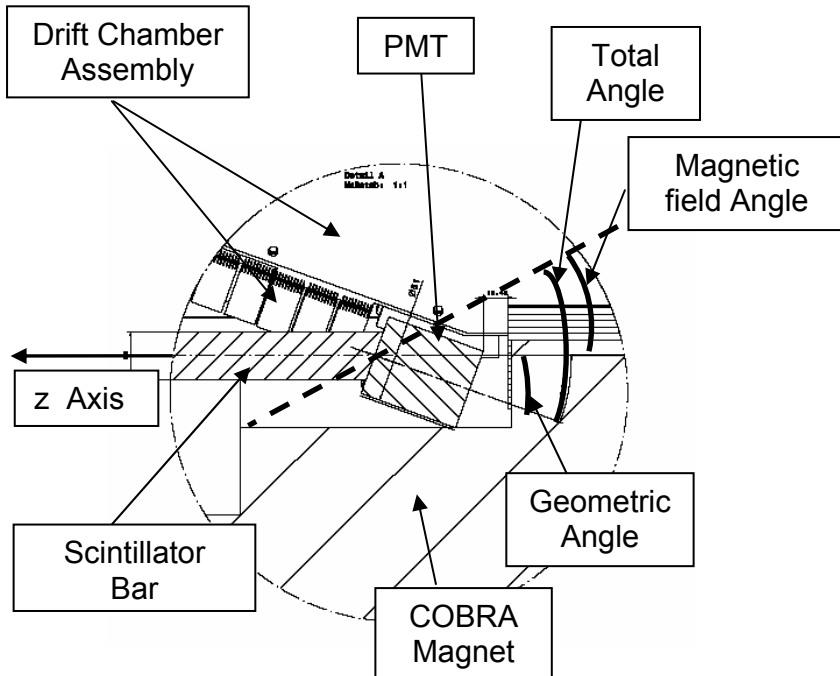


**Figure 3.7:** Sketch of the final position and orientation of the internal PMT inside the COBRA magnet.

Furthermore, it can be concluded that the 2" diameter PMTs were best fitted to our requests of gain, rate capability, maximum peak current and average anode current. Moreover, as it will be shown in the following, these PMTs allow to obtain the best matching between PMT and scintillator bar also improving the time resolution.

### **3.2. Test of the tilted PMT solution in the COBRA magnet**

The proposed solution for the tilted PMTs has been tested inside the COBRA magnet in April-May 2004. This measurement has been done to verify the effect of the real field, whose non-uniformity cannot be reproduced in the LASA magnet. During these tests, 2" diameter PMTs have been used, due to larger average anode current.

The PMTs have been mounted in the final operating position by using a frame that allowed the rotation around an axis perpendicular to the field lines and parallel to the photocathode plane, i.e. rotations in the z axis plane are allowed, maintaining the photocathode centre at a fixed radius predicted for the TC bars. The gain and the TTS, have been measured by illuminating the photocathode uniformly with a pulsed laser beam with  $\lambda=405$  nm, 60 ps pulse width and maximum rate of 100 MHz (Hamamatsu mod.PLP-10). The PMT intrinsic TTS is the main limit to the time resolution. The TTS is a difficult parameter to be measured at the single photoelectron regime, because of the wide exponential shape of the single photoelectron spectrum of these PMTs types. This is caused by the large spread in gain of the fine-mesh electron multiplier of the tube.

The importance of these tests lies in the possibility to measure the operative performance of the PMTs inside the COBRA magnet, in which the field is not uniform, and the electromagnetic interference noise is high. The gain was measured as a function of pulse repetition rate at different angles of four 2" fine-mesh PMTs; the timing resolution at different number of photoelectrons per pulse and at different angles. All the measurements have been taken in both positions inside the COBRA magnet (inner and outer). The data are affected by a systematic error of 5% in the orientation reproducibility and about 10% in absolute photoelectron number. Figure 3.8 shows the behaviour of a PMT (R0415) inside the COBRA (inner position) with a total angle of  $27.5^\circ$ . The constant voltage behaviour, in the curves, undergoes a slope variation caused by the saturation in the anodic current. The decrease of the output voltage, proportional to the gain, performance in the COBRA magnet ( $B= 1.05$ T) can be recovered by increasing the bias voltage supply of the PMT. The characteristics of the PMTs used

inside the COBRA, are summarized in Table 3.2\*: the cathode luminous sensitivity is the photoelectric current from the photocathode per incident light flux from a tungsten filament lamp operated at a distribution temperature of 2856 K and the anode luminous sensitivity is the anode output current, amplified by the secondary emission processes, per incident light on the photocathode. The cathode blue sensitivity index is the photoelectric current from the photocathode produced in the same way as previously described, but passing through a blue filter, with a peak at 420 nm. Finally, the anode dark current is the amount of current flowing in a photomultiplier tube even when the tube operates in a completely dark state.

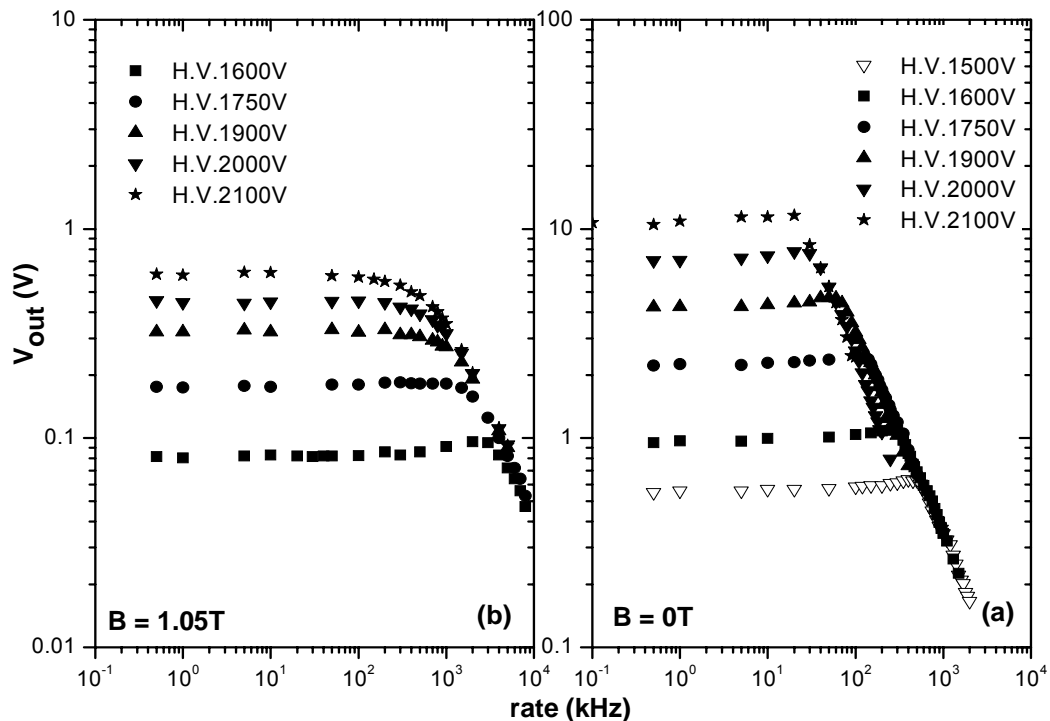


**Figure 3.8:** Output voltage versus pulse repetition rate at zero field (a) and in the inner COBRA field position (b).

---

\* The source of the datasheets of these phototubes is Hamamatsu; and are peculiar to these detectors.

**Table 3.2:** Physical and electrical characteristics of the R5924 Hamamatsu photomultiplier.

Properties	RA0415	RA0431	RA0432	RA0434
Cathode Luminous Sensibility	103.0 $\mu\text{A/lm}$	65.6 $\mu\text{A/lm}$	59.8 $\mu\text{A/lm}$	86.4 $\mu\text{A/lm}$
Anode Luminous Sensibility	1010.0 $\text{A/lm}$	1130.0 $\text{A/lm}$	2420.0 $\text{A/lm}$	1920.0 $\text{A/lm}$
Anode dark current	30.00 nA	0.60 nA	1.80 nA	1.70 nA
Cathode Blue Sensibility Index	10.70	9.35	8.52	10.10
QE% at 405 nm (extrapolated)	28.2 %	24.6 %	22.4 %	26.6 %
Gain at 1500 V	$6.3 \times 10^6$	$1.3 \times 10^6$	$3.3 \times 10^6$	$2.0 \times 10^6$
Gain at 1750 V	$20.3 \times 10^6$	$5.3 \times 10^6$	$12.0 \times 10^6$	$7.0 \times 10^6$
Gain at 2000 V	$100.0 \times 10^6$	$17.0 \times 10^6$	$40.0 \times 10^6$	$22.0 \times 10^6$
Gain at 2250V	$430.0 \times 10^6$	$53.0 \times 10^6$	$115.0 \times 10^6$	$70.0 \times 10^6$

Figure 3.9 shows the output voltage as a function of bias voltage of PMT, at different geometric angles in the COBRA, indicating that for a voltage of 2100 V (B on) it is possible to recover the gain corresponding to a voltage of 1500 V (B off), for geometric angles between 10 to 20 degrees. In Figure 3.9, “zero-field” and “zero-field-1” represent two measurements with B off, obtained after 7 hours from the shutdown of the COBRA. In particular, the second one has been done to verify the reproducibility of the measurements. In Figure 3.10, the TTS results of the final configuration in inner and outer position as a function of the tilting angles and photoelectrons pulses is shown. These time resolution measurements following photon statistics confirm that the timing obeys a  $\frac{1}{\sqrt{N_{pe}}}$  law.

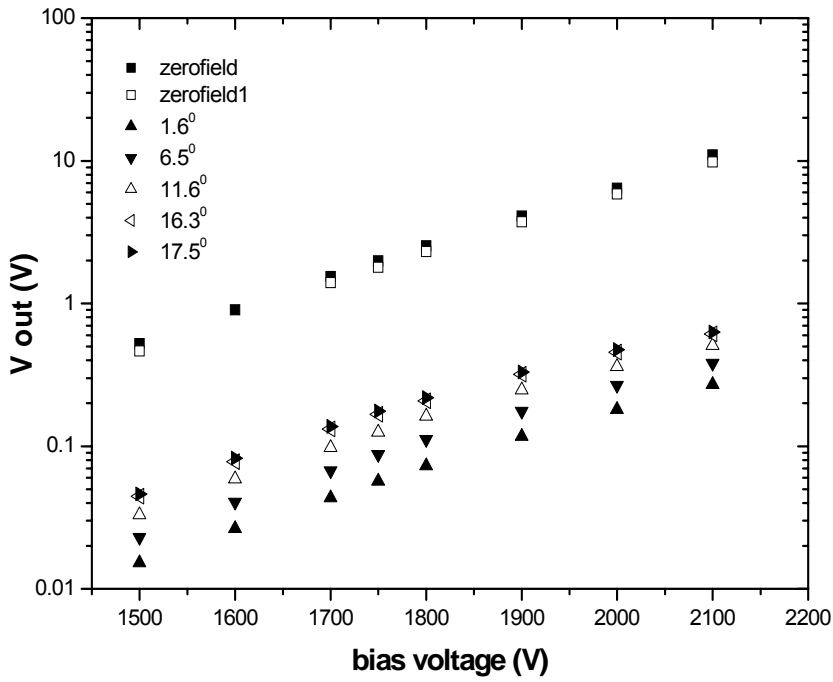


**Figure 3.9:** Output voltage versus bias voltage for inner PMT as a function of different geometric angles.

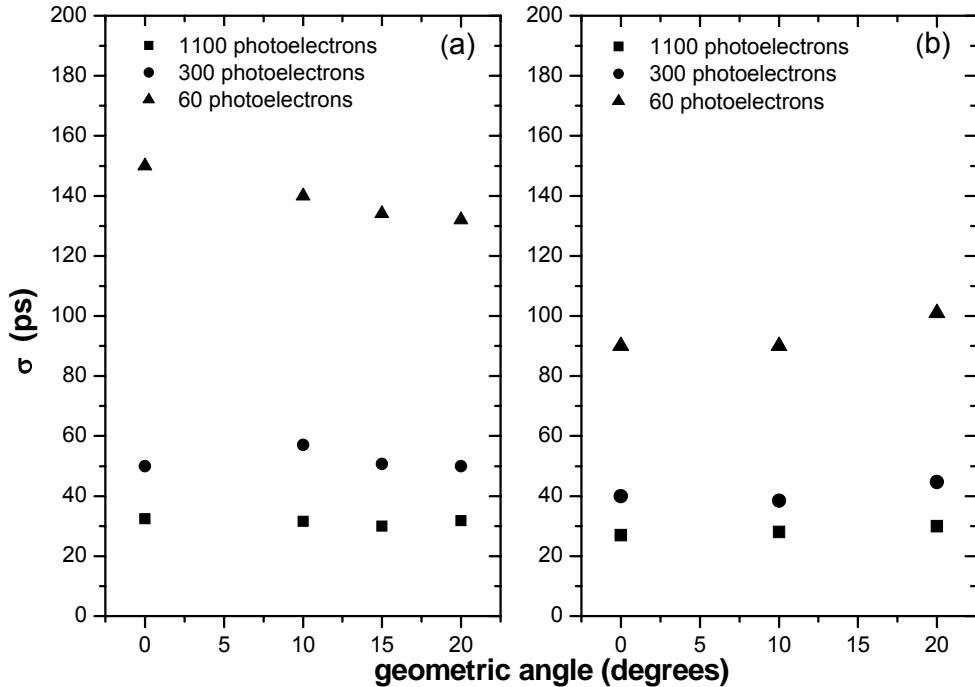


**Figure 3.10:** TTS for a inner (a) and outer (b) PMT, as a function of the geometrical tilting angles for 60, 300 and 1100 photoelectrons pulses.

The first conclusion of the test in the COBRA magnet is that the decrease of the time resolution overall performance, can be fully recovered by increasing the bias

voltage supply to the PMTs. This means that the gain loss, which is responsible for lower amplitude and lower slew rate ( $\frac{dV_{out}}{dt}|_{Max}$ ), can be fully recovered. The needed increase of biasing voltage is limited to reasonable values (i.e. 2100 V) thanks to the choice of the best tilted position. The second conclusion is that a number of photoelectrons between several hundreds and one thousand should be needed in order to work in the 100 ps resolution range.

### 3.3. Time resolution measurements at the beam

The measurement of the overall time resolution of a single element of the counter can be done ideally with a particle beam hitting the plastic scintillator in order to simulate the final trajectory of a positron inside scintillator itself.

For a particle beam, the rms spread of the variable  $t = t_a - t_b$  of a scintillator detectors, is given by<sup>5</sup>:

$$\sigma_t = \sqrt{\sigma_{elec}^2 + \frac{\sigma_{scin}^2 + \sigma_{pmt}^2 + \sigma_{pl}^2}{N_{pe}}} , \quad (3.1)$$

where  $\sigma_{scin}$  represents the rms value of the photon emission distribution function,  $\sigma_{pl}$  is the time spread in the light collection due to path length variations,  $\sigma_{pmt}$  is the time jitter in the photomultiplier and  $\sigma_{elec}$  is the jitter in the electronics readout system. The dominating factors for  $\sigma_t$  are  $N_{pe}$ , the number of photoelectrons; below 100 ps, contributions such as  $\sigma_{pmt}$  become increasingly important. By analyzing all the parameters determining the time resolution the following items can be observed.

1.  $\sigma_{pl}$  can be thought as formed by two terms: the first one,  $\sigma_{pla}$ , is the geometric spread of the beam which gives uncertainty on the impact point position. In our case, the beam spread has an uncertainty limit of 5 mm due to the size of the scintillator placed between the beam and the bar under test; it acts also as a collimator for the beam. The contribution of  $\sigma_{pla}$  is therefore  $\frac{\sigma_x}{v_{eff}} \approx \frac{2 \cdot 10^{-3}}{1.37 \cdot 10^8} \approx 15 \text{ ps FWHM}$ . It should be noted that the rms spread of the

variable  $t=(t_a+t_b)/2$ , (the measurement of the time resolution), is not influenced by this term because the mean time  $\frac{T_a+T_b}{2} = \frac{L}{2v_{eff}} + T_0$ , that gives the absolute impact time  $T_0$ , does not depend on the position. However, due to practical considerations, the most sensitive way for measuring the timing resolution, is via the time difference by a Time to Amplitude Converter (TAC). The second term,  $\sigma_{plB}$ , represents the spread due to the different paths of the light inside the bar.

2.  $\sigma_{scin}$  mainly arises from three contributions. The first and the most important term is related to the time spread owed to the generation of photons inside the scintillator. Figure 3.11 shows the photon arrival times on the two opposite PMTs. The simulation has been made considering 54000 photons generated in random positions perpendicularly to the phototube, according to the time distribution ( $TD$ ) given by  $TD = A(e^{-t/\tau_1} - e^{-t/\tau_2})$ . In this expression,  $A$  is a constant related to the number of photons created,  $\tau_1 = 1.8$  ns is the decay time of the scintillator and  $\tau_2$  is taken so that the rise time of the signal generation is exactly 0.7 ns, characteristic time of this scintillator as found on producer data sheet. The randomly and uniformly generated photons can take both directions indistinctly and this is confirmed by Figure 3.11, where the distributions of the two phototubes are identical. The number of generated photons,  $Nph$ , can be obtained taking into account that the light output is proportional to that produced by anthracene (68%, see Table 3.3), while the energy needed to produce a photon is  $\sim 100$  eV<sup>[1]</sup>. In this way, considering that in plastic scintillators, the released energy is about 2 MeV per crossed cm<sup>[6]</sup>, we have a number of produced photons given by:  $Nph = \frac{2MeV}{cm} \cdot 4cm \cdot \frac{1}{100eV} \cdot 68\% = 54400$  in

agreement with the measured values. The second contribution is the spread caused by the propagation of light inside the plastic scintillator that acts as a wave-guide. Finally, the last term is due to the fact that the photons are generated along the whole track of the positron going through the scintillator and not in a single point. In this case, the average incidence angle of the particle is  $\sim 38^\circ$ , as shown by the MC simulation (see Figure 3.13) and therefore the time spread is related to the projection of the track along the scintillator axis. Without

going through a detailed description, it can be concluded that the contribution due to this term is at least three times smaller than the formation time of the light inside the scintillator. In fact, considering a track,  $w$ , of  $\sim 5$  cm the time spread is

$$\approx \frac{wsen\theta_{inc}}{v_{eff}} \approx 200 \text{ ps} , \text{ whereas the light formation time is } 700 \text{ ps.}$$

3.  $\sigma_{elec}$  has been measured during the tests at LNF and its contribution has been estimated to be  $\sim 38$  ps FWHM. Obviously, this value is just an indication for the tests carried out during the construction of the detector, and thus using the available electronics. The real value will be estimated only when the definitive electronics will be available.
4. As already recalled in paragraph 3.2,  $\sigma_{pmt}$  is the TTS of PMTs. The experimental value obtained during the tests,  $\sim 650$  ps FWHM, is larger than the one indicated by the manufacturer.

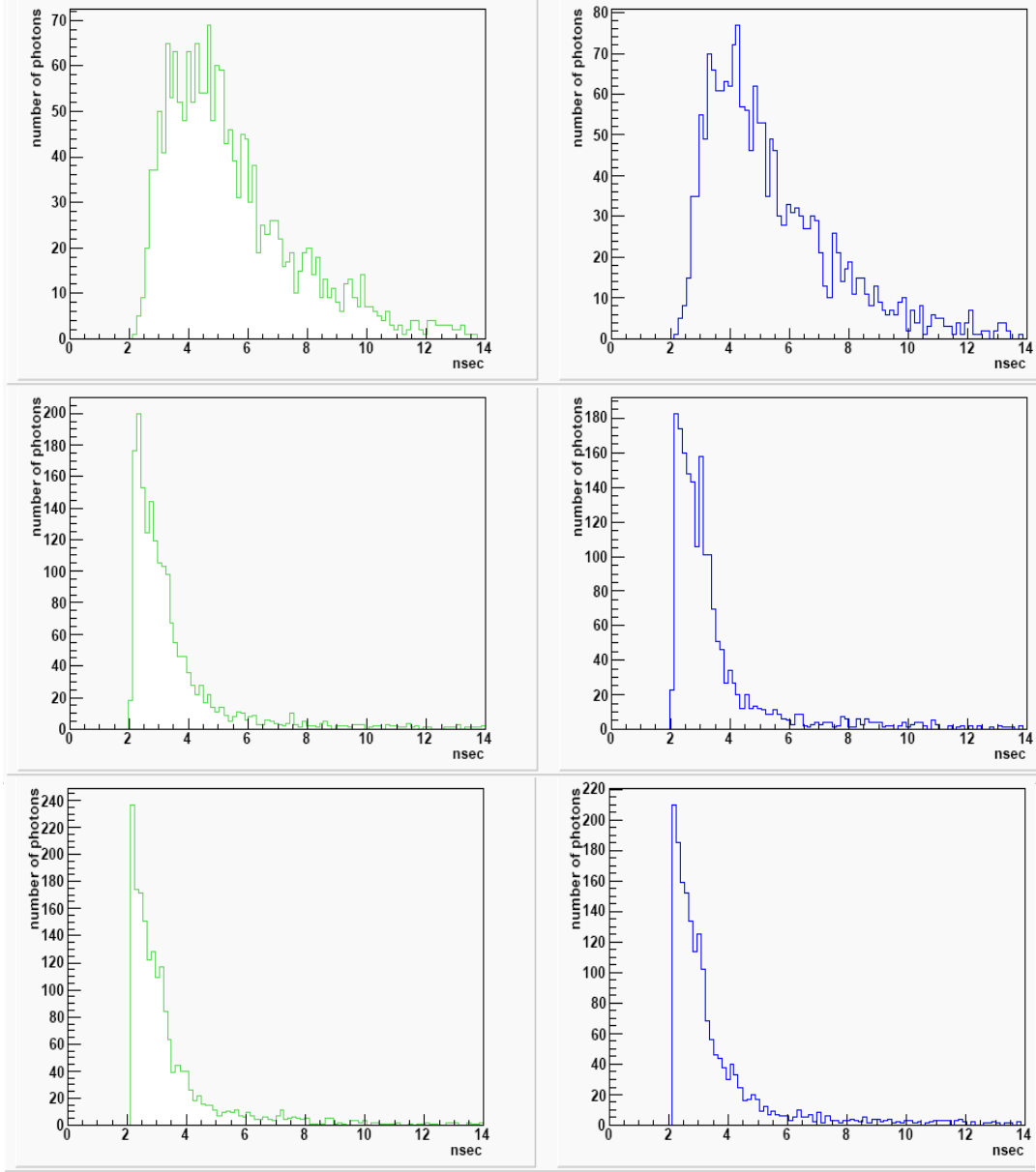


**Figure 3.11:** Photon arrival times on PMTs taking into account: time and spatial spread (top), spatial spread only (middle) and neglecting both (bottom).

From Figure 3.11 it can be noted that the main contribution to the time resolution is due to the time spread caused by the light pulse generation inside the scintillator, which gives  $\sim 1.98$  ns FWHM. This value has been obtained by subtracting from the resolution of the first distribution (Figure 3.11, top) those of the second or third one (middle and bottom panels), which do not show appreciable differences.

### 3.3.1. Early test

A prototype of a single counter slab has been preliminary tested at the  $\pi E1$  and  $\pi E5$  beam-lines at PSI and then at the Beam Test Facility (BTF) at National Laboratory of Frascati (LNF), (December 2003-January 2004). The prototype was made by a plastic scintillator 50 mm wide, 20 mm thick and 800 mm long, which has been coupled to the PMTs with and without light guide. The measurements were made without magnetic field. The best time resolution ( $104 \pm 2$ ) ps FWHM<sup>[7]</sup>, which fully meets the requirements of the TC, was obtained, for the first time, at BTF. The BTF provides  $e^-/e^+$  beams in the energy range of 25-750 MeV. The intensities available can range from a single particle per bunch with a pulse length of 1-10 ns, up to  $10^{10}$  particles per pulse, with a cycling rate of 50 Hz. In our standard measurements, the average number of electrons per bunch was in the range 0.5-1.5. However, the duty cycle at the present is limited to about 50%: particles are not available to the BTF when DAFNE is filled, which usually happens every 20 minutes, for a time interval of 20 minutes.

These measurements clearly confirmed that the timing resolution is mainly limited by the photoelectron statistics. Indeed, the time resolution is, in a first approximation, proportional to the inverse of the square root of the path length of the positrons inside the plastic scintillators. The timing resolutions have been measured for path length of 20 and 50 mm respectively, with 1.5" and 2" diameter fine-mesh PMTs. In Figure 3.12, the triangles represent the resolutions obtained with 1.5" PMT and scintillator bar BC408<sup>[8]</sup>, whereas circles and squares are the measurements made with two 2" PMTs. The superimposed curves show the  $\frac{1}{\sqrt{(path-length)}}$  behaviour. The two measurements with 2" PMT have been made with different plastic scintillators: BC408 and BC404 respectively. These scintillators are both provided by Saint-Gobain Crystal<sup>8</sup>. The plastic scintillator BC404 is slightly better than BC408 for fast time applications. However, the data did not show a large difference between the two types of bars, and further experiments are needed.

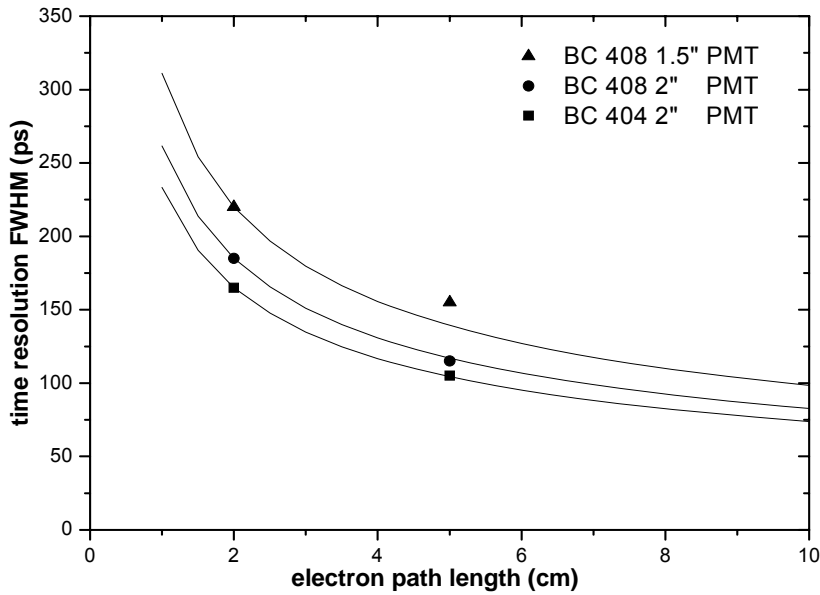


**Figure 3.12:** Best timing resolution as a function of path-length for 1.5" and 2" diameter PMTs. The curves show the  $1/\sqrt{\text{path-length}}$  behaviour.

The electronic setup for timing measurements has been tuned in order to reduce the time-walk effect to a negligible value. Moreover, to better define the size of the beam and to reduce the number of background events, a system for the geometrical selection of the beam has been realized; it consists of a  $5 \times 5 \text{ mm}^2$  cross made by two scintillating fibers coupled to avalanche photodiodes (APD). In this way, the signal coincidence from APDs and from the accelerator trigger allowed a good rejection of background events. Furthermore, the time spread due to the uncertainty on the impact position of positrons in the scintillator is reduced.

Each TC element consists of a scintillator bar with a PMT at each end, defined as PM1 and PM2. The time arrival of the scintillation light at both ends, produced at the particle's impact point at the bar, is given by  $T = (T_1 + T_2)/2$ , where  $T_1$  and  $T_2$  correspond to PM1 and PM2, respectively. The statistical uncertainty on the quantity  $T$  is the same as for  $T' = (T_1 - T_2)/2$ , easily measurable by employing a conventional start-stop technique. In this configuration, the PM1 signal provides the START signal to a Time to Amplitude Converter stopped afterwards by the PM2 signal, where is included a time delay to insure  $T_2 > T_1$ . After the STOP signal, the resulting analogue voltage is sampled and converted to a digital signal (ADC), which is proportional to the time between the two events. The timing resolution is given by the maximum time interval divided by the ADC resolution and equal to 28.0 ps/digit. Significant time fluctuations

were observed when employing a fixed threshold discriminator, due to the so called time-walk effect caused by a large variation of PMT's pulse-height.

A double-threshold technique was used, where a low-threshold discriminator at level of single photoelectron amplitude and sensitive to the early arriving photons, introduces negligible time-walking fluctuations and a high-threshold is used uniquely to validate the low-threshold signal, thus suppressing events produced by dark noise.

### 3.3.2. Choice of scintillator and PMT

Usually the area of the photocathode is small compared to the cross-sectional area of the scintillator<sup>[9,10,11]</sup>. Light will be lost in making this transition, but it is important that these losses are minimized and uniform over the cross-section of the scintillator, and that the transit time from all points at the scintillator end to the photocathode are approximately equal. For this reason and to increase the number of photoelectrons, the dimensions of scintillator bars were modified. The plastic scintillator bars composing each TC element had the following dimensions  $40 \times 40 \times 804$  mm<sup>3</sup>, thickness, width and length, respectively. At each end of the bar is directly coupled a 2" diameter Hamamatsu fine-mesh PMT (R5924). Its diameter is 52 mm and its photocathode diameter is 39 mm, thus optimally fitting the bar cross-section and eliminating the need of a light guide, which would increase the scintillation light time spread. The effective coupling efficiency is ~74%. Two types of scintillator materials have been studied: BC404 and BC408. The main characteristics are resumed in Table 3.3.

**Table 3.3:** Main properties of scintillator bars.

Scintillation Properties	BC404	BC408
Light output (% anthracene)	68	64
Rise time (ns)	0.7	0.9
Decay time (ns)	1.8	2.1
Wavelength of max. emission (nm)	408	425
Light attenuation length (cm)	140	210

The bars have been prepared in Genova according to the final design as illustrated in Figure 3.13. This figure shows that to avoid a timing counter-drift chamber contact it was necessary to reduce the tilting angle from 20 to 11° (geometric angle as reported in Figure 3.7) and to cut 5.3 mm of the scintillator edge.

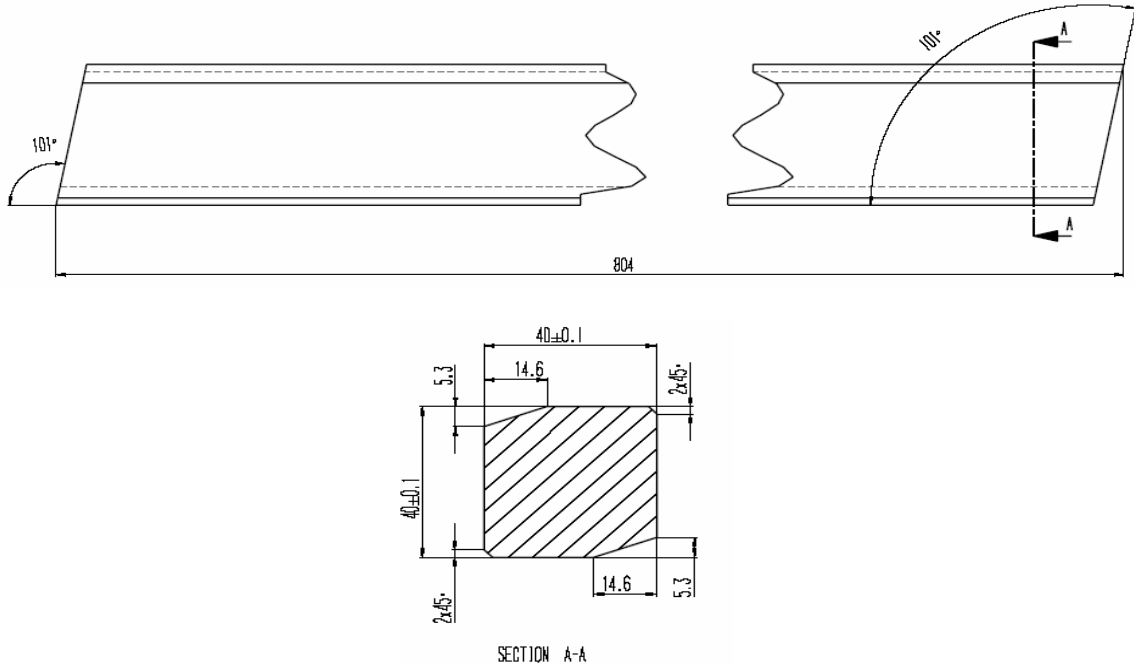


**Figure 3.13:** Final design of scintillator bar, side view (top) and front view (bottom).

The time resolution studies of the scintillator bars were performed in the Frascati Beam Test Facility in November 2004 and measured for several beam impact positions, along the bar (z-direction), and different impact angles, with respect to the normal of the bar surface. The impact angle and position cover a range corresponding to the most probable angles and positions given by a Monte Carlo simulation of the positron trajectories in the experiment, as illustrated in Figure 3.14.

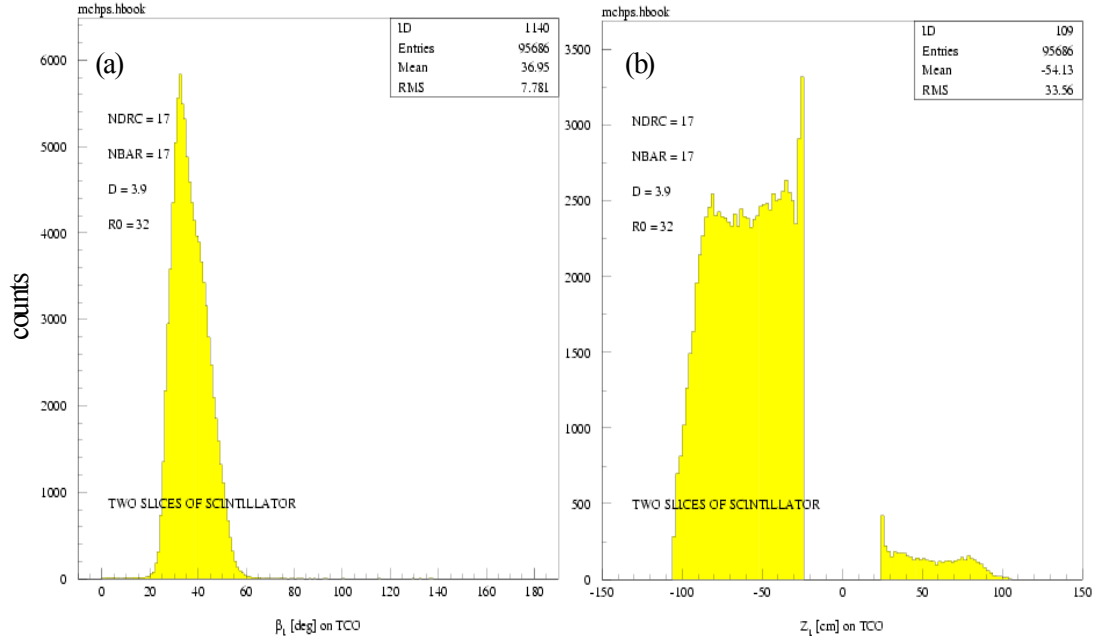


**Figure 3.14:** Monte Carlo simulations on the count rate response as a function of: the  $e^+$  impact angle (a) and the  $e^+$  impact position (b)<sup>12</sup>.

$R_o$  [cm] corresponds to the vertical distance between the bar and the target; D [cm] is the dimension of the square bar;  $N_{DRC}$  and  $N_{BAR}$  are the number of drift chambers and bars, respectively; in the horizontal axis labels, TCO refers to outer TC. Accordingly to this figure, the highest count rate corresponds to an impact angle of  $\sim 37$  degrees and to an impact position of  $\sim 54$  cm. The Monte Carlo simulation generates positrons in the range of  $-0.35 < \cos\theta < 0$ . Figure 3.14 (b) shows a tail for  $z>0$  due to a positrons generation near  $\cos\theta = 0$ . When the angle is close to  $90^\circ$  in fact, it is possible that a positron undergoing a multiple scattering produces a positive momentum component.

Due to the relatively large number of positions and angles in which measurements had to be carried on, a special mechanical chariot was built in the University of Genova, where the mounted bar is moved by remote control. The bar can slide along the chariot's main axis so that all points along the bar can be brought to the beam spot with a precision better than 5 mm. The chariot's axis can rotate around a horizontal axis and the bar can also rotate around the chariot axis. The precision for both rotations is 0.5 degrees. Figure 3.15 shows the chariot standing at an inclination of about 45°.



**Figure 3.15:** The mechanical chariot standing at the BTF, in Frascati.

The conditions chosen for the tests at the BTF were:  $e^+$  particles with energy of 420 MeV, yielding a minimum beam spot size; one particle per pulse in average, reducing the multi-hits events in the 10 ns spill. The bar under test is sandwiched between two BC422<sup>[8]</sup> scintillators, S1 and S2. S1 is a slab of 23x12x5 mm<sup>3</sup> coupled by a single 1" PMT (Hamamatsu R 647-01), and S2 is a slab of 50x50x20 mm<sup>3</sup>, measured by two PMTs (Philips XP2020). The general test layout is sketched in Figure 3.16.

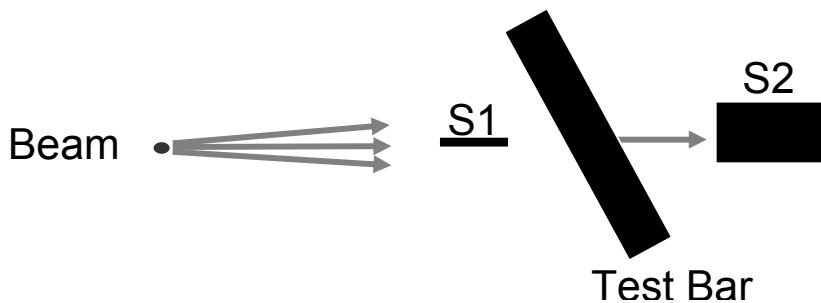


**Figure 3.16:** Layout of the tests at the BTF of Frascati.

The purpose of using S1 is to determine the vertical impact position optimizing the beam line parameters, which could introduce an “apparent” time spread in the test bar. The respective mean sizes, obtained from Gaussian fit are 3.0 and 2.1 mm,

indicating that the spot size is well defined, not introducing further spread time effects. The use of the S2 scintillator is to discriminate between single and multi-particle events. The discrimination threshold depends on the energy deposited in S2. When the signal corresponds to multiple events, the time-to-amplitude converter (TAC) is inhibited during the acquisition for that given threshold. Figure 3.17 shows a typical energy spectrum measured by S2, where the channel number is linearly correlated with the particle energy. Each peak corresponds to one, two and three simultaneous particles, which are clearly separated.

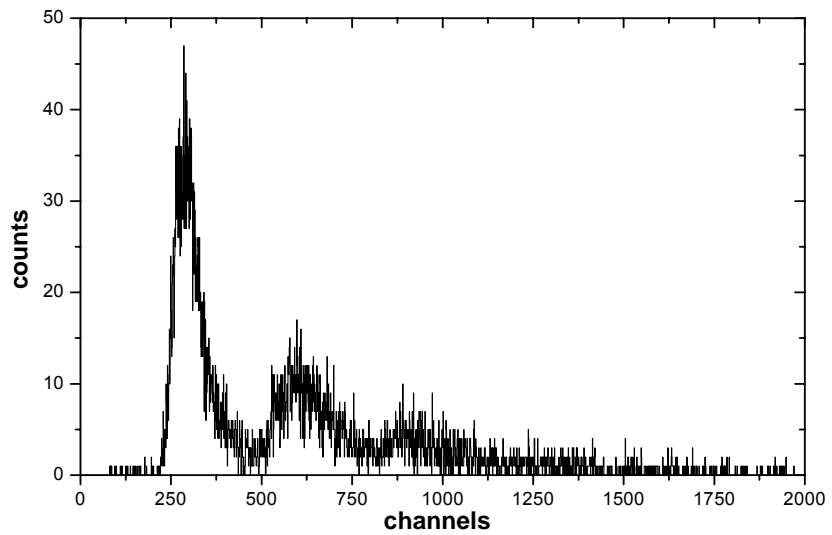


**Figure 3.17:** Charge spectrum obtained by the counter S2 in the test apparatus.

### 3.3.3. Results and interpretation

For each scintillator bar, data have been taken at 11 positions along the bar itself and for 4 different impact angles, for a total of 38 points. After selection of single positron events, using the appropriate threshold discrimination, each point consists of at least 3500 events. Typical time resolution distribution curves, for BC408 and BC404 scintillator bars, are displayed in Figure 3.18.

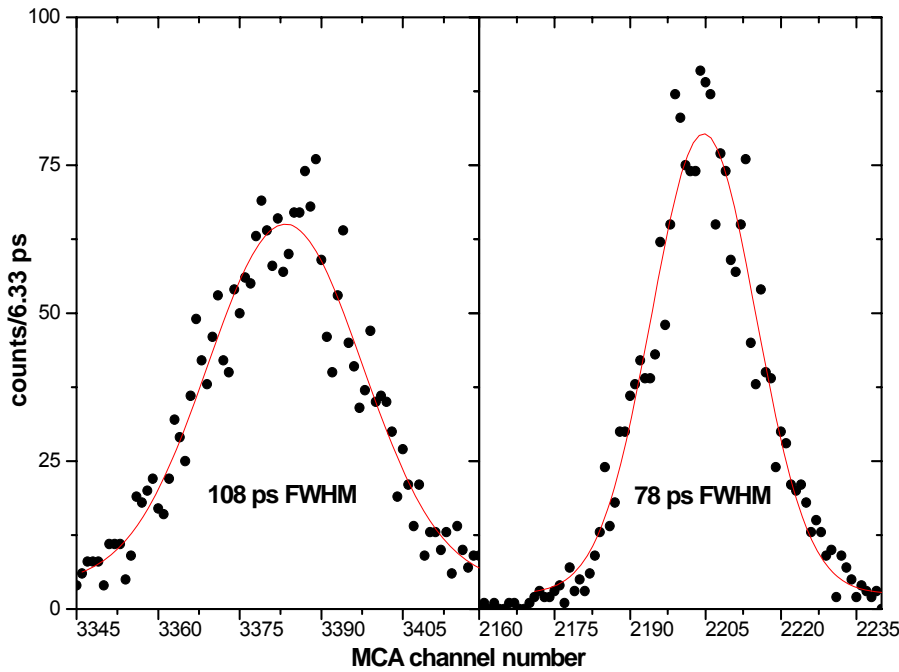


**Figure 3.18:** Scintillator experimental time resolution (dots) and best Gaussian fit (line) for BC408 (left) and BC404 (right).

The details about data acquisition system have been already described in paragraph 3.3.1. The resolution of the electronic system (DAQ) is 6.33 ps/ch. The calculated resolution is clearly better for the BC404 scintillator. In Figure 3.19, the time resolution as a function of beam impact position relative to the bar centre, for different impact angles and for both scintillator bars is plotted.

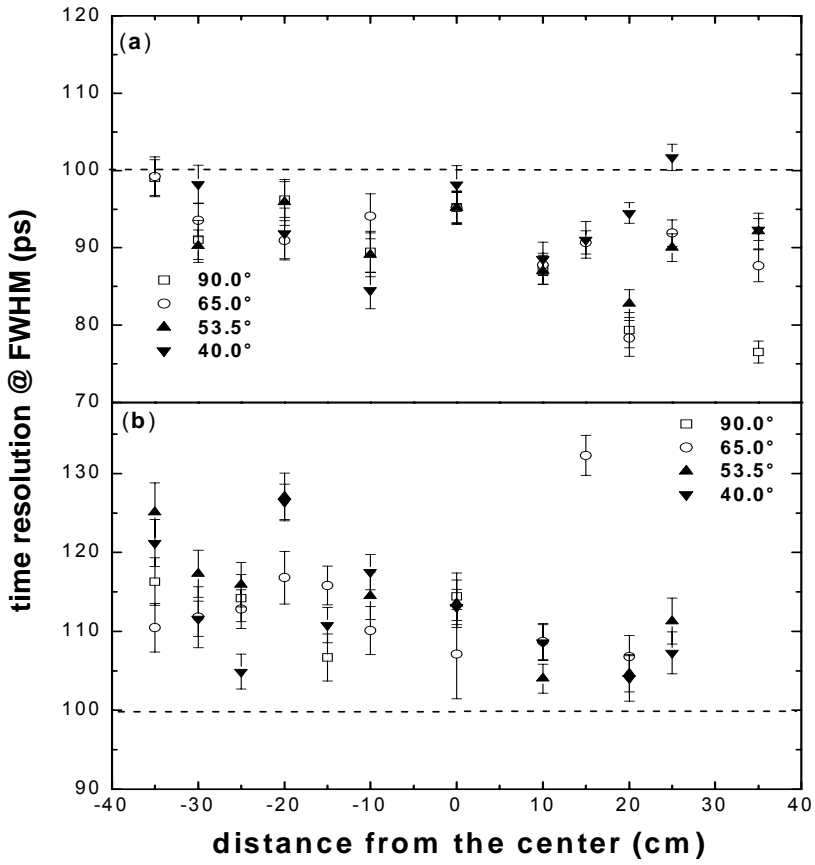


**Figure 3.19:** Time resolution as a function of the position for BC408 (bottom) and BC404 (top), with respect to the bar centre and for different impact angles. The dashed line represents the required limit resolution.

The error bars are those given by the Gaussian fit multiplied by the electronic acquisition resolution, 6.33 ps/ch, by the RMS-FWHM conversion factor, 2.35, and divided by 2, as described in paragraph 3.3.1. The results of Figure 3.19, clearly demonstrate that the scintillation type BC404 shows a better performance than the BC408. Furthermore, for BC404, which has been selected on this basis, the time resolution is rather insensitive to the impact position. It is worth noting that for the chosen scintillator, the average time resolution is  $\sigma \sim 39$  ps ( $\sim 92$  ps FWHM). In Table 3.4 the latest time resolution results, from different experiments, are shown.

**Table 3.4:** Comparison among different scintillating timing detectors.

Scintillator Types	PMT's	LxWxT (cm)	$\sigma$ (ps)	Ref.
BC420	R1828-01	40x7x2.2	123	<sup>13</sup>
BC408	R3478	12-48x1-1.25x1.5-2.4	85	<sup>14</sup>
BC408	H1949	200x8.5x5	110	<sup>15</sup>
BC408	XP2020	180-250x21x2.5	160	
BC408	XP2020	280x10x5	139	<sup>10</sup>
NE110 <sup>*</sup>	XP2020	210-300x21x2	300	<sup>16</sup>
NE110 <sup>*</sup>	XP2020	300x9.3x4	170	<sup>17</sup>
BC408	XP2020	305x10x5	110	<sup>18</sup>
NE Pilot F <sup>**</sup>	XP2020	317.5x15.6x5.1	163	<sup>11</sup>
BC408	XP43132B/D1	32-450x15-22x5.1	163	<sup>19</sup>
BC404	R5924	80x4x4	40	MEG

<sup>\*</sup> This type of scintillating fiber has the same physical properties<sup>20</sup> of BC412.

<sup>\*\*</sup>This type of scintillating fiber has the same physical properties<sup>20</sup> of BC408.

Different types of scintillating detectors, shaped as bars, are reported, with different sizes and types of PMTs; the results also correspond to different experimental conditions and detector time resolution performances. The experimental data indicate that the attained results in this work provide the best time resolution ever achieved up to our knowledge.

### 3.3.4. Validation test in magnetic field

During the tests carried out in Frascati, also the time resolution has been measured using a laser diode ( $\lambda=408$  nm, width=250 ps and rise time=100 ps) along with a fast pulse generator. This measurement has been repeated in the same conditions at PSI inside the COBRA magnet, to verify the reproducibility of the results in presence of magnetic field. In order to be sure that the signal generated by the positrons in the fiber was correctly reproduced, the signal amplitude was checked in both phototubes coupled to the bar; then, the light introduced by the laser gave the same result. The only change made was to increase the bias voltage of the PMTs from 1600 and 1750 V to 1700 and 2300 respectively, to compensate the effect of the field. As reported in Figure 3.20 no appreciable variation of the time resolution has been observed.

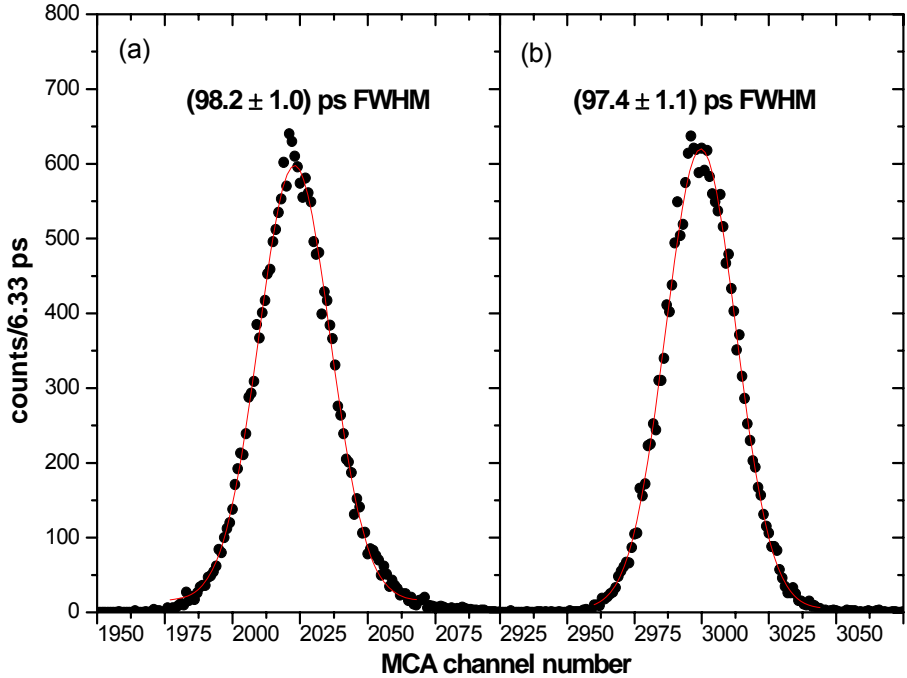


**Figure 3.20:** Experimental time resolution (dots) and best Gaussian fit (line) for BC404 inside the COBRA magnet (a) and at BTF (b).

Next phase will consist in evaluating the time resolution between  $\gamma$  and  $e^+$  processes, in accordance to the MEG proposal. The total required resolution is 150 ps FWHM, corresponding to  $\sim 100$  ps for each detector. The present results indicate that the TC time resolution is about 92 ps FWHM, at the impact of the positron. In addition, one has to consider the uncertainty generated by the “swim back” of the positron track to the target. This has been estimated by Monte Carlo simulated events and by their reconstruction through the MEG chambers, to be about 40 ps FWHM, providing a total uncertainty of 100.3 ps. If a similar resolution is attained also for the  $\gamma$ -rays, the predicted resolution can easily be reached. This is an order of magnitude better than the time resolution reached by the MEGA experiment<sup>21</sup>, precursor of MEG.

### 3.4. Front-end electronics

As described in paragraph 2.4, the signals coming from all the phototubes are digitalized using a digitizer with an adjustable sampling frequency from 600 MHz to 2.5

GHz. In general, the formation time of a single impulse from the timing sub-detector is influenced by several factors as: the rise time of the PMT, 2.5 ns<sup>[1]</sup>, the rise time of the scintillator, 0.7 ns<sup>[1]</sup>, and the length of the cable, which degrades the signal of < 1 ns. This last value has been experimentally obtained using an EnviroFlex 400<sup>[22]</sup> cable of the length, ~10 meters, needed to bring the information of the PMTs from inside the COBRA magnet to the front-end electronics. Table 3.5 shows the obtained values for different cables, Enviroflex 400, RG 58CU e RG 316. The measurements have been carried out using a square wave with amplitude of 500 mV, pulse width of 25 ns, and rise and fall times of 0.26 ns. The length of the cables was 10 meters.

**Table 3.5:** Experimental leading edge of different cables.

<b>Fast step response</b>	<b>RG58CU</b>	<b>Enviroflex 400</b>	<b>RG316</b>
Leading Edge 20-80% (ps)	650	570	940
Amplitude (mV)	464	465	442

It can be noted that, among the different cables tested, Enviroflex 400 has the smallest attenuation and also the best generation time of input signal. Moreover, it has a double silver-copper screening<sup>22</sup>, extremely useful for the use in external magnetic field as in MEG experiment, and a high flexibility, very important when the available space and geometries are small. Figure 3.21 shows the response of the cable to the signal transmission. It can be seen that the input signal is positive (left) while the output of the cable is negative (right). This is due to the fact that the pulse generator (LeCroy 9212) has two identical outputs, with the same phase and time, complementary one to each other; therefore, the positive one is sent to the oscilloscope (Tektronix TDS 7254) and the negative one goes through the cable to be tested.

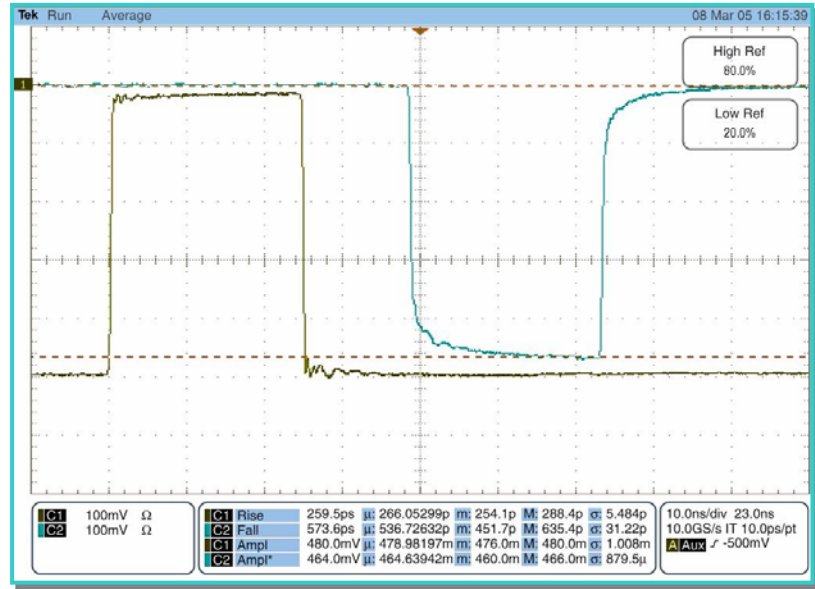


**Figure 3.21:** Reference signal (left) and Enviroflex 400 response (right).

Indeed, considering all these factors, the signal produced by a PMT has a minimum formation time of about 4.2 ns. Figure 3.22 shows the rise times,  $\sim 5$  ns, of two pulses obtained during one of the tests carried out at BTF in Frascati.

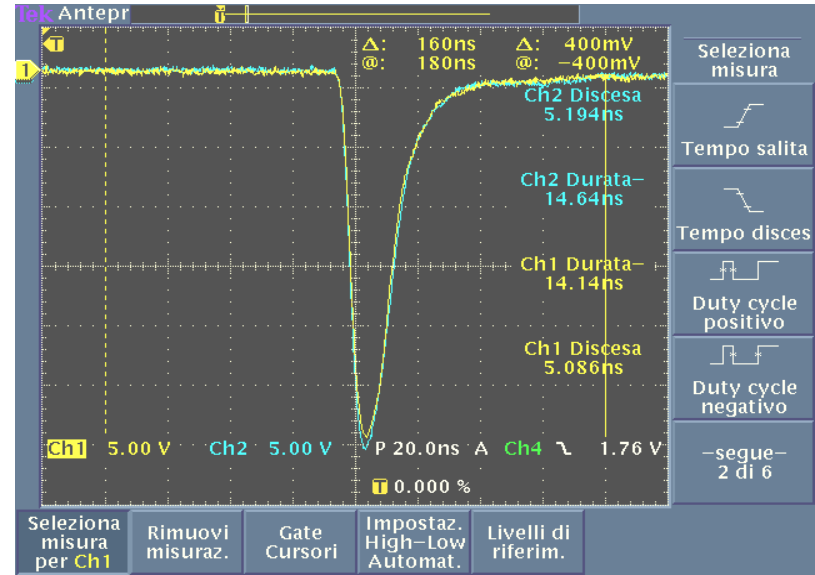


**Figure 3.22:** Signals obtained by two PMTs.

### 3.4.1. Considerations on PMT time resolution

To drive some considerations about the PMT resolution, let us suppose that the absolute value of the signal coming from a PMT increases linearly, as shown in Figure 3.23.

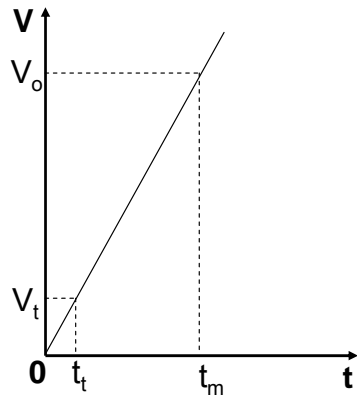


**Figure 3.23:** Lay-out of the signal formation for time-walk effect estimation.

This hypothesis is consistent with our working conditions, considering that we are going to work at a fixed threshold and we are not interested on what happens around the maximum of the signal. In this case, the time of the signal,  $t_t$ , is given by  $t_t = \frac{V_t}{V_0} \cdot t_m$ ,

where  $t_m$  is the rise time of the signal. Therefore the uncertainty on  $t_t$  due to the three

quantities  $V_t$ ,  $V_0$  and  $t_m$  is given by  $\delta(t_t) = \frac{V_t}{V_0} \cdot t_m \left[ \left( \frac{\delta V_t}{V_t} \right) + \left( \frac{\delta V_0}{V_0} \right) + \left( \frac{\delta t_m}{t_m} \right) \right]$ . It is worth

noting that  $\delta(t_t)$  is proportional to the factor  $f = \frac{V_t}{V_0} \cdot t_m$  and thus to the rise time of the

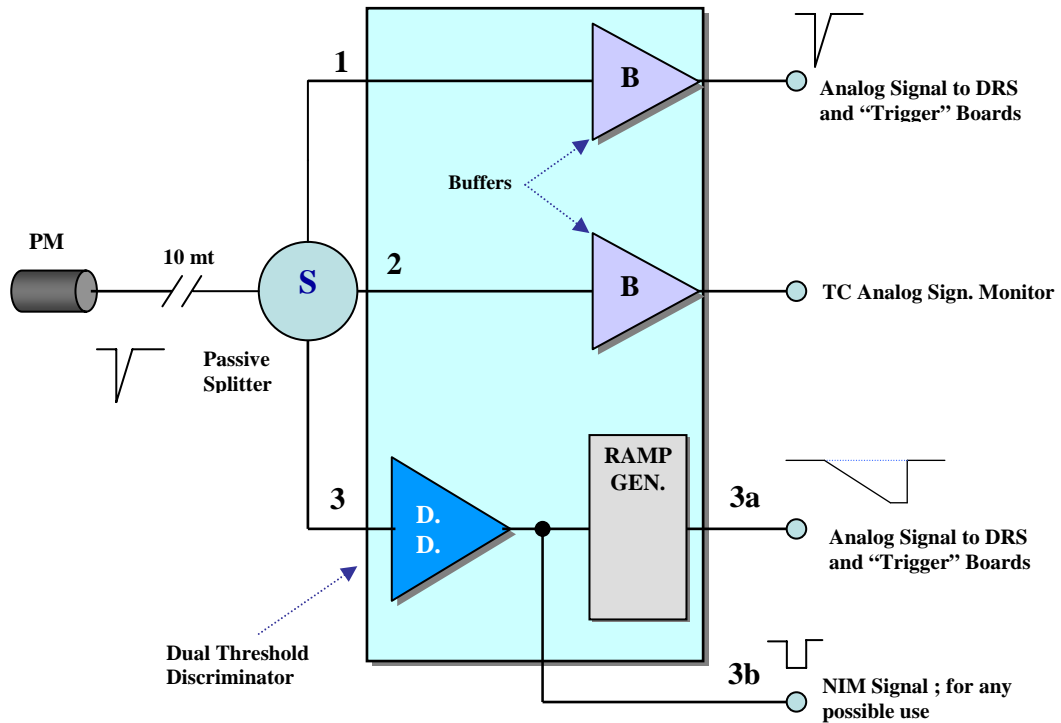
signal. By substituting the measured values in the expression of  $f$ , i.e. 10 mV, 10 V and 5 ns for  $V_t$ ,  $V_0$  and  $t_m$  respectively, one obtains that  $f$  maximum is of the order of 5–10 ps. The main reason to use a double threshold technique is to make the time-walk effect negligible, so that no time-amplitude corrections on signals are needed.

To be sure that the signals of the PMTs are correctly digitalized allowing the reconstruction of the rise time (and thus of the signal timing) of the pulses by the 2 GHz sampler, the signals should be stretched before being sent to the DRS. The sampler jitter

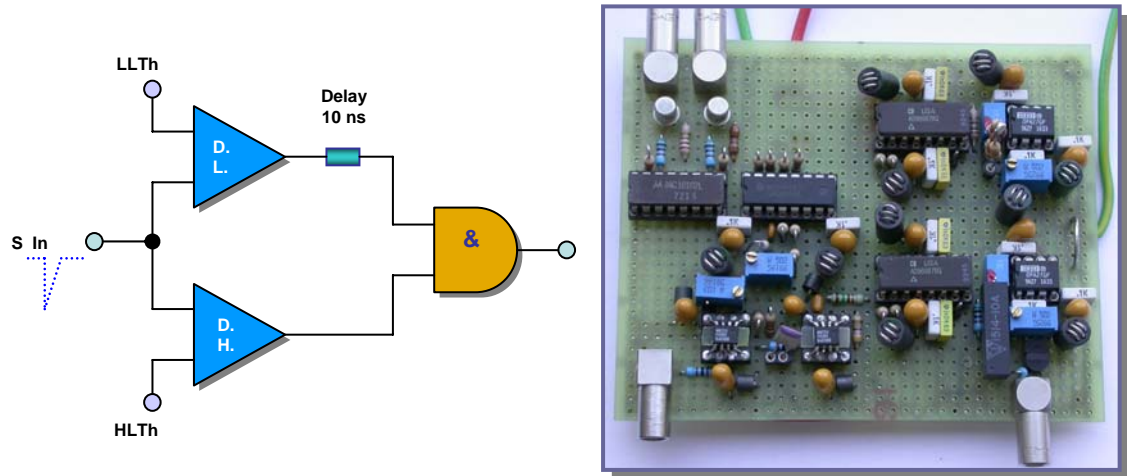
in fact, 150 ps<sup>[23]</sup>, does not allow a reliable time reconstruction of the signal, and therefore if the signal is sent directly to the DRS, it can sample only n points, with n<10. In this way, the uncertainty would be about  $\frac{500}{\sqrt{n}} \text{ ps}$ , equivalent to a minimum of  $\sim 160 \text{ ps}$ .

Figure 3.24 shows a scheme of the front-end electronics for the PMTs of the timing counter. Once reached the passive splitter, the signal is addressed to tree different lines.

- Line 1: the analogic signal sent to the trigger board is used to get a time coincidence between the photon signal in the calorimeter and that of the positron in the timing counter. The signal time is obtained by a linear interpolation on the rise front, with a resolution between 2.5 and 5 ns. The coincidence window TC-LXe of the trigger is 10-20 ns.
- Line 2: the analogic signal can be view before it is formed. This output can be used to estimate the charge accumulated by each PMT determining the real aging ( $100 \text{ mA} \times 100 \text{ h}$ )<sup>[1]</sup>.
- Line 3: the analogic signal goes through the double threshold discriminator as shown in Figure 3.25 (left). The double threshold discriminator, through the use of trimmers, allows to set the low (10-300 mV) or high (10 mV-5 V) threshold level. Once the signal is formed, it is stretched and then sent to DRS. The ramp generator is designed to produce both a ramp with rise time between 7 and 60 ns and a square wave with rise front of the order of ns and a variable amplitude up to 1.2 V, by using a shape selector. In this way, it should be possible to get rid of any problem related to the limited dynamic of DRS.



**Figure 3.24:** Layout of the front-end electronics.



**Figure 3.25:** Layout of dual threshold discriminator (left) and Bread Board prototype (right).

In Figure 3.25 (right) a prototype of the ramp generator and of the double threshold discriminator, is shown. The recent tests at the LNF (January 2006) confirmed that the desired time resolution can be reached also using the double threshold discriminator prototype, by carrying out a measurement with a scintillator bar coupled with two PMTs in the final configuration; the obtained resolutions are shown in Figure 3.26.

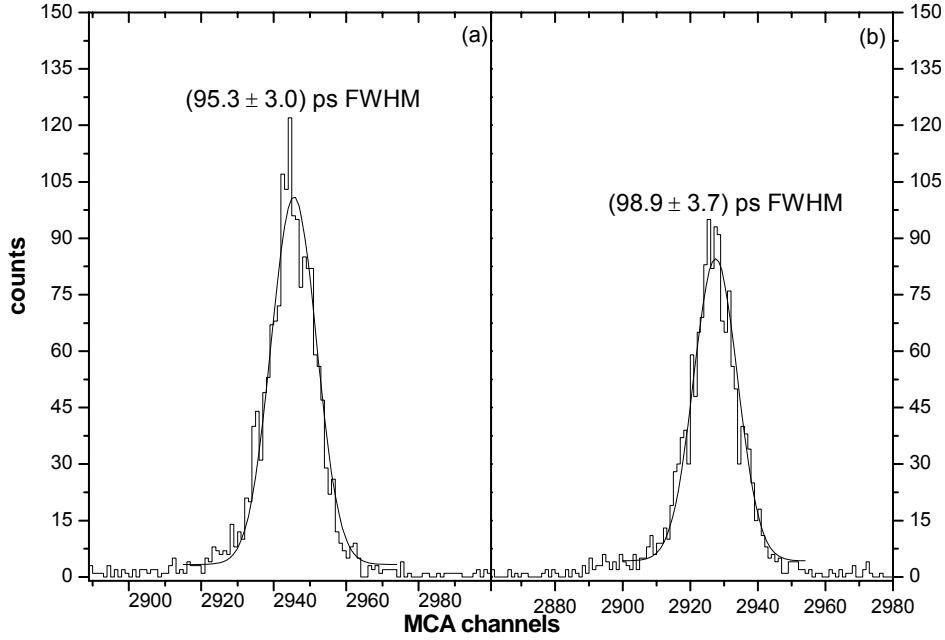


**Figure 3.26:** Experimental time resolution (vertical steps) and best Gaussian fit (line) using traditional electronic (a) and double threshold discriminator prototype (b).

Figure 3.26 shows a comparison between the time resolutions obtained with the NIM electronics used in all the beam tests described in this thesis (Octal Discriminator Philips mod. 710, Delay Time Philips mod. 792 and Logic Unit LeCroy mod. 365 AL) (a) and with the electronics that will be used in MEG experiment, with the low and the high thresholds at  $\sim 30$  mV and  $\sim 200$  mV respectively (b). The electronics common to both measurements consisted of a time-to-amplitude converter (TAC) and of a multi-channel analyzer (MCA). The results obtained with the two setups do not show significant differences.

### 3.5. Final measurements

Recently (January and April 2006), the preliminary tests for the characterization of the first timing sub-detector have been carried out. This sub-detector will be inserted inside the COBRA magnet within the end of June 2006. The tests of the detector in the final configuration is extremely important for the experiment for several reasons: the use of the definitive bars and their characterization, the use of supports and plastic parts

designed for the interfacing between phototube and scintillator, the gluing and painting of the plastic parts, the use of final PMTs and the coupling between them.

The modification of the mechanical chariot of Figure 3.15 allowed to use the support that will be inserted inside the COBRA. A scheme of the “cradle” realized at the University of Genova is reported in Figure 3.27. In particular, bottom panel of Figure 3.27 shows the tilting angle of the bars. In fact, in order to increase the uniformity of the track, the scintillator bars have been rotated by  $20^\circ$  in the plane orthogonal to the z axis. This value has been obtained using a MC simulation. The rotation of the bars became necessary to improve the uniformity of the track inside the scintillator and to reduce the time-walk effect.

### 3.5.1. Preparation of the bars

These recent tests have been carried out using 15 scintillator bars which will be employed in the realization of timing counter up-stream. The bars have been shaped as shown in Figure 3.13, by a numerically controlled milling cutter with a diamond insert, specially designed to pattern plastic scintillators<sup>24</sup>. The next phase of the preparation consisted in the bar polishing, which is essentially divided in two steps. First, the bars are roughly polished by means of special papers and abrasive pastes, in order to reduce the roughness of external surfaces down to values of the order of few microns. Then, the bars are hand polished using 3 and 1  $\mu\text{m}$  diamond pastes.

By this procedure, the roughness of the scintillator bars can be improved of almost an order of magnitude, up to values in the range 0.25-0.10  $\mu\text{m}$ . In a typical scintillator counter, the light will be internally reflected tenths of times before reaching the PMT.

This implies that the surface quality of the scintillator (roughness, dust, scratches, fingerprints etc.) is very important\*.

---

\* A surface can be considered smooth when its roughness is of the order of one fourth of the incident radiation wavelength.

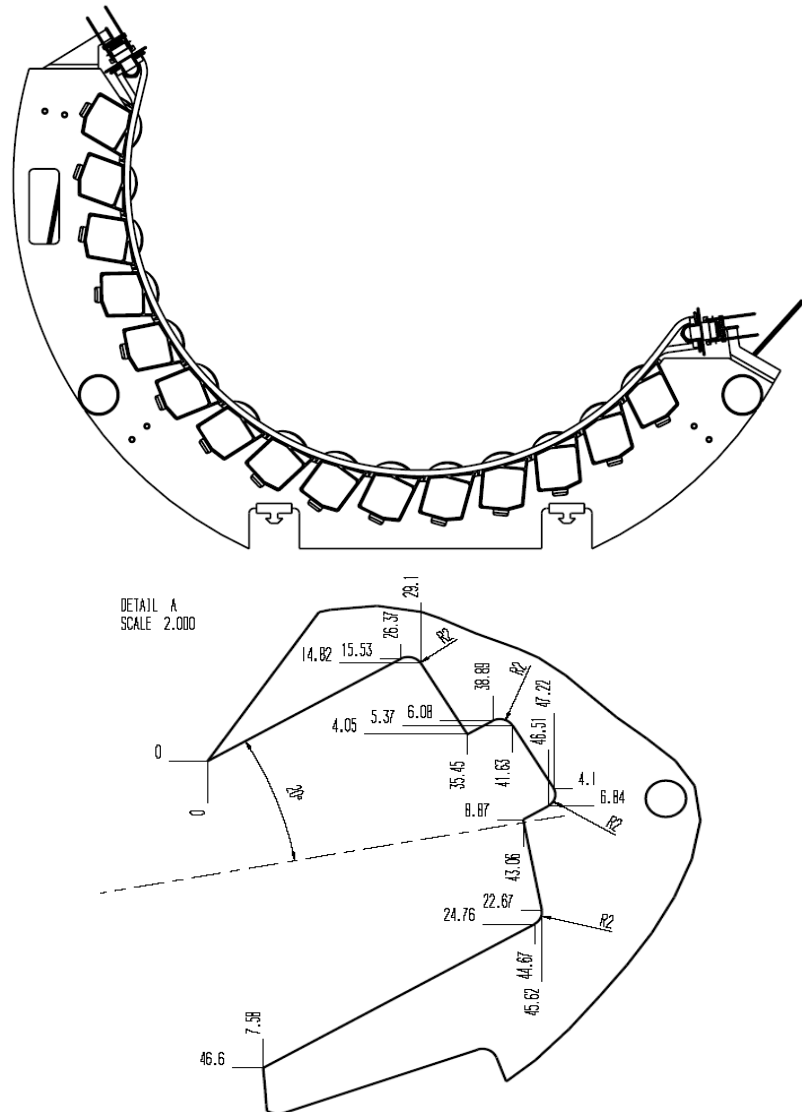


**Figure 3.27:** Final mechanical support of the timing counter: frontal view (top) and a particular of the profile where the tilting angle of the scintillator bars is visible (bottom).

In a first approximation, the number of reflections,  $n$ , is given by:

$$n = \frac{H}{W} = \frac{L \cdot \tan \theta}{W}, \text{ where } W \text{ is the scintillator thickness, } L \text{ is the distance between the}$$

point where the light is generated and the end of the bar and }  $H$  is the distance between the scintillator and the extension of the light trajectory at a fixed angle, as shown in Figure 3.28. Therefore, for a distance  $L=40$  cm and a thickness  $W=4$  cm, typical of

MEG experiment, one obtains  $n = \frac{40 \cdot \tan \theta_{\lim}}{4} \approx 10$  reflections above the limit

angle  $\theta_{\text{lim}} = \sin^{-1}\left(\frac{n_1}{n_2}\right)$ , in agreement with the measured value. In this expression,  $n_1$  and  $n_2$  are the refraction indexes of air and scintillator respectively. Therefore, considering a reflection efficiency,  $RE$ , of 0.994 %<sup>[25]</sup>, one obtains a percentage  $I$  of transmitted light of about  $I = RE^n = 0.994^{10} \approx 0.94$ , with a 6% loss.

It is evident that the light loss in these conditions can be neglected whereas, in case of scintillating fibers, this factor becomes important (see Chapter 4); in fact, the number of reflections, related to the material dimensions, strongly increases ( $n \sim 100$ ).

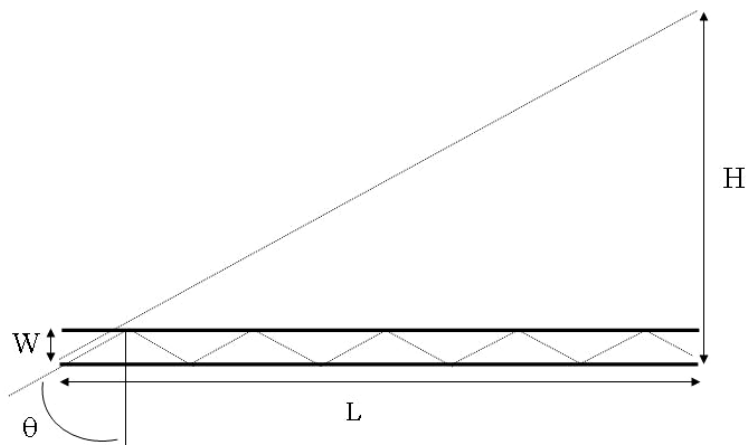


**Figure 3.28:** Scheme of the number of reflections.

Subsequently, the bars have been inserted inside the plastic housing and the scintillator-PMT sockets have been glued; Figure 3.29 shows pictures of these two parts.

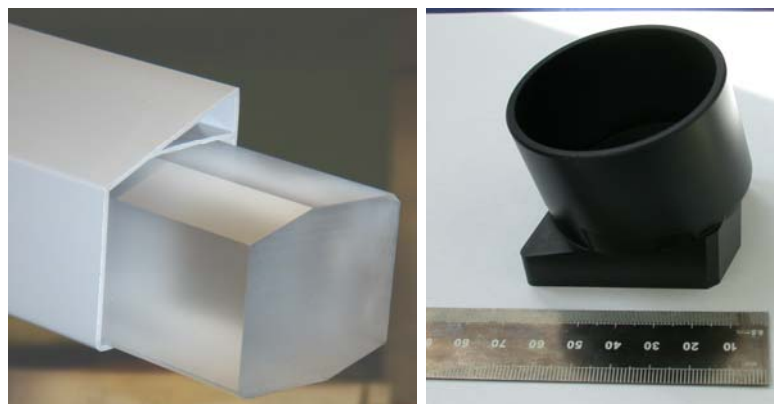


**Figure 3.29:** Pictures of BC404 bar, plastic housing and interface socket, in the final design.

The materials that have been used to realize the supports are:

- Acrylonitrile Butadiene Styrene (ABS) for the plastic housing;
- ERTACETAL C for the socket and the mechanical support. This material has excellent creep resistance and dimensional stability, which makes it ideal for machining of precision parts<sup>26</sup>.

### 3.5.2. Preparation of the PMTs

The Hamamatsu R5924 is a 19-stage dynode PMT with a bialkali photocathode and borosilicate window. This photomultiplier tube has been supplied by the manufacturer in an assembly that contains the tube, the voltage divider, the high-voltage cable and the signal cable. The PMT is housed in a Poly Oxy Methylene black cylindrical box<sup>2</sup>. To reduce the detector encumbrance, it has been decided to buy only the tube, without the electronics and its housing, so that it was possible to save ~2 cm in length and ~1 cm in width, as shown in Figure 3.30. Moreover, the resistances in the voltage divider have been changed from  $330\text{ K}\Omega$  to  $300\text{ K}\Omega$ , to get an increase in the maximum supplied current of about 10 %.

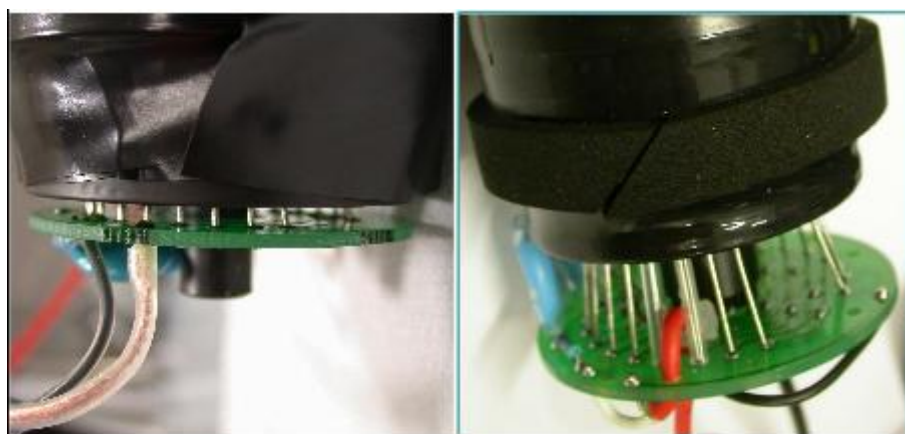


**Figure 3.30:** Actual dimensions of PMT (left) and PMT as provided by Hamamatsu (right).

### 3.5.3. Conclusions

The last tests carried out at BTF in April 2006 confirmed the previously obtained results. A detailed description of these results is reported in Dussoni's Ph.D. Thesis<sup>27</sup>. With 8 available PMTs, only three bars have been fully characterized, whereas the others were characterized using two phototubes as a reference. It is clear that a fundamental factor in the PMTs selection is the TTS measurement. Indeed, the detector resolution is proportional to this factor, which therefore has to be accurately known. The assembly and coupling procedure between PMTs and scintillator bars will be discussed once the properties of all the available phototubes will be known. In general, the PMTs with the higher gain will be inserted in the inner position, while those with lower gain will be placed in the outer part, where the effect of the magnetic field is less evident.

Concerning the choice of the scintillator, the MC simulations confirmed the experimental results. In fact, working at a low threshold as shown in paragraph 3.4.1., the time resolution is connected to the arrival statistics of the first photons and therefore the crucial factor is the formation rise time of the light pulse inside the scintillator. Figure 3.31 shows the number of photoelectrons arriving on PMT as a function of time. Considering a  $\sim 0.8$  ns time interval for both scintillators, the number of produced photoelectrons is  $\sim 24$  and  $\sim 36$  for BC 408 and BC 404 respectively.

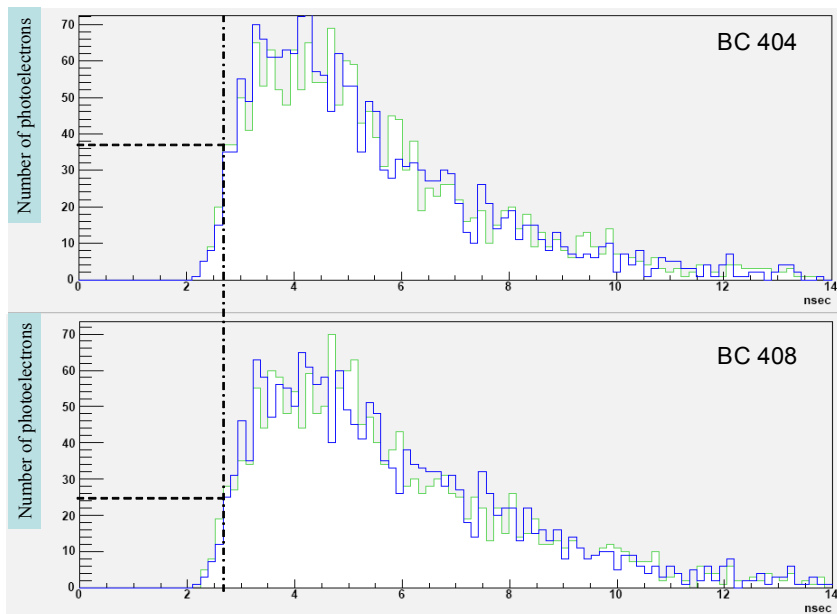


**Figure 3.31:** Time distribution of the number of produced photoelectrons in two different scintillators obtained from a MC simulation.

Therefore, in a first approximation, the PMT time resolution,  $\sigma_{pmt} = \frac{TTS}{\sqrt{N_{pe}}}$

improves of about 20%. This value is in agreement with the difference between the two experimental values obtained in the tests described in paragraph 3.3.2, where the average resolutions were 91 ps for BC404 and 113 ps for BC408.

## Bibliography Chapter 3

---

- <sup>1</sup> A. Baldini, R&D proposal to INFN, “The MEG experiment: search for the  $\mu^+ \rightarrow e^+ + \gamma$  decay at PSI”, September 2002.
- <sup>2</sup> Hamamatsu Photonics, [www.hamamatsu.it](http://www.hamamatsu.it).
- <sup>3</sup> M. Bonesini et al., proceeding of Beaune 2005, IV Conference on New Developments in Photodetection, to be published on NIMA.
- <sup>4</sup> <http://savannah.psi.ch/viewcvs/trunk/megmc/gem/bfield/lib/cobrafld.hbook?root=meg&rev=1651&view=log>.
- <sup>5</sup> W. B. Atwood, Lecture at SLAC Summer Institute, October 1980.
- <sup>6</sup> <http://physics.nist.gov/PhysRefData/Star/Text/contents.html>
- <sup>7</sup> F. Gatti, Talks from Review Meetings, February 2004, <http://meg.web.psi.ch/docs/>.
- <sup>8</sup> Saint-Gobain Crystal, [www.detectors.saint-gobain.com](http://www.detectors.saint-gobain.com).
- <sup>9</sup> M. Baldo-Ceolin et al., Nucl. Instr. and Meth. A 532 (2004) 548.
- <sup>10</sup> Y. Kubota et al., Nucl. Instr. and Meth. A 320 (1992) 66.
- <sup>11</sup> E.S. Smith et al., Nucl. Instr. and Meth A 432 (1999) 265.
- <sup>12</sup> <ftp://megftp@pc-grid-alex.roma1.infn.it/>.
- <sup>13</sup> B. Adeva et al., Nucl. Instr. and Meth A 491 (2002) 41.
- <sup>14</sup> G. Palla et al., Nucl. Instr. and Meth. A 451 (2000) 406.
- <sup>15</sup> V. Sum et al., Nucl. Instr. and Meth. A 326 (1993) 489.
- <sup>16</sup> M. Baldo Ceolin et al., Nuovo Cimento 105A (1992) 1679.
- <sup>17</sup> G.C. Bonazzola et al., Nucl. Instr. and Meth. A 356 (1995) 270.
- <sup>18</sup> S. Benerjee et al., Nucl. Instr. and Meth. A 269 (1988) 121.
- <sup>19</sup> J.S. Brown et al., Nucl. Instr. and Meth. 221 (1984) 503.
- <sup>20</sup> [www.apace-science.com/eljen/list.htm](http://www.apace-science.com/eljen/list.htm).
- <sup>21</sup> M. L. Brooks et al., Phys. Rev. Lett. 83 (1999) 1521.
- <sup>22</sup> Huber+Suhner group, [www.hubersuhner.com](http://www.hubersuhner.com)
- <sup>23</sup> S. Ritt, Talks from Review Meetings, February 2005, <http://meg.web.psi.ch/docs/>.
- <sup>24</sup> <http://www.sandvik.it>
- <sup>25</sup> X. H. Yang et al., NIM A 354 (1995) 270.
- <sup>26</sup> [http://www.dotmar.com.au/products/acetal/ertacetal\\_c.htm](http://www.dotmar.com.au/products/acetal/ertacetal_c.htm).
- <sup>27</sup> S. Dussoni, MEG collaboration, Ph.D. Thesis, “Search for Lepton Flavour Violation: The MEG experiment”, May 2006.

## *Chapter 4*

### **Triggering sub-detector**

This chapter is mainly devoted to the description of the triggering sub-detector that provides the position of the impact point of positrons and triggers the data system, with a resolution of  $\sim 10$  cm and 10 ns respectively. Initially, the idea was to use this part of the detector completely bared on scintillator bars, similarly to the timing sub-detector described in Chapter 3<sup>[1]</sup>, and the scintillator bars would be coupled at each end side with photomultipliers. Currently, in order to avoid the huge PMTs loss of performance, in particular the gain, caused by magnetic field perpendicular to the counter or the use of complex light guides coming out from the magnet, it has been investigated to employ scintillator fibers coupled avalanche photodiodes (APDs).

In the first part of this chapter, the physical properties of the main components of the detector will be described: scintillator fibers and APDs. The second part will be devoted to the characterization of the APD's gain and dark current, and to the study of light transmission and attenuation in fibers. Finally, the design of this apparatus will be presented as it will be inserted in the whole MEG experimental set-up.

## 4.1. Detector concept

Each inner part detector consists of a layer with 128 scintillating fibers with square section ( $5 \times 5 \text{ mm}^2$ ), viewed on each side by an APD. These devices show a slightly worst gain performance with respect to PMTs, but can operate in environments with strong magnetic field ( $\sim 1 \text{ T}$ ).

### 4.1.1. Scintillating fibers

Among the materials for impact point detection of charged particles, the scintillating fibers are extremely promising. Their small diameter allows to have a low occupancy rate; besides, a fluorescence time decay as short as a few nanoseconds makes a high rate operation possible, being able to be used as trigger pulses generator. Figure 4.1 shows the typical elements of a plastic scintillating fiber. The scintillating core material is clad with a non-scintillating material of lower refractive index, which is at least several wavelengths thick. A thin opaque extra mural absorber, EMA, is that can be applied to the outer fiber surface, primarily to eliminate crosstalk among closely packed fibers, even if this material decreases the signal intensity produced inside the fiber<sup>2</sup>. There is also a special class of fibers named Multiclad, which have a second layer of cladding with an even lower refractive index, permitting a total internal reflection at a second boundary. The additional photons guided by multiclad fibers increase the output signal up to 60 % over conventional single clad fibers<sup>2</sup>.

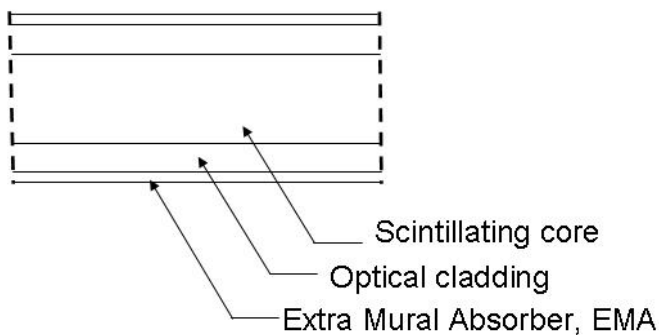


**Figure 4.1:** Elements of a scintillating fiber.

The fiber that we used in this work is named BCF 20 Multiclad and is developed by Saint-Gobain Crystals<sup>2</sup>. This fiber has a square cross-section of area  $5 \times 5 \text{ mm}^2$ , including a double cladding wall thickness of 0.2 mm, more than 890 mm in length\* and is typically used for fast signal generation. It has an emission peak at 492 nm, a time decay of 2.7 ns and a nominal attenuation length  $\geq 3.5 \text{ m}$ . This fiber yields about 8000 photons per MeV from a minimum ionizing particle. The main characteristics of single and multi clad-fibers are summarized in Table 4.1<sup>[2]</sup>.

**Table 4.1:** Common properties of single and multi-clad fibers<sup>2</sup>.

Single-clad Fibers Properties		Multi-clad Fibers Properties	
Core Material	Polystyrene	Second cladding material	Flour-acrylic
Core refractive index	1.60	Refractive index	1.42
Density (g/cm <sup>3</sup> )	1.05	Thickness, square fiber	2% of fiber size
Cladding material	Acrylic	Trapping efficiency, round fiber	5.6% minimun
Cladding refractive index	1.49	Trapping efficiency, square fiber	7.30%
Cladding thickness, square fiber	4% of fiber size		
Trapping efficiency, square fiber	0.04		
Trapping efficiency, round fiber	3.44% minimun		
Operating temperature	50°C to -20°C		
Vacuum compatible	Yes		

Along with the larger surface exposition to the incident particles, another property of square cross section fibers is that the fraction of photons,  $L$ , light piped along one direction of the fiber<sup>3</sup>, proportional of the differential solid angle, given by equation 4.1, is independent of the light emission position within the volume of the fiber:

$$L = \frac{4}{4\pi} \int_{\theta=\theta_c}^{\pi/2} \sin\theta d\theta \int_{\phi=\arccos(\cos\theta_c/\sin\theta)}^{\pi/2} d\phi, \quad (4.1)$$

where  $\theta_c$  is the critical angle of reflection,  $\theta$  and  $\phi$  represent the angles in spherical coordinates. For circular fibers,  $L$  is a function of light emission position within the

---

\* In MEG experiment there are two different fiber lengths, 893 and 915 mm respectively, as show in the following.

fibers and the variation in  $L$  is such that it increases as the “particle impact parameter” increases, where this quantity indicates the perpendicular distance from the particle trajectory to the fiber center, in units of the fiber radius<sup>3</sup>.

In this way, it is more straightforward to identify if the positrons cross the section of the fiber completely or if they just hit it close to an edge. This can be done by using a template of the signal waveform for the first situation (positron fully cross the scintillator) and setting in this way a threshold near the maximum.

#### 4.1.2. Avalanche Photodiodes

Photosensors made of semiconductor materials received an involving interest in recent years, being specially tailored for the needs of optical applications and being produced at a relatively low cost. Size, and geometry in general, spectral response and other parameters such as reduced power requirements, reduced sensitivity to temperature and insensitivity to magnetic fields, can be almost chosen freely. Several structures are commercially available, such as PIN diodes, APDs, CCDs, phototransistors, etc. The sensors can be made of all sorts of semiconductor materials: Si, Ge, GaAs, InGaAs, but also of materials with wide-band gap like InI, AgI<sub>2</sub>, PbI<sub>2</sub>, TlBr for applications at high temperatures or for particular spectral response requirements<sup>4</sup>.

Considering that the number of photons produced in a fibre depends on its geometry, it is very important to find a photon detector with high quantum efficiency and good geometrical matching to read out each individual fiber efficiently.

Hamamatsu Photonics developed avalanche photodiodes which are well-suited for these demanding applications. This APD is made by epitaxial growth on low resistivity N-type silicon and by ion implantation and diffusion. The P-type material in front of the amplification region, which forms the P-N junction, is less than 7  $\mu\text{m}$  thick, in order to reduce the sensitivity to ionising radiation. Surface currents are suppressed by making a groove, which is  $\sim$ 30  $\mu\text{m}$  deep and wide as illustrated in Figure 4.2<sup>[5]</sup>.

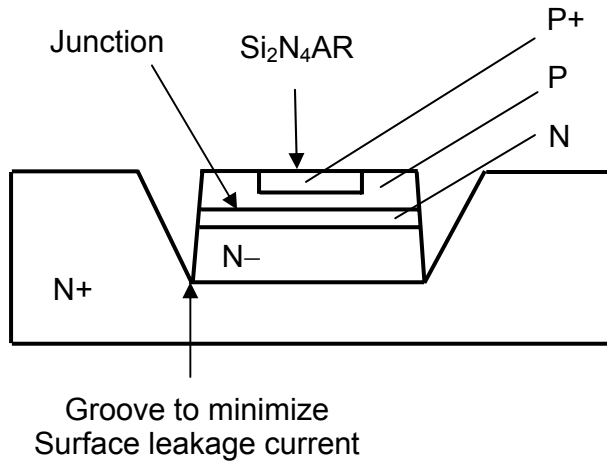


**Figure 4.2:** Structure of an APD produced by Hamamatsu Photonics, (AR stands for antireflecting).

For the detector in this work, APD type S8664-55 was used, which has an active surface of  $5 \times 5 \text{ mm}^2$ , perfectly matching with the dimensions of scintillating fibers. Furthermore, as shown in Figure 4.3, the quantum efficiency (Q.E.) of this device is  $\geq 80\%$  for wavelengths in the range 500-800 nm.

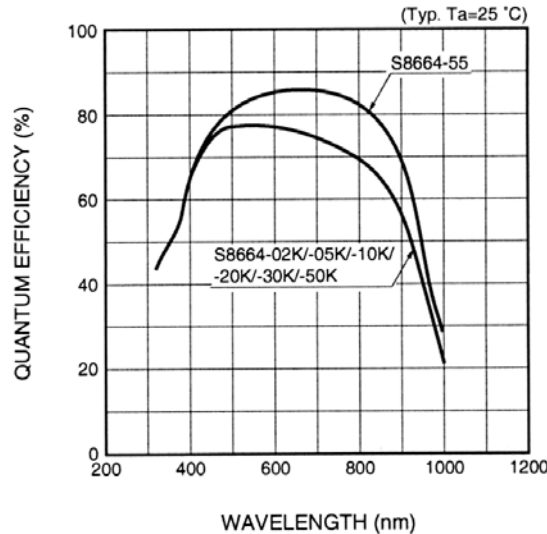


**Figure 4.3:** Quantum efficiency as function of wavelength of an APD produced by Hamamatsu Photonics (type S8664) for different active areas<sup>6</sup>.

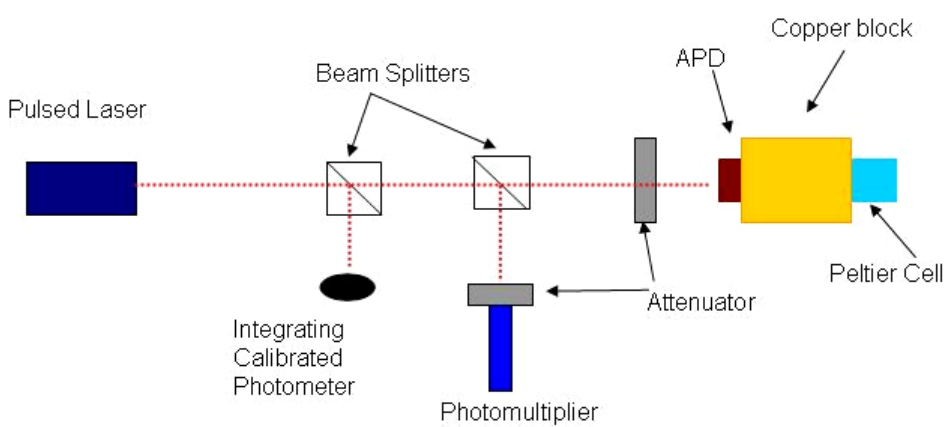
In comparison with photomultiplier tubes, APDs have several advantages: the Q.E. is typically a factor of 3 higher than PMT (for a PMT the Q.E. does not exceed 20-30%) and since the thickness is less than 1mm and the weight is only few grams, they can be easily mounted in complex systems and can work in high magnetic fields.

However, APDs have a relatively small gain ( $\leq 10^4$ ), and a charge-sensitive amplifier is needed. It is worth noting that among semiconductor devices, only APDs have an internal gain. A detailed description of the charge-amplifier and the electronic read-out of the APDs is reported in Dussoni's Ph.D. thesis<sup>7</sup>.

## 4.2. APD characterization

It is known that close to the breakdown region, APDs can reach very good gain values, of the order of 1000; the aim is therefore to make them operate in this region. Considering that, both breakdown voltage and dark current are strongly influenced by the working temperature, an accurate characterization of the gain and noise of each device in the same conditions of the MEG experiment is necessary.

Figure 4.4 shows a scheme of the system that has been realized for the characterization and test of these devices. In order to simulate the light coming from the scintillating fiber, a pulsed laser with  $\lambda=408$  nm (model NDHV310ACA with AVTECH pulsing system) together with a photometer with a sensor sensitive to wavelengths in the range 190-1100 nm (NEWPORT, Mod 2930C) have been used. In this setup, it is possible to count with a good precision the number of photons hitting each APD and thus estimate the absolute gain. The temperature of the APD was controlled by a Peltier cell and a thermocouple PT 100 as a thermal sensor.



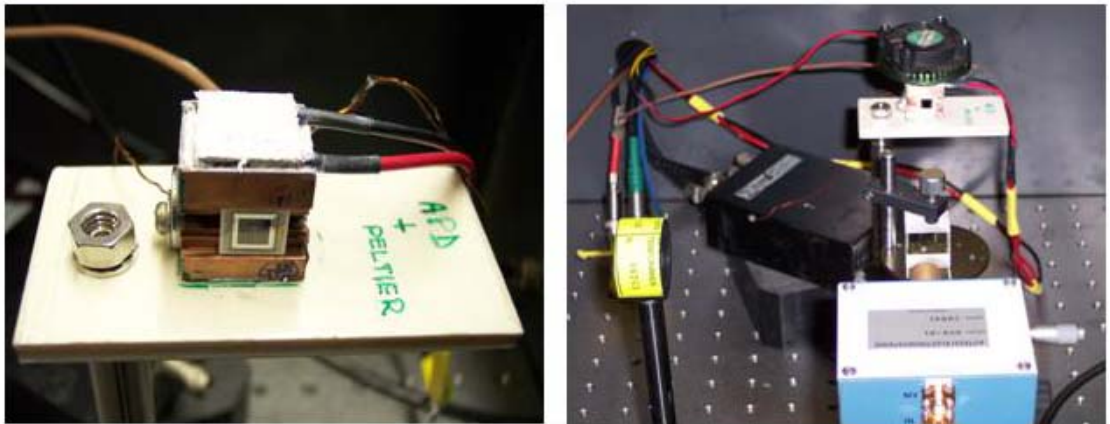


**Figure 4.4:** Scheme (top) and photos (bottom) of the testing system for the APDs characterization.

The APD is excited by a laser pulse of few nanoseconds and thermalized at different temperatures. The photometer and the phototubes are used to monitor the amplitude and the duration of the light pulse and to determine with accuracy the number of photons.

#### 4.2.1. Thermal dependence

The gain of the APD increases with decreasing temperature, due to the longer mean free path for elastic collisions with the lattice that lower temperature gives and therefore to the lower energy loss for the electrons. Consequently, at lower temperatures, electrons will gain more energy for an equal electric field and the ionization rate and gain increase.

In the APD, electron-hole pairs will be present, both produced by optical signals and released by thermal excitation. In general, in every semiconductor device, it is expected that thermal generation of electron-hole pairs decreases with decreasing temperature, as the probability  $p$  for excitation of an electron across the band gap  $\varepsilon$  varies as  $p = \exp\left(-\frac{\varepsilon}{kT}\right)$ . This decrease of thermal background is not immediately

obvious since the gain shows a fast increase with decreasing temperature, as mentioned above, and consequently the dark current rises as the temperature falls<sup>8</sup>. In fact, the APD dark current can be of two different natures: surface leakage current,  $I_s$ , that flows

through the interface between the PN junction and Si oxide layer, and bulk current,  $I_b$ , generated inside the Si substrate. The surface leak current is not multiplied since it does not flow in the avalanche region, while the bulk current does. In general, the total dark current can be expressed by  $I_D = I_s + M \cdot I_b$ .

In Figure 4.5 the dark current as a function of the bias voltage for an APD of the MEG experiment at five different temperatures is shown. It indicates that for a given bias, the dark current is much larger at the high temperature.

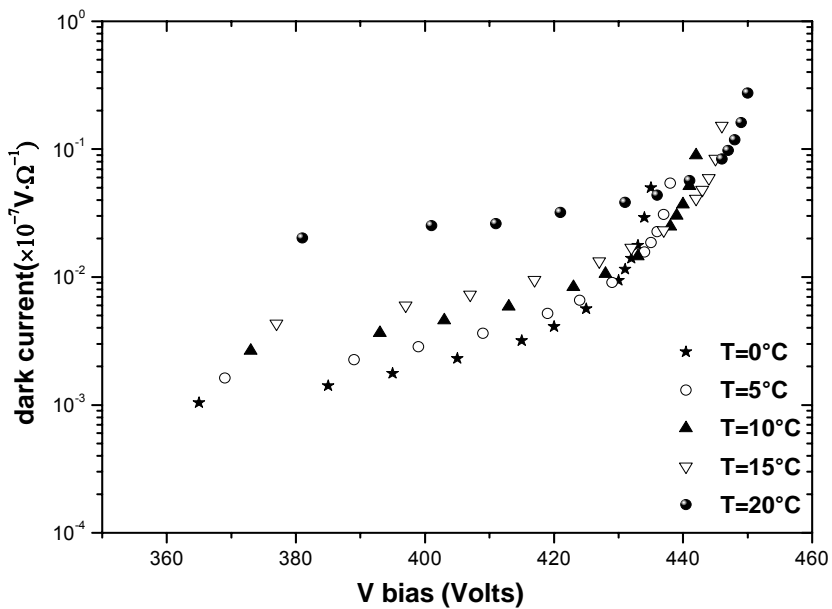


**Figure 4.5:** Dark current as a function of voltage bias at different temperatures. The current is measured across a  $10\text{ M}\Omega$  resistance in series with the APD.

On the contrary, observing the part of the figure near the breakdown voltage magnified in Figure 4.6(a), it is possible to see that, for a fixed bias voltage, the dark current is much larger for the lower temperature. This is due to the fact that the APD gain exponentially increases close to the breakdown region. Figure 4.6(b) shows that lowering the temperature the APD will breakdown at lower bias.

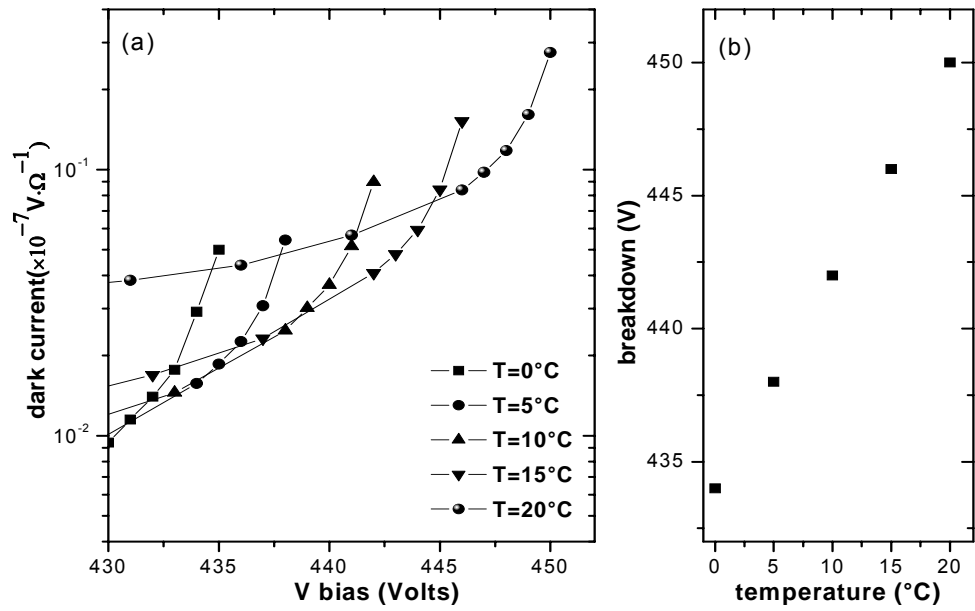


**Figure 4.6:** Dark current near the breakdown at different temperatures (a), breakdown voltage as a function of temperature (b).

Actually, considering voltages with the same gain at different temperature, it is clear that the number of thermal electrons decreases with decreasing temperature. This is a very important point, because the signal-thermal noise ratio is proportional to the number of electron-hole pairs, and it is not changed by the gain. Therefore detector signal can be improved by controlling the temperature and by keeping it as low as possible, compatibly with the working conditions of the experiment.

From Figure 4.6 (b) it is possible to calculate the temperature coefficient which indicates the change of the breakdown voltage as a function of the APD temperature. The fit shown in Figure 4.7 gives a value of  $0.80 \pm 0.03 \text{ V}/^\circ\text{C}$ , in agreement with the one reported by the manufacturer (see Table 4.3). This information is extremely important, because it will allow to estimate the breakdown in the final detector, also at temperatures different than the test one.

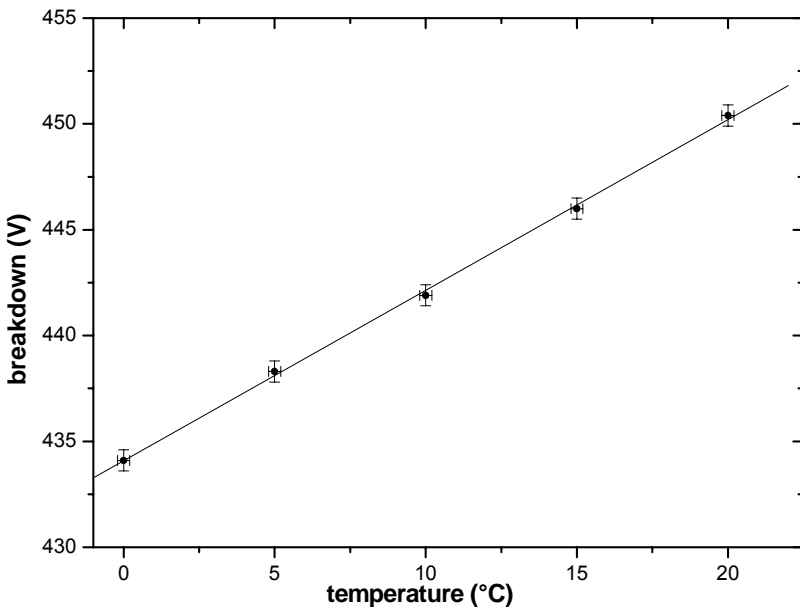


**Figure 4.7:** Breakdown voltages as a function of different temperatures (dots) and Linear fit (line).

#### 4.2.2. APD evaluation

To find a best compromise among APD performance and total cost, four batches coming from different productions have been compared. Table 4.2 summarizes the APDs arrived and tested since Fall 2003.

**Table 4.2:** Summary of the APD batches.

Batch number	Type	Date	Number of APDs
Batch # 1	Sample for evaluation test	Fall 2003	12
Batch # 2	Low cost CMS irradiated	2004	> 50
Batch # 3	Low cost CMS not irradiated	March 2005	1200
Batch # 4	Directly from Hamamatsu	2004–2005	2–20

The batch # 1 was the first evaluated; on the basis of the good result obtained with these samples, have been decided to pursue in the design of the fiber-APD detector. Later, two batches coming from the production for the CMS experiment,

irradiated (# 2) and not irradiated (# 3), have been tested. Finally a test on “virgin” APDs of a new production from Hamamatsu (# 4) has been carried out.

Figure 4.8 shows the dark current normalized to the gain as a function of the absolute gain for APDs coming from different batches. These measurements were done before the batch # 3 arrived.

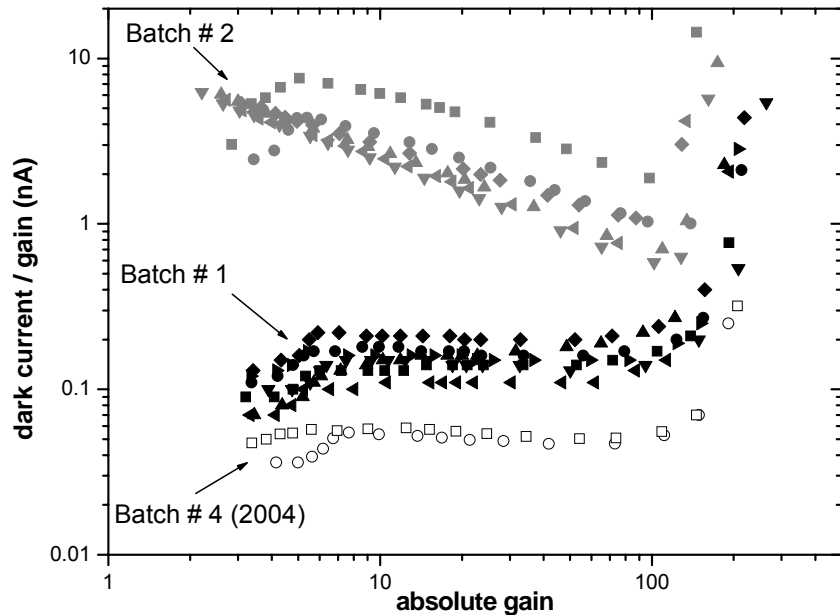


**Figure 4.8:** Dark current normalized to the gain as a function of the gain for batches #1,2 and 4.

Most of the work has been done to qualify batch # 3, which appeared to have similar behavior to # 1 and the best performance to cost ratio. The 1200 APDs received in March 2005 (# 3) have been tested to verify the dark noise characteristics, breakdown voltage and gain. The first APDs that have been tested are those coming from the same batch, i.e. those coming from the same silicon wafer, in order to verify whether their noise characteristics were the same reported by Hamamatsu and whether their breakdown voltage was similar. In this way, the uniformity of the behaviour could allow to test a small number of detectors. In Table 4.3 the main properties of the APDs employed in MEG experiment are summarized.

**Table 4.3:** Electrical and optical characteristics of APD S8664<sup>II</sup>.

Spectral response (nm)	320-1000
Peak sensitivity (nm)	600
Quantum efficiency @ 420 nm (%)	70
Temperature coefficient of V <sub>BD</sub> (V/°C)	0.78
Dark current typical-max (nA)	5-50
Cut off frequency (MHz)	40

Unfortunately, the first tests carried out on the APDs did not give the expected results. Indeed, comparing the behaviour of APDs provided directly from Hamamatsu and received from PSI for MEG experiment, the necessity to test all the photodiodes to be mounted in the final detector appeared evident. Two different factors contribute to this problem: first, the photodiodes provided by PSI are not easily divided in groups, because they come from different batches and therefore have different properties. Moreover, as shown in Figure 4.9 (a), the dark current behaviour is not a-priori reproducible. In the figure, the straight line indicates the maximum dark current limit obtained for APDs from Hamamastu (full symbol, panel b), which is about 50 nA. As it can be observed, the APDs provided by PSI (open symbol, panel a) often exceed this threshold.

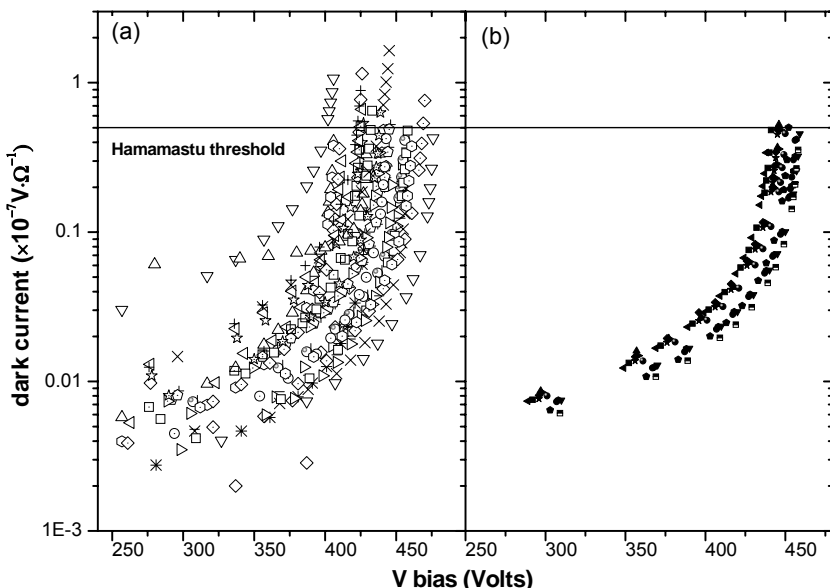


**Figure 4.9:** Dark current as a function of voltage for APDs from Hamamatsu batch # 4 (full symbols) and a selection of batch # 3 (open symbols). The solid line shows the maximum dark current given by the manufacturer.

Therefore, a selection both in terms of breakdown voltage and mostly in terms of dark current became necessary. To characterize a so large number of APDs, a LabVIEW program for the measurement control has been realized.

#### 4.2.3. Dark current and gain measurements

For the measurement of the breakdown voltage,  $V_{BD}$ , a  $10 \text{ M}\Omega$  resistance in series with the APD, has been used. In this way, the voltage  $V_R$  across the resistance can be measured by a digital multimeter and a voltage source providing a voltage  $V_{HV}$ , both controlled by a computer through GPIB interface. Starting from a fixed voltage of 360 V,  $V_{HV}$  is increased by 5V steps while the program reads  $V_R$ . The measurement goes on until  $V_R$  exceeds the critical value of 2 V, corresponding to a dark current of 200 nA; then, the program gives  $V_{BD} = V_{HV} - V_R$  as an output. The experimental values show a 1% agreement with those given by the manufacturer. Once the breakdown is calculated, the program starts to measure the dark current from  $V_{BD} - 1 \text{ V}$  for a given number of voltage steps which can be set a priori.

Figure 4.4 shows the scheme for the measurement of APDs absolute gain. The first tests have been carried out by using a laser with a wavelength  $\lambda=780 \text{ nm}$ . Then a laser with  $\lambda=408 \text{ nm}$  has been bought, in order to reproduce the wavelength of the light produced by the scintillating fibers, which has a peak at 492 nm. It is worth noting that the variation of the output signal is related to the incident wavelength<sup>9</sup>, and thus has an influence also on the measurement of the absolute gain. Figure 4.10 shows the gain as a function of wavelengths of the incident light. The data are referred to the same APD. It can be observed that for  $\lambda=780 \text{ nm}$  the maximum gain is about 200, while for  $\lambda=492 \text{ nm}$  it exceeds 550. This result is in good agreement with the expected values.

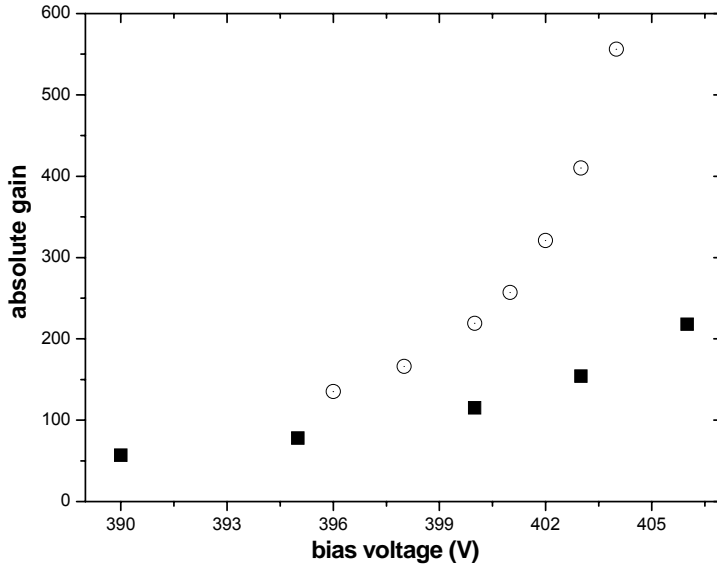


**Figure 4.10:** Wavelength dependence of APD gain at 408 nm (square) and 780 nm (circle).

The signal coming from the laser is split and read at one side by a photometer, (NEWPORT mod. 2930C with a UV-818 head sensor)<sup>10</sup> which has an uncertainty of 2% in the range 200-1100 nm, positioned at the same distance than the APD to be measured. As already recalled, the APD is thermalized at  $20 \pm 0.3$  °C. The signal from the APD is amplified by a charge preamplifier (SILENA 205), with a gain of 450 V/pC, and then sent to a digital oscilloscope (Tektronix mod. TDS 3054). Also in this case, the acquisition is made through a LabVIEW program, which uses the same voltage values employed for the dark current measurement. In Figure 4.10 the point at the highest voltage, given by  $V_{BD} - 1$  V, is not the same for the two curves; this is due to the fact that in the first case, for  $\lambda=780$  nm, the system for the temperature control was not used yet.

The laser is excited by a 2 KHz pulse generator (AVTECH) with a 200 ps rise time and a 4 ns pulse width. The laser output signal, about 12  $\mu$ W, is attenuated by a factor 600 before reaching the APD: in fact, it has been experimentally observed that the photodiode becomes non-linear when the light power exceeds  $\sim 70$  pW (see ref. [7]).

The used setup allows to evaluate precisely the number of photons reaching the APD,  $n_{inc}$ , and so to calculate the detector absolute gain,  $G$ . Known the output voltage,  $V_{out}$ , it is possible to obtain the number of produced electrons,  $n_p$ , by

$n_p = \frac{V_{out}}{450mV/pC} \cdot \frac{1}{1.6 \cdot 10^{-19}}$  and thus the gain  $G = \frac{n_p}{n_{inc}}$ , considering a quantum efficiency of ~70 % at 408 nm, as shown in Figure 4.3 .

### 4.3. Fibers characterization

Scintillating fibers represent an extremely important and delicate part of the detector. In fact, besides providing the trigger signal for the timing counter, they allow an accurate reconstruction of impact point of the positron. As previously mentioned, at the first trigger level, a rough information on the position is provided by the logic sum of 18 adjacent scintillating fibers, whereas the scintillator bars give the time coincidence LXe–TC in a range 10–20 ns. In a second phase, the triggering sub-detector acquisition system will provide information on which and how many fibers were hit, reducing the spatial resolution down to ~1cm. This value can be evinced from MC simulations, observing the average number of hit fibers per event (see Figure 4.12 (right)).

In order to fit the scintillating fibers into the magnet shape, they have to be bended with an average curvature radius of 288.9 mm. Figure 4.11 shows the ending part of the fibers in the triggering sub-detector. Considering that the space occupied by an APD is  $10.6 \times 9.0 \text{ mm}^2$  the fibers were split at the end to allow the coupling between them with a separation of 1 mm.

To do that, the fibers will be shaped in two different ways in the ending part, but keeping the same shape in the central part. As a consequence, there will be a difference (b–a) in the total length of the fibers of ~ 22 cm, as schematically shown in Figure 4.11.

It is therefore important that the light collected inside the fiber arrives to the APDs with the minimum efficiency loss. From Monte Carlo simulations, it was possible to calculate the amount of energy released and the average number of crossed fibers. Figure 4.12 shows that the energy released by the positrons inside the fiber is  $\geq 1 \text{ MeV}$ , and that they cross on average two fibers.

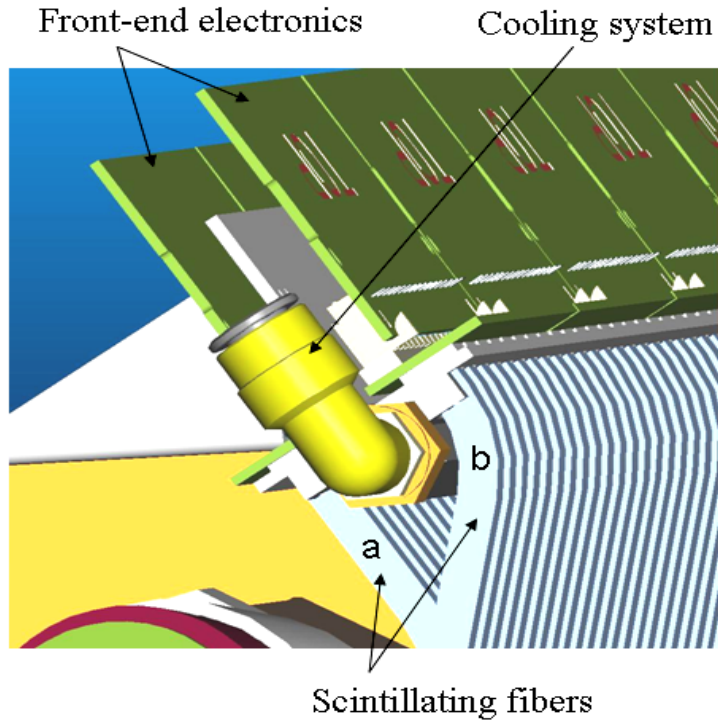


**Figure 4.11:** Layout of the scintillating fiber's ending part.

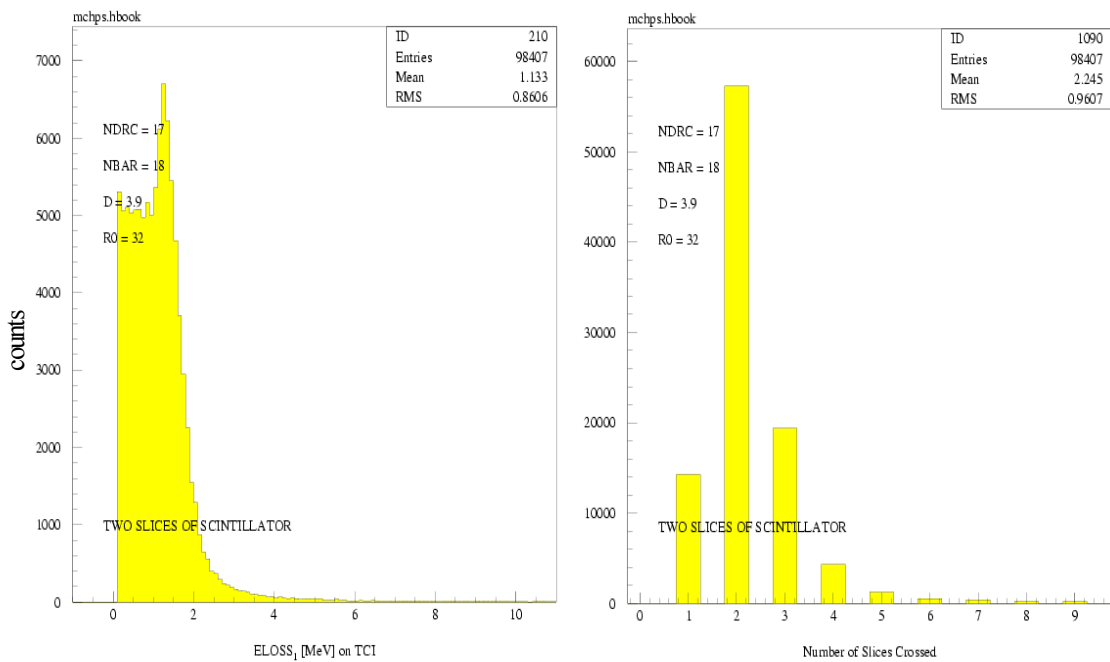


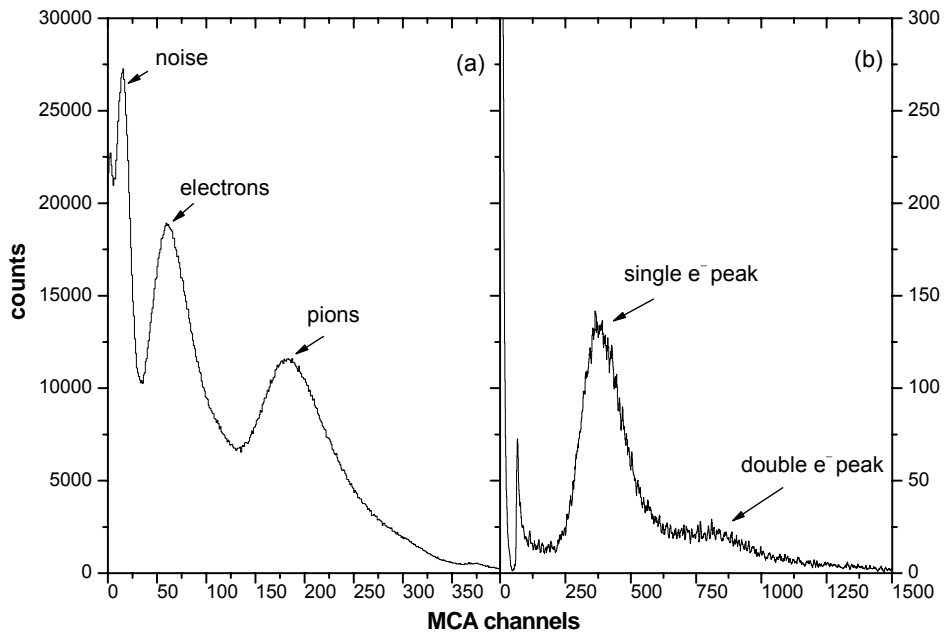
**Figure 4.12:** Monte Carlo simulation on the count rate response as a function of: the energy loss (left) and of the number of crossed fibers (right)<sup>11</sup>.

### **4.3.1. Light propagation measurements**

Among the measurements carried out on scintillating fibers, one of the most important is the estimation of the light attenuation length. The original idea of reading the light from a scintillating fiber with an APD has been tested at the PSI and LNF beam facilities. In the beam tests pieces of fibers were coupled with APDs. The main aim of these tests was the investigation of the overall signal to noise properties of the fiber-APD assembly. The problems addressed in these test were:

1. photon yield at the fiber output enough high for an APD readout;
2. APD gain and noise in operating conditions;
3. Signal to noise ratio high enough to fire a discriminator for simple 1/0 output when the fiber is crossed/not crossed by a particle. It is worth noting that the electronic readout is switched on only if both APDs of the same fiber receive enough photons to turn on the discriminators.

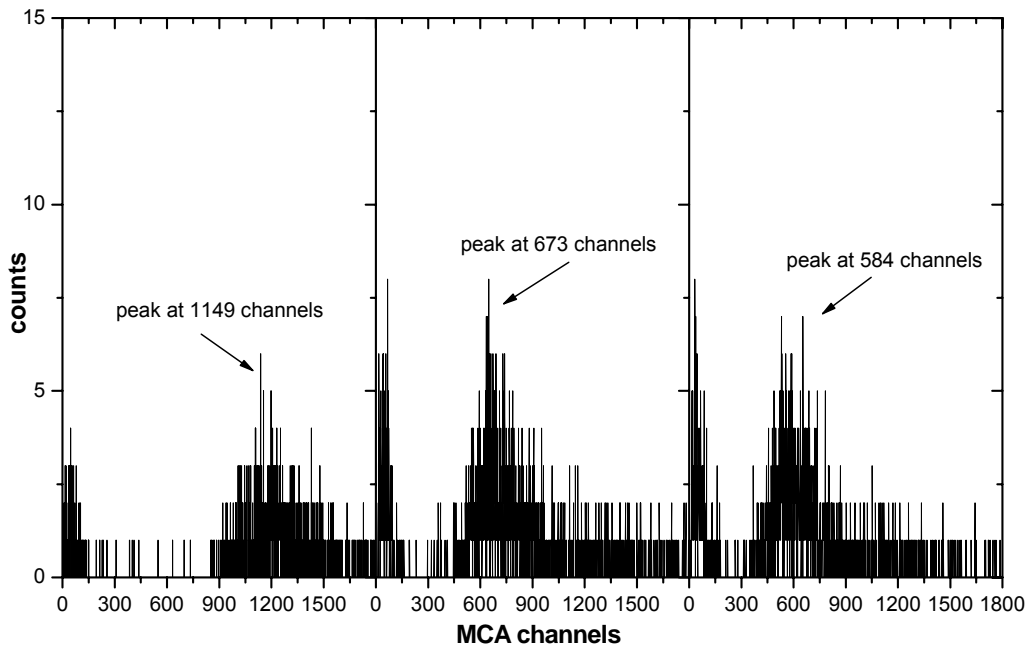
Furthermore, being the attenuation length given by the manufacturer  $> 350 \text{ cm}^{\dagger}$  and considering that for the final length of the fiber of  $\sim 90 \text{ cm}$ , it has been predicted a maximum signal reduction of 12%, for the final detector. In Figure 4.13 (a), the spectrum obtained from a 5 cm scintillator fiber coupled with an APD acquired during the PSI tests is reported. The two peaks referred to electrons and pions, coming from the  $\pi E1$  beam line, are well visible. The Figure 4.13 (b) shows the charge spectrum made at the BTF (LNF) beam test, where a single a double electron peak are clearly extracted. The results show a good signal to noise ratio that was dependent only on the APD quality. It has been concluded that with good APD, i.e. APD with characteristics similar to the Hamamatsu nominal parameters (batch # 4), the detectors was assumed to work as wanted.



**Figure 4.13:** Spectrum obtained with  $e^- - \pi$  beam at PSI (a) and with  $e^-$  at LNF (b).

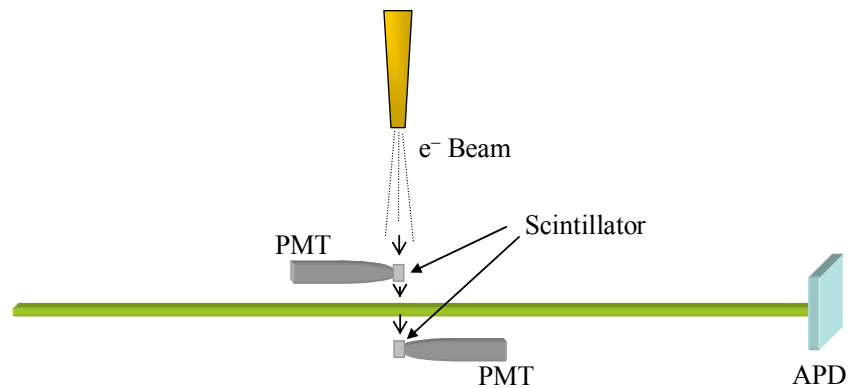
Most of the efforts were addressed to select APD with parameter in the useful range: the selection, as mentioned before, was made over 1200 samples. Only at the end of this job we were ready to test final prototypes.

Some problems appeared in the last BTF tests (January 2006), where the fibers of the final length and shape were used. In this case, the signal-noise ratio was lower than the expected and strongly dependent from the position at which the beam hit the fiber. This unexpected position dependence seems to be attributed to an effective attenuation length shorter than the one declared by the producer.



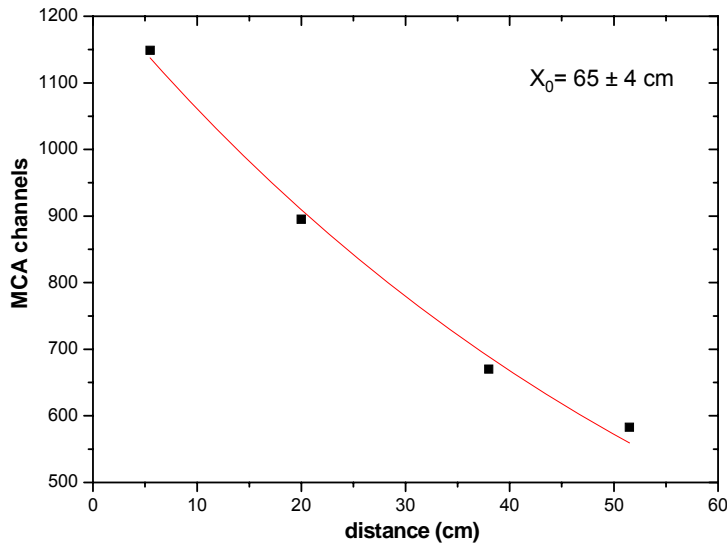
**Figure 4.14:** Spectra obtained using 90 cm scintillating fiber coupled with APD at LNF.

Figure 4.14 shows three spectra obtained during the tests at the BTF with a 103 cm long scintillating fiber, coupled with one of the APDs previously characterized. For each graph, the peak shift (1149, 673 and 584) is related to the shift of the impact point of the electron beam. The corresponding distances are 5.5, 38.0 e 51.5 cm respectively. These values represent the distance between the detector (APD) and the impact point of the electron beam. By means of a system for the geometrical selection of the beam, it was possible to reduce the uncertainty on the impact point on the fiber in order to be sure that it was completely crossed, as shown in Figure 4.15.



**Figure 4.15:** Sketch of the experimental setup for the measurements with fibers at BTF (LNF).

These measurements led to an attenuation length for the scintillating fibers of  $(65 \pm 4)$  cm.



**Figure 4.16:** Measurement of the attenuation length using the data from the BTF tests (dots) and exponential fit (line).

For this reasons it has been decided to estimate the attenuation length as reported by the producer. For this measurements, a  $^{90}\text{Sr}$  radioactive source with an activity of  $2.7 \cdot 10^6$  Bq has been used. Strontium shows a  $\beta^-$  decay in  $^{90}\text{Y}$ , which also decays  $\beta^-$  with an average lifetime of 64.1 h and an end-point energy of 2.28 MeV<sup>[12]</sup>. In these conditions, the released energy inside the fiber is comparable to that observed in MC simulations. In Figure 4.17, the experimental setup for these measurements is shown.

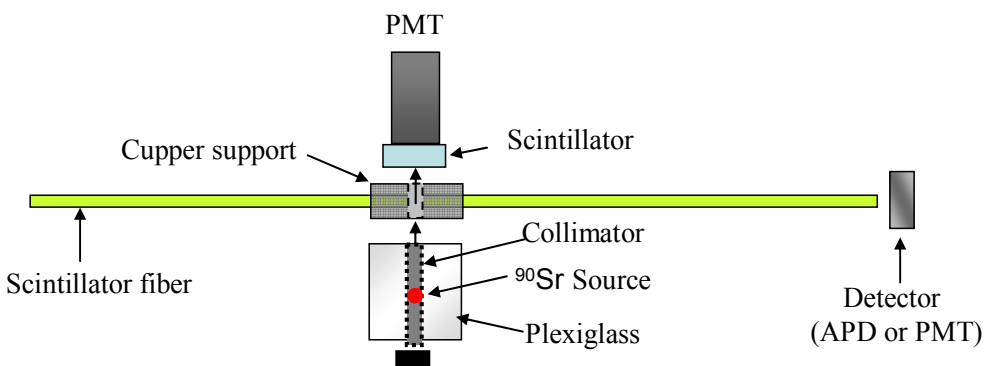


**Figure 4.17:** Experimental setup for the attenuation length measurements.

The  $^{90}\text{Sr}$  source is glued at one side of a thin plexiglass cylinder (0.3 cm  $\varnothing$ ), positioned inside a hollow plexiglass cylinder (5 cm  $\varnothing$ ). The source can be therefore

moved inside it, so that the electron rate on the fiber can be changed and the electron beam can be focused on the fiber itself; the range of 2.5 MeV electrons inside the plexiglass is in fact  $\sim 1$  cm. On the opposite side of the fiber, a small block of BC422 plastic scintillator coupled with a PMT (Hamamatsu mod. H3167) is positioned. When the scintillator is excited by an electron, the phototube provides a gate-signal to the multi-channel analyzer (MCA) acquisition system, meaning that the particle has crossed the 5 mm of the fiber. Now, the signal coming from the APD which is placed at one of the two fiber sides, is acquired. Figure 4.18 (a) shows the results on the attenuation length obtained using an APD of the MEG experiment. To be more confident on the experimental data, the measurement has been repeated with a 1" PMT instead of the APD, as shown in Figure 4.18 (b), reproducing the same test made by the manufacturer. Figure 4.19 shows the attenuation length given by the manufacturer for scintillating fibers of various diameters.

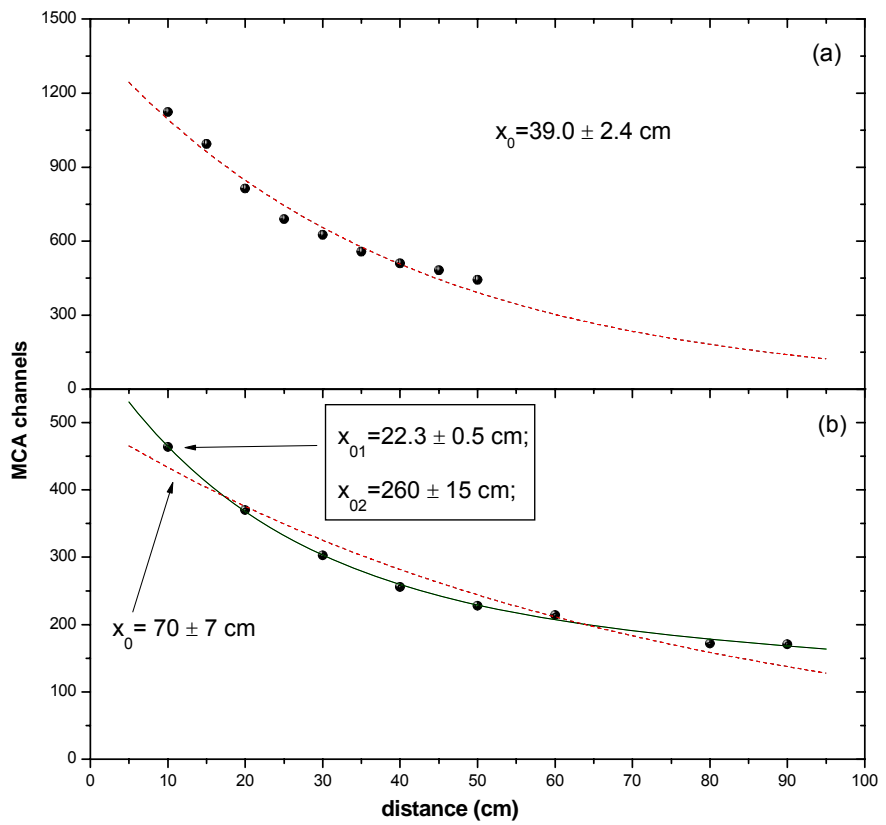


**Figure 4.18:** Measurements of the attenuation length using a PMT (b) and an APD (a) as detector. Points and dashed lines represent the experimental data and the single exponential fit respectively. Solid line represents the double exponential fit.

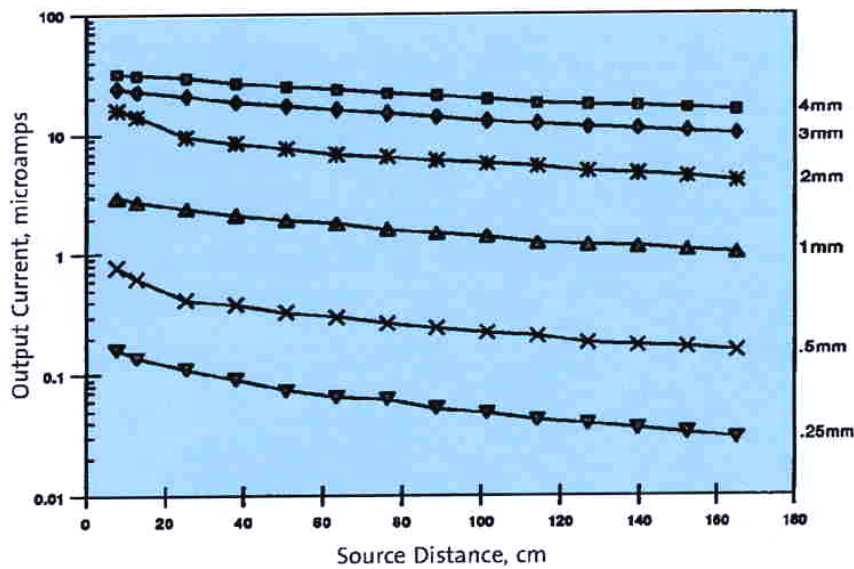


**Figure 4.19:** Attenuation length for different scintillating fibers diameters measured by Bicron with  $^{90}\text{Sr}$  source.

### 4.3.2. Emission spectrum measurements

To understand the origin of higher attenuation length, a more careful analysis of the properties of scintillating fibers became necessary, to verify whether the reduced attenuation length was caused by defects in the physical properties of the plastic scintillator BCF20 influencing the emission and absorption band. Therefore, it has been decided to measure the emission spectrum of some fibers; in Figure 4.20 the emission spectra for different types of scintillating fibers given by the producer have been reported.

For this measurement, a UV lamp<sup>13</sup> with  $\lambda = 365$  nm as indicated by the producer, and a monochromator (MonoSpec mod. 82-477) with a spectral range between 190 nm and 40  $\mu\text{m}$  have been used to excite the fiber. The light signal coming out from the monochromator was detected by a phototube (Thorn mod. 9798 B) with spectral response in the range 300–800 nm.

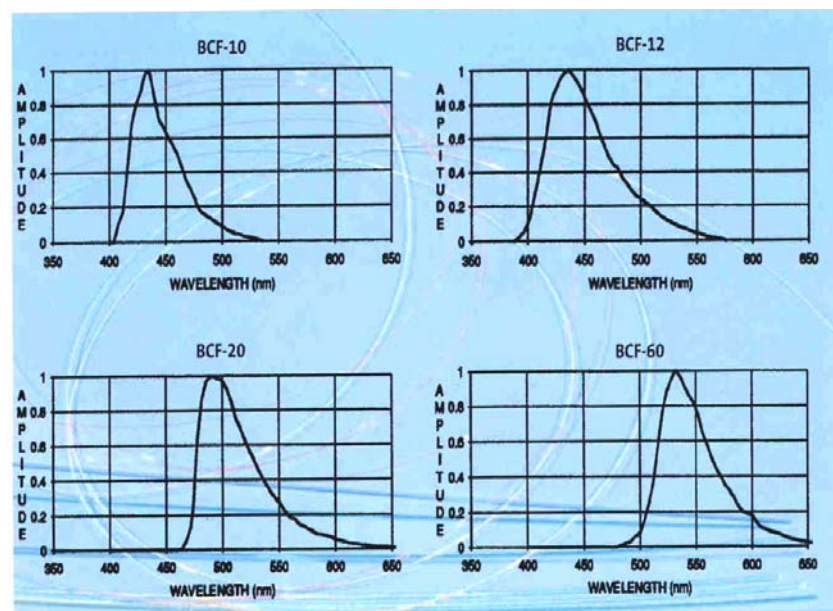


**Figure 4.20:** Emission spectra for different scintillation fibers from Bicron<sup>II</sup>: BCF10, BCF12, BCF20 (used in MEG experiment) and BCF60.

A LabVIEW program allowed both to control a step motor which changes the inclination of the lenses inside the monochromator and to read the signal of the PMT through a voltmeter.

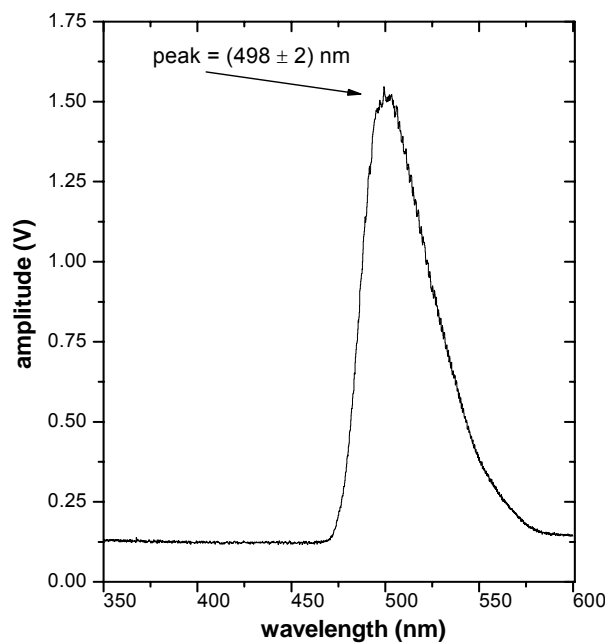


**Figure 4.21:** Spectral response for BCF 20 scintillating fiber.

Figure 4.21 shows the measured spectrum, which is in good agreement with that from the manufacturer reported in Figure 4.20.

### 4.3.3. Remarks on cladding properties

The fits relative to the attenuation length measurements were performed using the single and double exponential decay laws as:

$$y = A_0 e^{(-x/x_0)}, \quad y = A_{01} e^{(-x/x_{01})} + A_{02} e^{(-x/x_{02})}$$

It has been demonstrated<sup>14</sup> that, for fibers with a single cladding, there are two components contributing to the light: “core” light and “cladding” light. The first consists of those rays that are totally internally reflected at the core-cladding interface. The latter is the light which is totally reflected at the cladding-air interface. The attenuation properties of these two components are different and must be taken into account. In fact, the “core” light has an attenuation length that is determined by the absorption in the bulk and by the effective reflection coefficient at this interface. In Chapter 3 the importance of this last parameter has already been described. Although small imperfection could be present, reducing the reflection coefficient, the core-cladding interface is usually well controlled so that this coefficient should be very close to unity. In this way, a long attenuation length is possible in this case. The “cladding” light, instead, consists of rays which are beyond the angle of total internal reflection at the core-cladding interface but that can be trapped at the cladding-air interface. Since the quality of this interface is hard to be controlled, the reflection coefficient and, as a consequence, also attenuation properties worsen.

In case of double-cladding fibers, as those that will be used in the MEG experiment, there are three different interfaces and so it should be possible to observe three different attenuation lengths. To do that, specific test to observe the different light component, along with the use of fibers longer than 1 m, will be needed.

In Figure 4.18 the single exponential fits are shown as dashed lines. In case of Figure 4.18 (a), where only points up to 50 cm are available, a single exponential decay function fits quite well the experimental data.

In Figure 4.18 (b) instead, data up to 1 meter allows to better evidence the attenuation length behaviour. A comparison between single (dashed line) and double (solid line) exponential fits is shown in the graph. It can be observed that, differently from Figure 4.18 (a), the single exponential fit does not well reproduce the experimental data. On the contrary a double exponential fit accounts for the measured points

behaviour, showing that two different attenuation lengths are present, as previously described. One of them is more than 2.5 meter, closer to that provided by the manufacturer; the other one is about 20 cm. It is worth noting that the producer gives only one value ( $>3.5\text{m}$ ), neglecting the influence of the different light components at different distances. Therefore, at distances of 40-50 cm, typical of the MEG experiment, the light is influenced by the shortest attenuation length, with a signal reduction of more than 50%. This effect is mainly due to losses at the outer cladding.

The recent tests carried out on fibers evidenced an attenuation length different from that indicated by the manufacturer. At present, possible solutions to enhance the light collected inside the scintillating fibers are under study, as:

1. to collect the signal coming from two adjacent scintillating fibers and send it to a single APD. In this way, the amount of collected light would be doubled, without any loss of spatial resolution, as shown in paragraph 4.3. The final project wouldn't be substantially modified, a part from a reduction of the number of APDs and therefore of the acquisition channels.
2. the use of high reflectivity materials, i.e. Kodak White Reflectance Coating with a reflectance of 0.992 at 500 nm wavelength<sup>15</sup>, to coat the fiber surface. This solution will be tested soon.
3. to use optical fibers in the ending part of the detector, to reduce the light losses due to the curvature of the fibers. In Figure 4.22, the joint between scintillating fiber and optical fiber is shown.

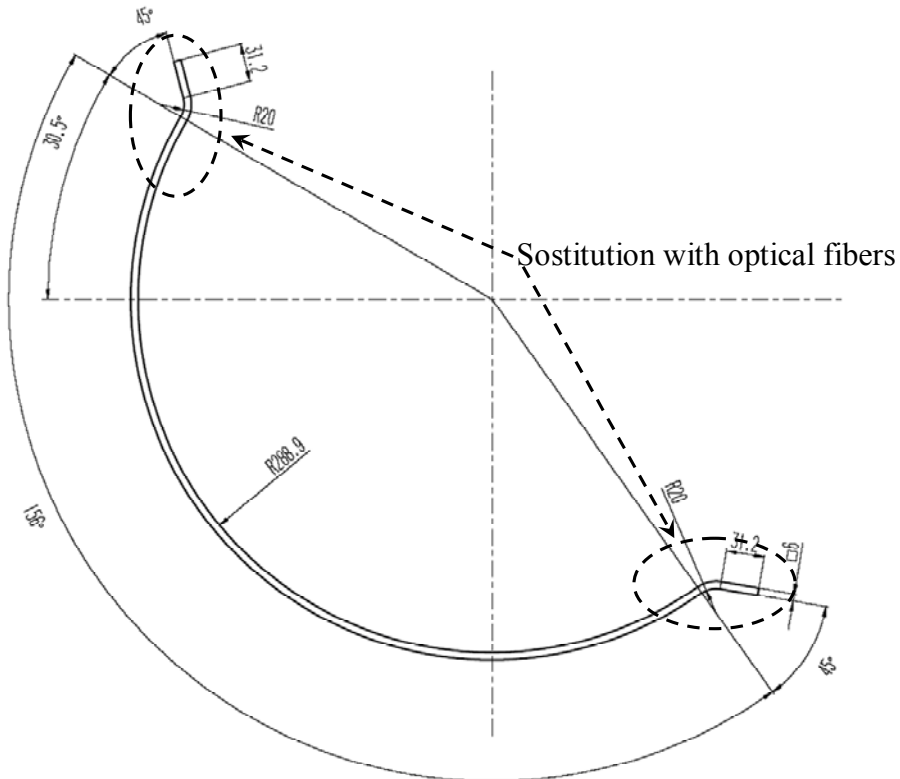


**Figure 4.22:** Layout of scintillating fiber, where the potential modifications to the initial project are indicated.

In conclusion, most of the problems occurred during the tests on fibers can be ascribed to the attenuation length properties. A BC404 scintillating fiber of almost the same dimensions of the fibers used up to now ( $5 \times 5 \times 90 \text{ cm}^3$ ) will be realized in Genova soon. The machining and polishing procedure will be the same described in Chapter 3. In this case, due to the absence of cladding, only one attenuation length should be observed.

#### 4.3.4. Summary of the scintillating fiber measurements

The results of all the measurements carried out on BCF20 scintillating fibers are summarized in Table 4.4, along with the corresponding values given by the manufacturer, when available. In the following, the experimental procedures to obtain these results are briefly described, avoiding those already discussed in previous paragraphs.

**Table 4.4:** Summary of the measurements on fibers, compared with the data provided by the producer.

	<b>Expected<sup>*</sup></b>	<b>Measured</b>
Emission spectrum peak	492 nm	$498.5 \pm 2.0$ nm
Attenuation length	$> 3.5$ m	$X_1 = 22.3 \pm 2.3$ cm $X_2 = 260 \pm 15$ cm
Cladding-core ratio		
$R = \frac{L.(cladding - air)}{L.core}$	1.37	$1.44 \pm 0.18$
Trapping efficiency without EMA	7.3%	$6.6 \pm 0.5$ %
Trapping efficiency with EMA	Not available	$5.7 \pm 0.4$ %
Light efficiency loss – final design	Not available	$26 \pm 2$ %
Efficiency loss – annealing process 120°C	Not available	Below instruments sensitivity

\* Given by the producer.

The measured ratio between “cladding” and “core” light is approximately 1.44. This value has been obtained by using the weight coefficients  $A_{01}$  and  $A_{02}$  given by the double exponential fit described in paragraph 4.3.3. The expected value instead is the ratio between the amount of light trapped at the cladding-air interface and in the core, as shown by:

$$R = \frac{\int_{90-\theta_{lim1}}^{90-\theta_{lim2}} \sin \theta d\theta}{\int_0^{90-\theta_{lim1}} \sin \theta d\theta};$$

where  $\theta_{lim1} = \arcsin(1.49/1.6) = 69^\circ$  is the critical angle at the core-cladding interface and  $\theta_{lim2} = \arcsin(1/1.6) = 39^\circ$  is the angle in the core for light trapped at the cladding-air interface. The experimental and expected values are in good agreement.

The trapping efficiency was measured on ~10 cm long pieces of straight fibers, by making the ratio between the incident light and the light coming out from the fiber itself. A similar procedure has been used to measure the light loss due to the fiber curvature as shown in Figure 4.22. A teflon covered steel mould is used to shape the fibers. The straight fiber is heated up to 120 °C for 5 minutes, bended in two steps and

finally cooled down in about half an hour. Figure 4.23 shows a bended fiber in the final design.

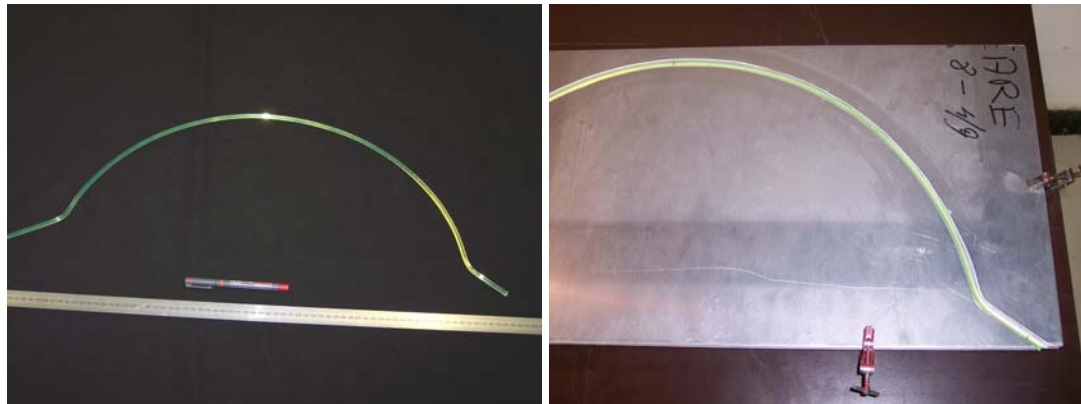


**Figure 4.23:** Test for the bending of scintillating fibers.

## Bibliography Chapter 4

- 
- <sup>1</sup> A. Baldini, R&D proposal to INFN, “The MEG experiment: search for the  $\mu^+ \rightarrow e^+ + \gamma$  decay at PSI”, September 2002.
  - <sup>2</sup> Saint-Gobain Crystal, [www.detectors.saint-gobain.com](http://www.detectors.saint-gobain.com).
  - <sup>3</sup> W. R. Binns et al., NIM 216 (1983) 475.
  - <sup>4</sup> R. Farrell et al., NIM A 387 (1997) 194.
  - <sup>5</sup> K. Deiters et al., NIM A 442 (2000) 193.
  - <sup>6</sup> Hamamatsu Photonics, [www.hamamatsu.it](http://www.hamamatsu.it).
  - <sup>7</sup> S. Dussoni, MEG collaboration, Ph.D. Thesis, “Search for Lepton Flavour Violation: The MEG experiment”, May 2006.
  - <sup>8</sup> I. Tapan et al., NIM A 388 (1997) 79.
  - <sup>9</sup> T. Kirn et al., NIM a 387 (1997) 202.
  - <sup>10</sup> <http://www.newport.com/>.
  - <sup>11</sup> <ftp://megftp@pc-grid-alex.roma1.infn.it/>.
  - <sup>12</sup> Table of Isotopes, E. Browne et al., Edited by C. M. Lederer and V. S. Shirley, 7<sup>th</sup> Edition, 1978.
  - <sup>13</sup> <http://www.spectroline.com/>.
  - <sup>14</sup> N.A. Amos et al., NIM A 297 (1990) 396.
  - <sup>15</sup> <http://www.kodak.com/>.

## *Chapter 5*

# **Preparation of $\alpha$ -source on wire and target for (p, $\gamma$ ) energy calibration of LXe detector**

In the MEG experiment, the data collection will last for about two years. The calibration and the monitoring of the whole MEG detector is necessary in order to ensure that the required performance (energy, time and space resolutions) are maintained over the full life of the experiment. The MEG collaboration decided to use several complementary and redundant methods to calibrate and monitor the working parameters of all detectors<sup>1</sup>.

During my PhD thesis I have contributed to the study of new methods for monitoring the light yield and for calibrating the energy scale of the LXe calorimeter.

As described in Chapter 2, the LXe purity is a key issue for this detector. Tiny amount of light absorbing impurities could reduce the light yield and the transparency of the LXe, causing unpredictable worsening of energy resolution and variation of the energy scale.<sup>1</sup>.

In this Appendix will be described the preparation of special calibration source to be used for monitoring the yield and absorption length of the liquid Xenon, and of targets to be used for energy scale calibration by mean of protons for exciting gamma lines.

First I describe the preparation of calibration sources that make use of small  $^{210}\text{Po}$  alpha-sources onto thin wire that has been tested in the LXe Large Prototype. Later I will move on the description of the method of production of lithium (Li) and

boron (B) targets, which have been tested at Van de Graaf accelerator (VDG-AN2000) at National Laboratory of Legnaro (LNL). Similar targets should be used in the 1 MeV Crockroft-Walton (CW) accelerator that will be integrate into the MEG experiment.

## 5.1. Radioactive wire-sources

One of the methods to monitor liquid scintillator calorimeters consists on a set of thin wires, on which are deposited alpha-sources in selected positions. The choice of alpha-sources is made based on several reasons: good reference for the energy calibration, due to their almost monochromatic emission line; being point-like sources, they provide a good setup geometry calibration, i.e. the cross-calibration of phototubes. The conversion point of  $\gamma$ -source is not known a priori, while the alpha-source has a well characteristic range and thus it can be reconstructed in the expected positions: the range of alpha source in LXe is 40  $\mu\text{m}$  and in gas is 7 mm. It is, therefore, possible to verify experimentally whether the Monte Carlo simulation correctly reproduces the solid angles, reflections and measure directly the attenuation length of Xenon.

A series of wires (thickness 50  $\mu\text{m}$ ) with the aim to test the effectiveness of the calibration method, have been produced. The sources have built by electroplating two wire portions, whose length is less than 1 mm, at a distance of 124 mm each from the other. In order to assure a successful electro-plating process we have chosen to work with  $^{210}\text{Po}$ . Special care has been done in avoiding any unwanted contamination of the wire. Therefore the wire has been covered by photoresist, except on the points where the source was deposited. After the electroplating process in a solution of  $\text{PoCl}_4$ , the resist has been removed with acetone, as in standard photolithography techniques. Four wires have been prepared, with two alpha-sources for each. Two of the sources had an activity of 100 Bq, while the other two 30 Bq. In Figure 5.1 is displayed the activity of the alpha-sources measured using a PIN diode, with an active area of  $10 \text{ mm}^2$ , in front of the wire. The spectra were acquired with a traditional acquisition system composed of a preamplifier, a shaping amplifier and a multi-channel analyzer, MCA. From the spectrum, it is possible to see a tail at lower energies.

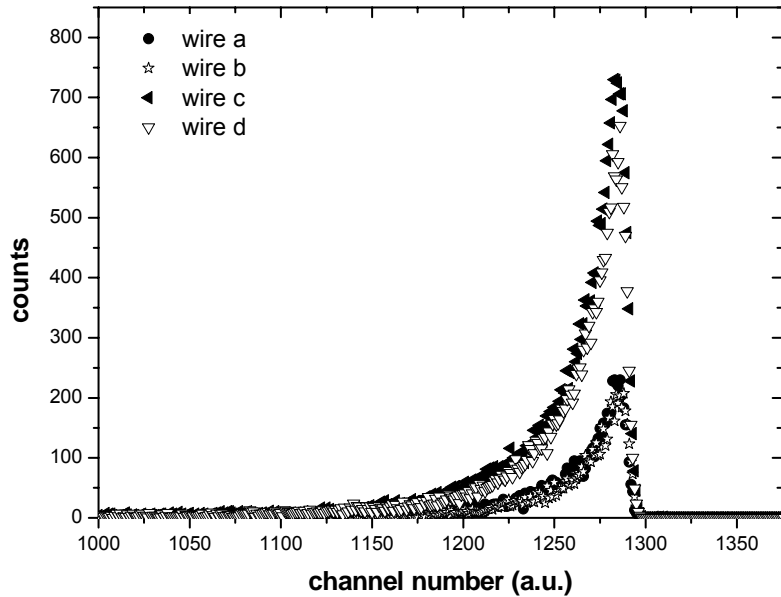


**Figure 5.1:** Activity spectrum of the four alpha-sources. The (c) and (d) wires show an activity of about three times with respect to (a) and (b) sources.

The wires were mounted in the Large Prototype and tested in Xe gas and LXe as shown in Figure 5.2. The results demonstrate that the original idea was correct. The reconstruction of the alpha- events position revealed an unexpected loop structure around the wire with a reconstructed radius much greater than the wire diameter.

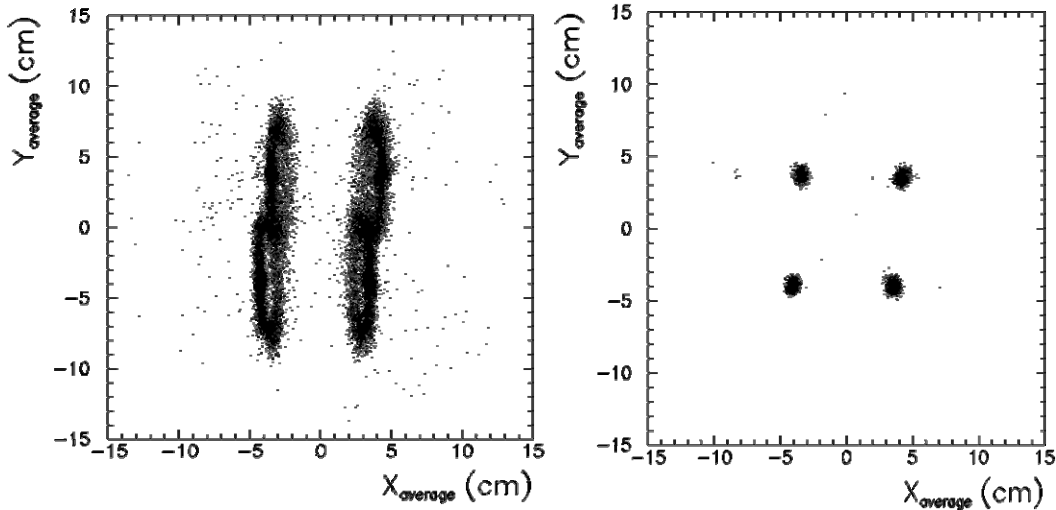


**Figure 5.2:** Difference between liquid (left) and gaseous (right) Xenon determined by alpha range<sup>2</sup>.

This has been explained as shift of the reconstructed barycentre of the light emission caused by the combined effect of the wire shadow and of the light diffusion. It

has been demonstrated that the reconstructed radius is dependent on the absorption length, and therefore can be used as monitor of this important parameters.

Unfortunately, Po is only good for preliminary tests, but not for the whole experiment due to its short lifetime of 138 d. The sources must have a stable intensity for several years after their installation in the MEG calorimeter<sup>3</sup>. The best possible radioisotope seems to be <sup>241</sup>Am, which has a lifetime of 432.2 years<sup>4</sup>. The production of a stable and safe <sup>241</sup>Am wire-source required a systematic program of R&D<sup>5</sup>. The sources have been produced by SORAD Ltd; currently Isotope Products Cesio. After production, the alpha-sources were tested for mechanically stress at cryogenic temperatures, since the commercial sources are tested only for  $T \geq -40$  °C, and leakage of radioactive isotopes into LXe. The <sup>241</sup>Am wire sources were tested at the ENEA-Casaccia Laboratory<sup>6</sup>. An immersion of ~1h, in liquid nitrogen,  $T = 77$  K, did not indicate any source leakage, at a minimum detectable activity level of ~0.01 Bq. In Figure 5.3 is shown an alpha-source wire, which has been mounted in the large prototype detector.

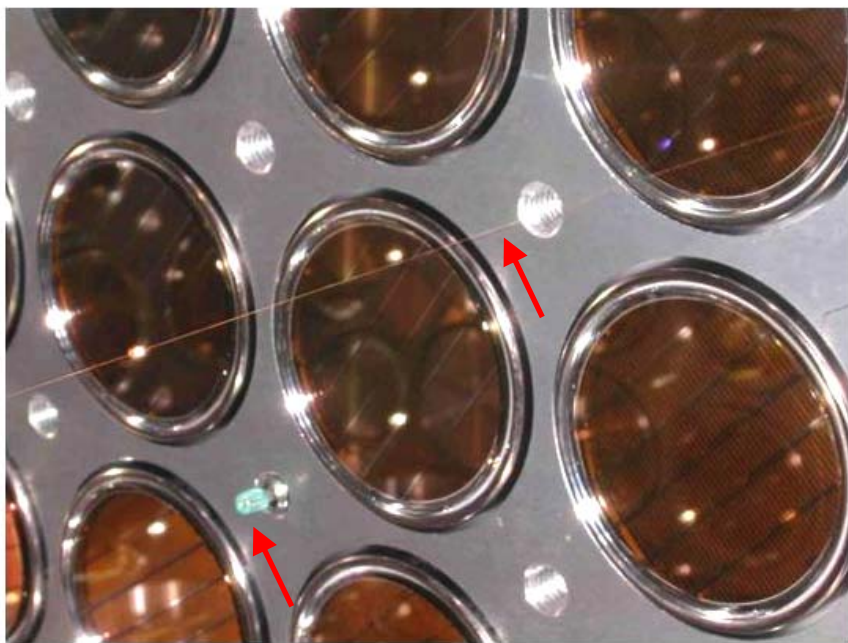


**Figure 5.3:** Picture of a two-source wire mounted in the large prototype detector, indicated with an arrow; and a LED marked with an arrow.

The calibration technique based on the radioactive point-sources, that have been developed and used for the first time in large prototype LXe detector, is particularly

valuable for liquid detector (liquid scintillator detector or cryogenic noble gas) in which the radioactive sources can be positioned within the scintillator material. In the MEG experiment, this technique allowed to re-calibrate the PMTs and to improve the resolution from  $(6.5 \pm 0.6)$  to  $(4.9 \pm 0.4)$  %. This method will be used, during the normal operating conditions, to control the PMT quantum efficiencies and LXe optical properties.

## 5.2. Targets for the Cockcroft-Walton accelerator

At the beginning of 2005 the Group of Pisa (in particular Prof. C. Bemporad) proposed to calibrate the energy scale of the LXe detector by using high energy gamma line. Two main reaction  $(p,\gamma)$  have been selected:

1.  ${}^7_3Li(p,\gamma){}^8_4Be^{[7]}$ , with a resonance at  $E_p = 440$  keV that generates 17.6 MeV  $\gamma$ -line,
2.  ${}^{11}_5B(p,\gamma){}^{12}_6C^{[7]}$  with a resonance at  $E_p = 163$  keV that generates 16.1, 11.7 and 4.4 MeV  $\gamma$ -lines.

The advantage of the proton-reaction approach, which was used in a precursor of the  $\mu^+ \rightarrow e^+ \gamma$  experiment<sup>8</sup>, is that one generates  $\gamma$ -rays which illuminate isotropically the calorimeter from the COBRA center, testing the uniformity of its energy and space responses. Moreover, it should be possible to convert the 17.6 MeV  $\gamma$ -rays into an  $e^+e^-$  pair, and to use the positron for checking the magnetic spectrometer. It is worth nothing that, while the calorimeter calibration can be done using the full COBRA field, this is not possible for the spectrometer (drift chambers and timing counters), since the positron produced has a too low energy. In this case is necessary to reduce the COBRA field for reaching sufficient positron detection efficiency.

The performance of CW accelerator, in terms of intensity, energy resolution and stability are better than the previous VDG machine at the LNL. The principal differences are indicated in Table 5.1.

**Table 5.1:** Characteristics of the MEG CW and of the Legnaro VDG<sup>9</sup>.

Proton beam properties	MEG CW	Legnaro VDG
Energy (keV)	300-900	400-2000
Energy spread -FWHM (keV)	< 0.5	15
Spot size @ 3 m -FWHM (cm×cm)	< 3×3	< 0.5×0.5
Energy stability -FWHM (%)	0.1	0.2
Range of the average current (μA)	1-100	0.1-1
Current stability (%)	3	10

The aim of the test carried out at LNL was to measure the Li rate at 500 keV with thick target ( $\sim 10\Gamma_R$ ), perform measurements below resonance at 400 keV and measurements at 550 keV to check the rate saturation. Moreover, modifying the energy spread of the VDG machine\* it should be possible to measure the Li resonance excitation curve with a thin target ( $\sim 1\Gamma_R$ ), and to produce  $\gamma$ 's from  $^{11}_5B(p,\gamma)^{12}_6C$  by 500 keV protons.

According to the test purposes the targets should have the following properties:

- thin LiF target corresponding to 10 keV at 440 keV to be used with a variable energy beam of 5 keV spread, thickness 0.12 μm;
- thick LiF target corresponding to ~120 keV energy loss, to be used with 500 keV beam, thickness 1.41 μm;
- very thick LiF target corresponding to 500 keV proton range, thickness 4.74 μm;
- very thick B target corresponding to 500 keV proton range, thickness  $\geq 5$  μm.

### 5.2.2. Preparation of copper plates

Thin films may be prepared using several different techniques, the principal procedures for the deposition being: thermal evaporation, electron gun evaporation, chemical vapor deposition (CVD) and pulsed laser deposition (PLD).

---

\* The energy resolution can be improved by a factor  $\sim 3$ , but the intensity decreases quadratically.

Thermal evaporation is accomplished by using vacuum pumps to reduce the pressure inside a deposition chamber to  $10^{-4}$ – $10^{-6}$  mbar, and heating the material to be evaporated in a filament or boat made of a high melting point material. Both metals and thermally stable compounds, such as metal oxides, may be deposited. The properties of evaporated films depend on the film structure and also on the interaction of the film with its substrate.

To obtain the most durable and adherent coatings on different substrates, the support surface must be free of any contaminant materials such as grease or absorbed water. The degree of durability and adhesion of the deposit layer depends on many factors such as substrate, chemical affinity between substrate and film, growth temperature, other than surface cleanliness, which is a basic requirement to obtain a good target.

Several OFH copper plates were prepared with two aims: used as substrates for the materials to be deposited and act as a support inside the vacuum tube, used during the tests at LNL. Furthermore, copper improves the heat dissipation and minimizes the deterioration of the target during proton bombardment<sup>10</sup>. The plates with  $(50\pm1)$  mm of diameter and  $(2.0\pm0.1)$  mm of thickness have been obtained by wire erosion technique. In a second stage, the copper was polished by 1000, 2400 and 4000 AWG (American wire gauge) abrasive papers (Silicon Carbide) and, for final polishing, a colloidal silica suspension. In Figure 5.4 the Struers machine used to prepare the copper substrates is shown. Before the deposition, an acetone ultrasonic cleaning of the plates was performed.



**Figure 5.4:** Stage of working (left), final result of one plate (right).

### 5.2.3. Preparation of LiF targets

The Li targets are used to produce the calibration  $\gamma$ -line. Several complications during the preparation of metallic lithium targets occurred, caused by the high chemical reactivity of lithium. In the presence of small amounts of water, formation of LiOH takes place. When stored in absolute dry air, no chemical reactions occur. Another property of lithium metal, is its tendency to form alloys<sup>11</sup>. For these reasons lithium fluoride targets have been prepared. They are less sensitive to contamination and alloy formation; moreover the  $\gamma$ -line of fluorine is at  $\sim 6$  MeV, far enough from the  $^7\text{Li}$  line.

Several tests were carried out to find out the best conditions for the target deposition. In particular, in order to obtain a compromise between uniform thickness and the large area required for the experimental setup, the influence of the distance between LiF source and copper plate has been studied.

The thickness ( $t$ ) of material evaporated has been estimated using<sup>12</sup>:

$$t = \frac{m}{\pi\rho} \cdot \frac{\cos\theta \cos\phi}{r^2}, \quad (\text{A.1})$$

where  $m$  is the mass of the material with density  $\rho$  inserted in the tantalum crucible,  $r$  is the distance between the copper plate and the source and the angles  $\theta$  and  $\phi$  are shown schematically Figure 5.5.

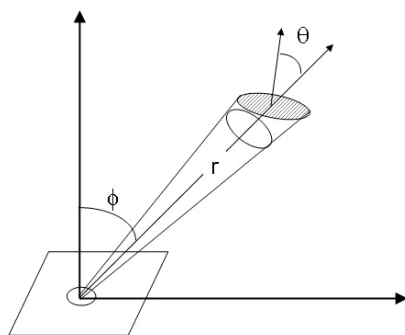


**Figure 5.5:** Evaporation geometry.

In these studies, both  $\theta$  and  $\phi$  angles were zero for the copper plate, while a non-zero  $\phi$  ( $\sim 19^\circ$ ) for the quartz balance; therefore the quantity of evaporated material to get the right thickness on the substrate was scaled. A cross-check for the thicknesses was made by measuring the targets with a profilometer. The deposition thicknesses of the

three LiF targets were  $4.72 \pm 0.18$ ,  $1.34 \pm 0.11$  and  $0.11 \pm 0.01$   $\mu\text{m}$  respectively, in agreement with the required values for the tests.

#### 5.2.4. Preparation of B targets

The boron targets were deposited using an electron beam evaporation technique with a carbon crucible due to its high evaporation temperature of  $1797$   $^{\circ}\text{C}$  at  $10^{-4}$  Torr<sup>13</sup>. In fact using standard evaporation technique, the tantalum and tungsten crucibles crack during the melting of boron and thus no deposition can occur. The thickness calibration system was similar to that previously described. Two targets were obtained with similar thicknesses:  $1.78 \pm 0.21$  and  $1.84 \pm 0.22$   $\mu\text{m}$ , thinner than the ones required for the Legnaro test.

#### 5.2.5. Experimental setup

The measurement of the  $\gamma$ -ray spectra was performed with two NaI detectors, a small cylindrical crystal with  $4''$  diameter and height, and a large square  $28\times28\times35$   $\text{cm}^3$ . The individual crystal calibration was initially obtained by a  $^{60}\text{Co}$ -source and, during the measurement, by natural radioactivity  $\gamma$ -lines at  $1.46$  MeV ( $^{40}\text{K}$ ) and  $2.61$  MeV ( $^{208}\text{Tl}$ ). One side of an aluminum pipe  $\varnothing 9\times160$  cm was attached to accelerator beam-line and the other one held the target at an angle of  $45^{\circ}$  relative to the beam-direction. Inside the pipe, four clamps placed at a diameter of  $51$  mm, were used as a support for the target. The sensible area was  $30$  mm, as this should be the final design of MEG system. Figure 5.6 shows the lay-out of the experimental setup: the covered solid angles are  $\sim 6.3$  and  $\sim 1.5\%$  for the big and small detector respectively.

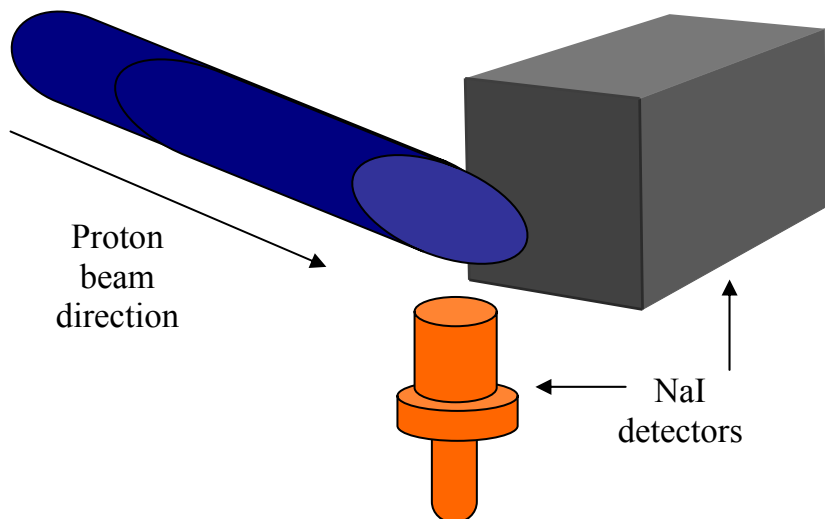


**Figure 5.6:** Layout of aluminium pipe and NaI detectors.

The target supporting pipe contained a set of diaphragms electrically insulated which can be read independently and used to align the beam on target. For the final MEG system a direct measurement of the proton current hitting the target and a method of beam alignment must be studied.

### 5.2.6. Results

In Figure 5.7 is showed the  $\gamma$ -spectra obtained using a thick 4.72  $\mu\text{m}$  LiF target, the 17.6 MeV and the 14.6 MeV  $^7\text{Li}$ -lines are showed. At low energy ~6 MeV is also possible to see the  $^{19}\text{F}$ -line and at even lower energies, the natural radioactivity lines of  $^{40}\text{K}$  (1.46 MeV) and  $^{208}\text{Tl}$  (2.61 MeV).

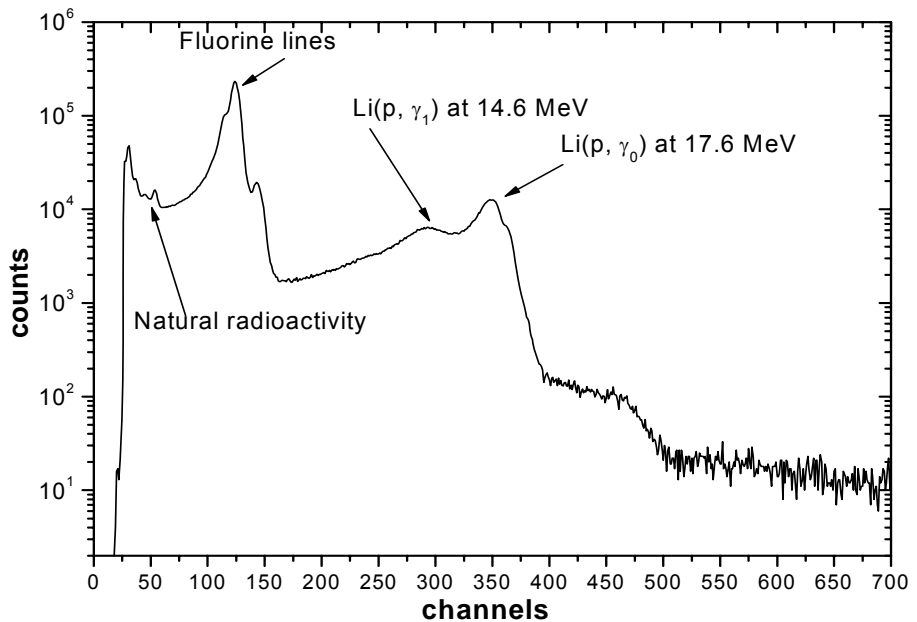


**Figure 5.7:** Thick LiF target  $\gamma$ -spectrum.

The observed  $\gamma$ -lines and the  ${}^7\text{Li}$   $\gamma$ -rate ( $\sim 2 \cdot 10^4$  @17.6 MeV) are in agreement with the expected spectrum generated by protons hitting  ${}^{14}\text{F}$ . In Figure 5.8 is possible to compare the spectrum obtained at  $E_p = 400$  keV, below the energy resonance, with one obtained at  $E_p = 450$  keV. The switching-on of the  ${}^7\text{Li}$ -lines is clearly seen in comparison with the rate of the constant  ${}^{19}\text{F}$ -line.

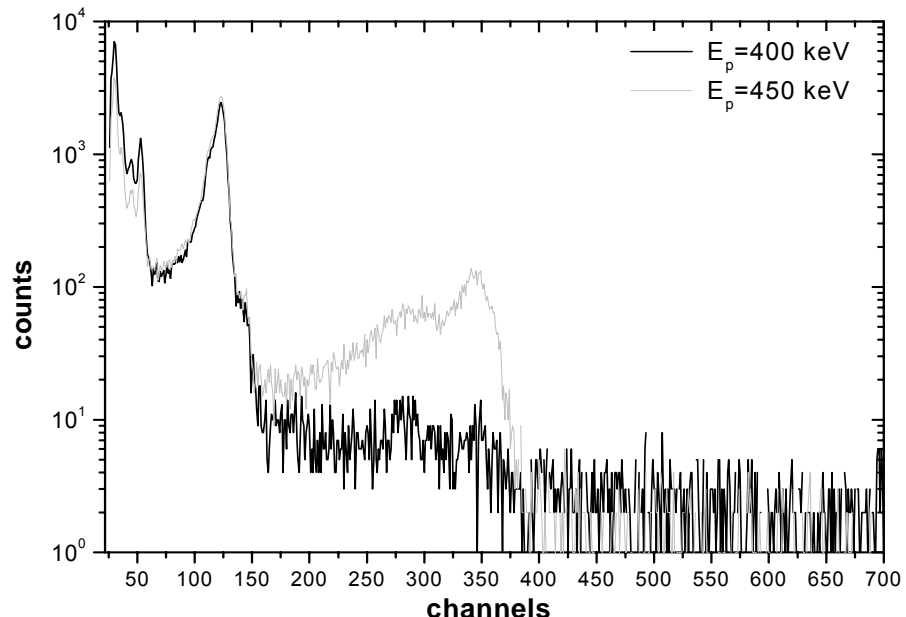


**Figure 5.8:** Thick LiF target  $\gamma$ -spectrum at  $T_p = 400$  keV (black-line) and at  $T_p = 450$  keV (light gray-line).

In Figure 5.9 the  $\gamma$ -spectra obtained using a  $1.84\text{ }\mu\text{m}$  B target is reported. Since the Legnaro VDG could not reach an  $E_p = 165\text{ keV}$ , the boron lines were excited by  $E_p = 500\text{ keV}$  protons. In this condition, with protons far from the resonance energy, the  $16.1\text{ }(\gamma_0)$  and  $11.7\text{ }(\gamma_1)$  MeV  $\gamma$ -rays will be produced at higher energies than the nominal value, due to energy conservation. Only the carbon de-excitation line at  $4.4\text{ }(\gamma_2)$  MeV emitted in coincidence with  $\gamma_1$  remains at the same energy reference.

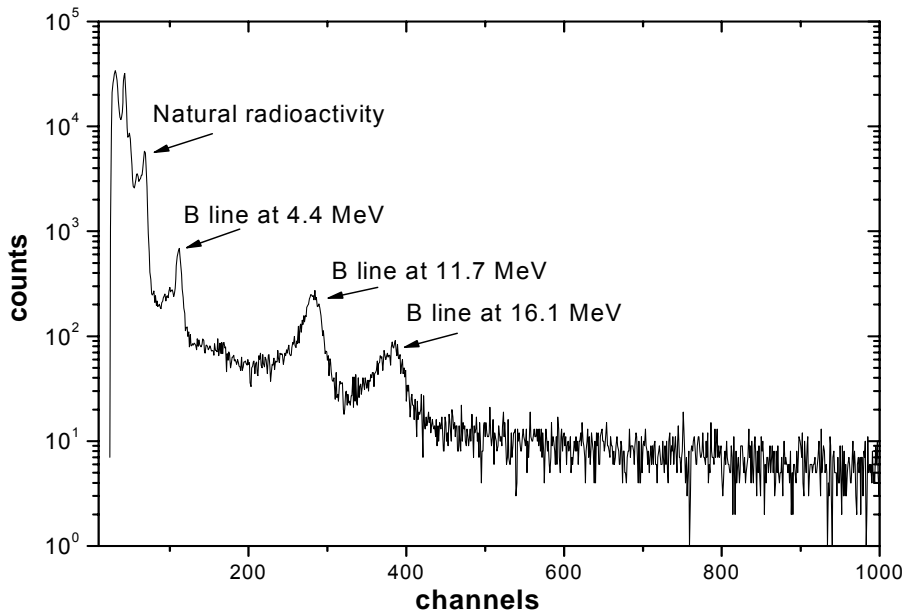


**Figure 5.9:** Boron target  $\gamma$ -spectrum.

During the Legnaro test, the coincidence rate of the  $16.1$  and the  $4.4\text{ MeV}$  emitted by  $^{11}_5\text{B}(p,\gamma)^{12}_6\text{C}$  reaction were measured. The large NaI was used to detect the  $11.7\text{ }\gamma$ -rays and produce a gate signal for the acquisition of the  $4.4\text{ MeV}$   $\gamma$ -rays in the small detector. These two  $\gamma$ -lines,  $\gamma_1$  and  $\gamma_2$ , will provide a method of testing the potentiality in distinguishing double  $\gamma$ -rays entering in the LXe calorimeter. In Figure 5.10 is reported the spectrum obtained in small NaI detector, the  $1^{\text{st}}$  escape represents the  $\gamma$ -rays that release only a part of their energy into the detector.

Moreover, the excitation curve has also been measured of  $0.11\text{ }\mu\text{m}$  thin and  $1.34\text{ }\mu\text{m}$  thick LiF target. The energy of the resonance measured  $(446 \pm 1)\text{ keV}$  appears to be  $\sim 5\text{ keV}$  higher than the expected value. This is probably due because of the Legnaro machine was not calibrated, since a long time, in energy.

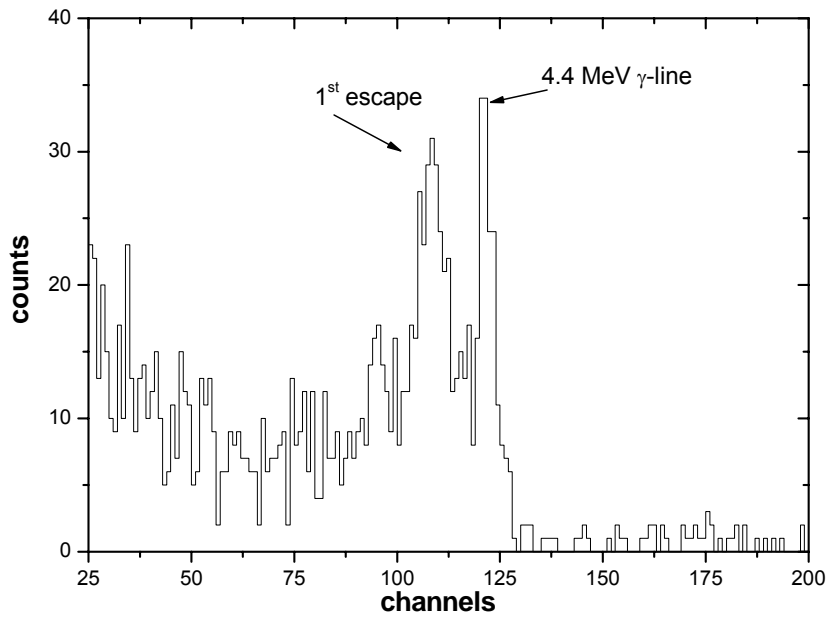


**Figure 5.10:**  $\gamma$ -line at 4.4 MeV emitted by  $^{11}_5B(p,\gamma)^{12}_6C$  reaction.

The Crockroft-Walton accelerator is one of the most versatile methods for calibration and monitoring the MEG experiment. The high rate statistics of  $^{7}_3Li(p,\gamma)^{8}_4Be$  reaction, should allowed a fast calibration of the LXe detector. The C-W is a low-radiation device which can be used without generating additional background, close to the experiment. The results obtained prove the validity of the proposed calibration method.

## Bibliography: Chapter 5

---

- <sup>1</sup> A. Baldini et al., MEG-TN027 (2005).
- <sup>2</sup> G. Signorelli, MEG Collaboration, Ph.D. Thesis, “A sensitive search for lepton flavour violation: the MEG experiment and the new LXe calorimetry”.
- <sup>3</sup> A. Baldini et al., MEG-TN029 (2005).
- <sup>4</sup> <http://nucleardata.nuclear.lu.se/nucleardata/toi/>.
- <sup>5</sup> <http://www.raz-dva.cz/sorad/>.
- <sup>6</sup> P. De Felice et al., “Leakage tests for  $^{241}\text{Am}$  solid sources used for Liquid Xenon Detector monitoring. ENEA internal note and arXiv: physics/0509101 (2005).
- <sup>7</sup> NACRE, European Compilation of Reactions Rates for Astrophysics, <http://pntpm.ulb.ac.be/nacre.htm>.
- <sup>8</sup> R. D. Bolton et al., Phys. Rev. D 38, (1988) 2077.
- <sup>9</sup> <http://www.lnl.infn.it>;  
<http://www.highvolteng.com>.
- <sup>10</sup> F. Zijderhand and C. Van der Leun, Nucl. Phys. A 460 (1986) 181.
- <sup>11</sup> G. Domogala et al., NIM A 257 (1987) 7.
- <sup>12</sup> L. Holland, Vacuum deposition of thin films, Chapman and Hall, Ltd (1961).
- <sup>13</sup> D. A. Glocker and S. I. Shah (Eds.), Handbook of Thin film process technology, IoP (1995).
- <sup>14</sup> D. Zahnow et al., Z. Phys. A 351, (1995) 229.

## ***Appendix A***

### **Plastic scintillator**

The scintillation light of these materials is generated by transitions of covalent electrons of  $\pi$ -molecular orbitals. Energy levels for  $\pi$ -electrons, in an organic molecule, are schematically represented in Figure A.1. Each principal level  $S_{0i}$ , is accompanied by vibrational sublevels  $S_{ji}$ . The first principal level is usually of few eV above the singlet ground state  $S_{00}$ . Vibrational levels have a typical spacing of  $\sim 0.16$  eV. There is also a sequence of excited  $\pi$ -electron triplet states ( $T_{0i}$ ) with vibrational levels ( $T_{ji}$ ), but with lower energy than the corresponding singlet states. When a photon, or charged particle, passes through an organic scintillator, as in this work, there is an excitation of electrons from the ground state to the higher excited singlet states. Thermal equilibrium is rapidly established, within  $\sim 10^{-11}$  s, populating predominantly the lowest electronic state, at room temperature. Then the radiative transition  $S_{1x} \rightarrow S_{0x}$  undergoes a fast transition, with a typical lifetime of  $10^{-8} - 10^{-9}$  s. It is important to notice that the fiber is transparent to its scintillation light (fluorescence), since the electrons decay to vibrational sublevels of  $S_0$ . Slow transitions from  $T_{0x} \rightarrow S_{0x}$ ,  $t \geq 10^{-4}$  s, constitute phosphorescence and are possible through the interaction of  $T_{0x}$  with another  $T_{0x}$  level as:  $T_{0x} + T_{0x} \rightarrow S_{1x} + S_{0x} + \text{phonons}$ , as illustrated in Figure A.1.

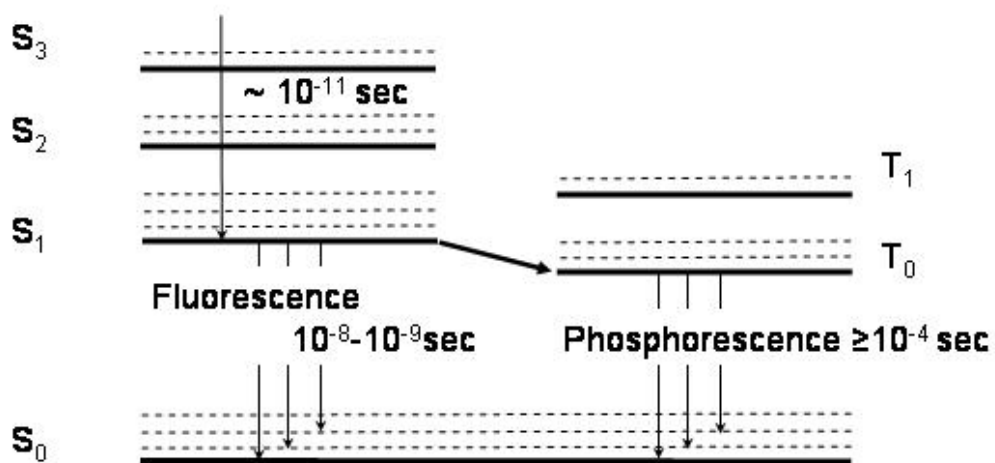


**Figure A.1:**  $\pi$ -electronic energy levels<sup>1</sup>.

## Bibliography Appendix A

---

<sup>1</sup> T.O. White, NIM A 273 (1988) 820.

## Acknowledgments

Finalmente la parte più interessante della tesi: i ringraziamenti. Per prima cosa voglio fare una precisazione. I ringraziamenti li scriverò in italiano perché così non dovrò più chiedere aiuto per le traduzioni. Sono molte le persone che devo ringraziare, quelle che mi hanno sopportato, quelle che mi hanno aiutato, quelle che hanno creduto in me.

Questi tre anni sono stati duri ma ringrazio il mio capo, Flavio Gatti, che ha creduto e crede in me, almeno spero, nonostante i miei precedenti “storici”. A questo proposito ringrazio tutto il laboratorio, L103, per l’aiuto, la simpatia e le risate che ci siamo fatti. In particolare, Adriano Bevilaqua, Luigi Parodi, Davide Bondi e soprattutto la Lilli, il cane più dolce che ci sia. Non posso ovviamente dimenticare gli altri componenti del laboratorio, Loredana Gastaldo, Lorenza Ferrari, Maria Ribeiro Gomes (semplicemente straordinaria, grazie), Daniele Pergolesi (a chi non disperde...), Pietro Repetto (e la sua vigna a Tramontana, mi mancherai) e Simeone Dussoni, il mio compagno di viaggio in questa straordinaria avventura. Di Simeone non voglio dire molto, posso dire che la mia ragazza, Valeria, è gelosa perché ho passato più notti con lui a lavorare e a fare misure che con chiunque altra persona, considerando oltre 100 giorni di trasferte. È una persona straordinaria ed un fisico incredibile.

Dino Zanello, il mio correlatore. Ma sarebbe riduttivo chiamarlo così. È uno dei fisici più geniali che conosca, un uomo che non solo si occupa del software per il timing counter ma che sa la vera fisica e non disprezza sporcarsi le mani quando si tratta di lavorare. Non posso dimenticare i suoi collaboratori: Alessandro Barchiesi ed Angelo Graziosi, due geni del computer, grazie.

Il gruppo di Pavia, tutti, che collabora con noi nell’esperimento. Ho conosciuto persone straordinarie con le quali ho passato piacevolissimi momenti. Ricordo in particolare Massimo Rossella e Roberto Nardò due persone fantastiche e simpaticissime, il Boca, Antonio, Giorgio Cecchet. A questo proposito non posso non

ricordare Maurizio Bonesini con il quale è stato fatto un lavoro incredibile sui fototubi (LASA-Milano), grazie mille.

Il gruppo di Pisa. Beh ricordarli tutti è difficile. Ho conosciuto un gruppo che lavora alla grande, se mi concedete l'espressione. Ricordo Alessandro Baldini, il capo italiano dell'esperimento, Carlo Bemporad, con il quale ho passato una settimana a fare misure a Legnaro, un grande fisico, si deve imparare molto da lui. Fabrizio Cei, Giovanni Signorelli, Marco Grassi (a questi ho veramente "rotto le palle", in questo periodo).

La BTF di Frascati nelle persone di Giovanni Mazzitelli e Bruno Bonomo. Grazie a loro siamo riusciti ad ottenere risultati straordinari. Grazie mille a tutte le persone che lavorano alla control room di DaΦne, gli ho angosciati per benino.

Gli INFN di Genova. Qui la lista è lunga quindi scusate se mi dimentico di qualcuno. Ringrazio l'officina meccanica dove ho passato buona parte del mio tempo, dove ho incontrato persone straordinarie ed ho imparato un sacco di cose. Molte di queste persone sono state in missione con me e mi sono sempre trovato benissimo. Roberto Cereseto, il capo officina, non solo è un grande esperto di tutto ma è un amico. Claudio, Andrea, Antonino, Palmiro insomma tutti. Il servizio elettronica degli INFN con a capo Paolo Musico, grazie per il supporto e il lavoro svolto. Ringraziamento particolare per Fabio Siccardi, oltre al lavoro mi ha tenuto sveglio con skype durante i beam test. Il servizio di disegno e progettazione degli INFN con a capo Stefano Cuneo, grazie per il lavoro svolto, soprattutto quando si ha a che fare con dei fisici. Il gruppo di ottica, in particolare Carlo per l'aiuto e la sua disponibilità. Per ultima, ma non meno importante, ringrazio l'amministrazione dove lavorano persone simpatiche e straordinarie, mi sono trovato benissimo con loro.

Non posso di certo dimenticare il famosissimo gruppo III nelle persone di Andrea Rottura che è veramente un pozzo di informazioni. Senza i suoi prestiti molte missioni sarebbero andate in fumo. Ti ringrazio molto. Un saluto anche ad un altro Andrea un po' più giovane ma molto più brutto...(scherzo) grazie per i consigli e le belle risate.

Adesso passerei ai ringraziamenti personali.

Sono grato a mia madre Elisa che mi ha permesso di studiare senza dovermi preoccupare di nulla, nonstante tutte le brutte cose che le dico sempre a lei devo veramente tutto. Ringrazio mia sorella Francesca che mi ha sopportato in questi anni e le auguro tanta felicità, visto che è in dolce attesa. Ringrazio in particolar modo Valeria; senza di lei non sarei riuscito in questa impresa. Mi ha aiutato e incoraggiato, a lei devo veramente molto, ti voglio un mondo di bene. Ringrazio i miei amici, vicini e lontani, tutti, in particolare Andrea Gerbi, anche lui fisico ma soprattutto un vero amico. I miei parenti che hanno sempre creduto in me, grazie.